October 2018

PROBING LOCAL VACANCY-DRIVEN RESISTIVE SWITCHING IN METAL OXIDE NANOSTRUCTURES

Jiaying Wang
University of Massachusetts Amherst

PROBING LOCAL VACANCY-DRIVEN RESISTIVE SWITCHING IN METAL OXIDE NANOSTRUCTURES

A Dissertation Presented

by

JIAYING WANG

Submitted to the Graduate School of the
University of Massachusetts Amherst in partial fulfillment
of the requirements for the degree of

DOCTOR OF PHILOSOPHY

September 2018

Mechanical Engenieering

PROBING LOCAL VACANCY-DRIVEN RESISTIVE SWITCHING IN METAL OXIDE NANOSTRUCTURES

A Dissertation Presented

by

JIAYING WANG

Approved as to style and content by:

Stephen S. Nonnenmann, Chair

Jae-Hwang Lee, Member

Yubing Sun, Member

Jianhua (Joshua) Yang, Member

Sundar Krishnamurty, Department Head
Yahya Modarres-Sadeghi, Graduate Program Director
Mechanical Engenieering

DEDICATION

To my grandparents.

ACKNOWLEDGMENTS

I would like to thank my advisor, Prof. Stephen Nonnenmann, for his many years of thoughtful, patient guidance and support. Thanks are also due to my groupmates Jiaxin Zhu and Zimu Zhou. Together their friendship and selfless contribution to my professional development have been invaluable and will forever be appreciated. I would also like to extend my gratitude to the members of my committee, Prof. Jae-Hwang Lee, Prof. Yubin Sun and Prof. Jianhua Yang, for their helpful comments and suggestions on all stages of this project.

I wish to express my appreciation to all the individuals who volunteered their participation in this project. I want to thank University of Massachusetts-Amherst for partly funding this research and providing travel expenses during academic conferences. I am very grateful to the UMass Center for Hierarchical Manufacturing (CHM), a NSF Nanoscale Science and Engineering Center (CMMI-1025020), and through the NSF Directorate of Engineering under award CBET-1706113. Thanks to John Nicholson for training and supporting the use of cleanroom facilities. My experiments, especially the advanced semiconductor device fabrication, would never have been possible without his helps and efforts to ensure the up-to-date maintenance. I thank him for always being supportive with his technological skills and providing valuable suggestions on each project. In addition to the facility staff of the cleanroom lab where I have spent my last couple years, all the helps and encouragements from fellows who worked in the lab could be indispensable part of my growth and harvest. Zhongrui Wang, Peng Lin, Hao Jiang, Shuang Pi, Can Li, Peng Yan, Ye Zhuo, Navnidhi Upadhyay, Shiva Asapu, Dacheng Mao, Hongwei Tan thanks for sharing your knowledge with me during the last four years.

I wish to thank the collaborators Satyan Choudhary for performing the fabrication and transfer of nanoribbons, William L. Harrigan, Jonathan De Roo and Katrien De Keukeleere for synthesizing the solution-processed oxide nanocrystals, Prof. Alfred J. Crospy, Prof. Kevin R. Kittilstved for supervising the works from begin to end. Thank you all for their tireless efforts in typing the many versions of the manuscripts.

A special thanks to my roommates Wanting Xie, Shaoling Zhang, Zheyuan Hu. Thanks for offering help and care on my daily life, teaching and encouraging me to get through difficult situations and always being there for me. And Ami Gao, Boyuan Liu, Zhuang Liu, Wenbo Wang thank you to all those whose support and friendship helped me to stay focused on this project and who have provided me with the encouragement to continue when the thing getting tough.

ABSTRACT

PROBING LOCAL VACANCY-DRIVEN RESISTIVE SWITCHING IN METAL OXIDE NANOSTRUCTURES

SEPTEMBER 2018

JIAYING WANG

B.E., BEIJING UNIVERSITY OF TECHNOLOGY

Ph.D., UNIVERSITY OF MASSACHUSETTS AMHERST

Directed by: Professor Stephen S. Nonnenmann

Novel nonvolatile memory technologies garner intense research interest as conventional flash devices approach their physical limit. Memristors, often comprising an insulating thin film between two metal electrodes to constitute a class of two-terminal devices, enable a variety of important large data storage and data-driven computing applications. In addition to nonvolatile behavior, other features such as high scalability, low power consumption, and sub-nanosecond response times make memristors among the most attractive candidate systems. Their strength in electronic storage relies on the unique properties of the tunable variations in resistance induced from the accumulation of charged defects based on the applied bias history.

Metal oxides serve as the most common "storage" materials, demonstrating advantages including simple fabrication, high reliability, and fast operation speeds. While the basic working concepts and the underlying conduction mechanisms have been established through combined experimental and simulation studies, the role of metal-insulator interface, which acts as the crux of coupled electronic-ionic interactions,

has not been fully understood. Continuous scaling, for the purpose of high density memories, also requires a detailed understanding of the switching behavior and transport mechanism. Other technical challenges include the development of innovative, low-cost fabrication methods that effectively enable high-performance structures as an alternative to complicated process modules. Stable retention and endurance of the switching characteristics, as well as uniformity of the switching parameters to ensure a valid program/read operation also represent significant challenges. Studies in device and materials optimization remain in the formative stages, and thus motivate this work to drive progress in the most attractive areas, including size dependent behavior and switching performance of memristors.

This collection of work aims to correlate resistive switching within metal oxide based memristors with the fundamental physical mechanisms and material properties on a highly localized scale. Chapter 3 relates the device size and the resulting performance matrix of memory cells in the first step towards fully understanding the scaling projection and reliability issues that affect nanoscale architectures. Chapter 4 demonstrates a convective self-assembly, transferable approach that enables the fabrication of highly-controlled nanoribbon comprising solution-processed nanocrystals, providing multiple degrees of freedom for understanding the interfacial memristive behavior of functional oxide nanostructures. As a powerful tool in the study of resistive switching, conductive AFM probes the homogeneity of the charge transport properties, thus offering electrical information by locally applied bias when it is placed in direct contact with desired regime. Finally we also focus on the improving the cycle-to-cycle uniformity by embedding nanostructure into conventional metal-insulator-metal (MIM) geometry in Chapter 5. This improvement is attributed to the concentration of electric field when metal nanoislands are inserted into the oxide film matrix. The details of this work will highlight the tunable and optimizable template-driven method that

can be applied on any memristive systems, yielding a superior uniformity of operating voltage and resistance states.

In summary, this thesis promotes the development of novel, high-performance metal oxide based memristors enabled by the availability of new, nanostructured materials and innovations in device structure engineering. The switching performance, underlying mechanisms, area/defect concentration effects, development of solution-processed nanocrystals assemblies and chemistries, and highly enhanced uniformity in memristors are addressed by combining systematic deposition approaches with the advanced nanoscopic observation of the conducting filament, leading to the strongest competitor among future nonvolatile memory solution.

TABLE OF CONTENTS

LIST OF TABLES

Table **Page**

LIST OF FIGURES

Figure **Page**

CHAPTER 1

INTRODUCTION AND BACKGROUND

1.1 Fundamental of Resistive Switching

As Moore's law faces its physical limit, resistive switching memories (RRAM) have emerged as a promising next generation non-volatile memory device. While resistive switches, or memristors, were first discovered as a missing circuit element in 1971 by Leon Chua,[1] their use in a wide range of applications including storage devices, analog devices and neuromorphic computing have renewed interest and attention over the past decade. After the initial demonstrations of high performance, high density platforms, RRAM devices are now entering the industrial development stage. In the near future, RRAM is expected to replace NAND Flash and embedded memories allowing faster computing with large capacities due to the high speed and remarkable scalability. [2] [3]

RRAM cells typically comprise an insulating metal oxide film between two metal electrodes (metal-insulator-metal; MIM), constituting a class of two-terminal devices that exhibit tunable variations in resistance based on the history of the applied bias.[4][5] The physical effect in the RRAM device is based on the resistive switching (RS) effect, a reversible change in resistance between a high resistance state (HRS) and a low resistance state (LRS) by applying an electric field to the electrode. The "set" operation is defined by the transition from the LRS to the HRS; the opposite switching event (HRS to LRS) defines the "reset" operation. A virgin cell, which displays a high resistance due to defects generated during thin film processing, usually requires a high voltage electroforming process leading to the dielectric soft breakdown

process in order to enable subsequent set/reset operation. As the "1" step shown in Figure 1.1 a-c, a low compliance current is applied to avoid the permanent damage of the device or to tune different switching characters during electroforming. This process induces redox/electrochemical reactions at the metal-oxide interface that produce oxygen ions which migrate under electric field to ultimately form a conductive path connecting the top and bottom electrode (Fig 1.1 c). Conversely, the opposite electric field reverses oxygen ion migration towards the other electrode interface and thus ruptures the conductive channel, resulting in the recovery of the high resistance state as shown in Fig 1.1 d. The operating voltage at which the set and reset event occurs is denoted as V_{set} and V_{reset}, respectively. The resistance values at different states can be determined using a small read voltage and their ratio is defined as R_{HRS}/R_{LRS} (or R_{OFF}/R_{ON}). Numerous materials exhibit RS, including transition metal oxides, nitrides, and complex metal oxides such as perovskites. Transition metal oxides such as TiO_2,[6][7] HfO_2 [8] and Ta_2O_5 [9] have experienced particularly intense research and development interest due to complementary metal-oxide-semiconductor (CMOS) compatibility and demonstrated advantages such as scalability, fast switching speed, and low power consumption. Resistive switching in binary transition metal oxides have been reported in various nanostructures such as nanoparticles (0D),[10][11]nanowires/nanotubes (1D),[12][13][14] and thin films (2D). [6] [15]

1.2 Classification of RRAM

RRAM devices are classified into three categorizations, based on the polarity dependency: unipolar resistive switching (URS), bipolar resistive switching (BRS), and complementary resistive switching (CRS). URS is observed when switching between HRS and LRS occurs in each polarity of applied voltage, which has been found in many transition oxides such as NiO,[16] [17] TiO_2,[7] [18] and Nb_2O_5. [19] In BRS,

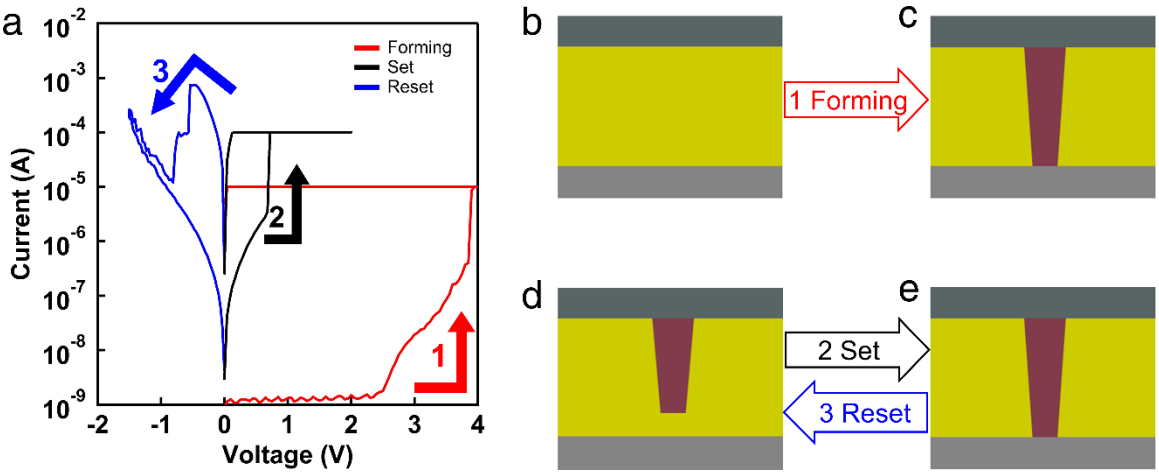

Figure 1.1. a. Typical bipolar resistive switching I-V curves including forming, set and reset process. b. the schematic illustration of the corresponding processes in a that 1 forming, 2 set and 3 reset.

switching is directional that one polarity induces LRS while the other polarity recovers to HRS. This type of switching has been reported in Ta_2O_5, HfO_2 and many complex perovskite oxides.[20] [21] The CRS has been usually measured in those structures where two BRS cells are merged in an antiserial manner,[9] [22] remaining at high resistance at low bias voltages then can be subsequently switched to the LRS with larger voltages. By further increasing the applied voltage, however, the resistance changes back to the LRS. In recent studies,[23] this behavior has also been reported for a single cell where the switching layer was modulated into different defect concentrations or using different operation conditions. This highly nonlinear behavior has received considerable attention due to the potential of overcoming the current path issues that occurs in the passive crossbar RRAM arrays.

RRAM are also classified into two types with respect to the switching mechanism as anion-type and cation-type. Anion-type memristor, or valence change memory (VCM), is dominated by oxygen ions induced from the preparation process or formed during forming/set process. VCM cells are typically fabricated into MIM structures with one high work function electrode and an Ohmic counter electrode, which cre-

ates a Schottky-like interface that tunes the subsequent resistive switching process by modifying the interface under applied electrical field. VCM cells can exhibit filamentary type switching, as described in Figs. 1.1b-e. Among the possible metal oxides, Ta_2O_5 displays the most promise for application due to its large ON/OFF ratio, good reliability, low operation energy, and additional CRS behavior. VCM also exhibit an area-dependent interfacial type switching mode in which the switching process takes place at the interface between electrode and the oxide, involving in various perovskite oxides such as $SrTiO_3$.[24] [25] Another crucial category that has been developing rapidly is anion-type electrochemical metallization memory (ECM), where the switching behavior is dominated by the formation and dissolution of a metal filament. Here stacks consisting of one chemically active electrode such as Ag,[26] Cu,[27] or Pd[28] were recently found to produce cation ions of Ag^+ or Cu^{2+} that migrate through a solid electrolyte under positive bias towards an inert counter electrode (Pt, Ir or TiN). To obtain the LRS, the redox and dissolution process leads to the formation of metallic filaments by applying a positive bias to the active electrode. Conversely, a negative bias causes the conductive filament to dissolve and initiates the LRS to HRS transition. Although issues in identifying the mechanism still need to be addressed, recent *in situ* TEM and *ex situ* c-AFM observations of cation migration have provided compelling experimental evidence.[29] [30]

The basic performance parameters of RRAM devices include retention time, endurance, scalability, stability, write speed and energy consumption. The ideal RRAM is a high-density architecture with at least ten year reliability, stable lifetime, fast response speed, and minimal energy consumption. One of the primary advantages that RRAM has over Flash is its fast speed, which is on the order of nanoseconds.

1.3 Remained Challenges and Perspectives

The revolution of RRAM is at a stage where theoretical studies are maturing and steps towards large scale integration are realizing its potential. In the past decade, RRAM have advanced in multiple industry arenas, primarily due to concurrent developments in materials engineering and knowledge of the underlying transport mechanisms. Several challenges still remain to be solved in terms of further improvements in scalability, uniformity and reliability. Enhancing the uniformity and reliability are urgently required for high volume integration and are thus among the strongest priorities for RRAM devices and improvements in order to replace the conventional flash memory.

Scalability down to the nanometer regime is necessary for future high density integration. The active device area is defined by a single conducting filament, which can be as small as a few atomic units, depending on various underlying mechanisms responsible for filament formation. In recent years, device scaling has achieved sub-100 nm dimensions by nanoimprint lithography and e-beam lithography; however, further refinements are facing the resolution limit of lithography or etch techniques. In addition to minimizing the size of the device, it is important to retain the performance. Devices may lose their uniformity or reliability when scaling to extremely small sizes, further motivating the importance of understanding the correlation between scalability and performance optimization.

1.4 Outline of the Dissertation

This thesis primarily focuses on understanding the underlying transport mechanisms, controlling defect density and defect movement, designing device fabrication, and improving device performance of RRAM to meet industrial requirements. The switching behavior takes place in a highly confined volume, which enables the scaling potential for a sub-nano device to create a large capacity memory. However, as

RRAM is based on the formation and rupture of conducting filaments during every read/write operation, RRAM is strongly affected by switching fluctuation. In this case, uniformity becomes one important evaluation factor for RRAM, as well as a major barrier impeding industrial commercialization. Variations in the numbers/sizes of the conductive filaments resulting from random formation under electric field are considered as the origin of the parameter fluctuations. To address this challenge, direct characterization of the filament morphology is required. In addition, innovations in device structure and integration schemes are highly desirable. Other outcomes include novel materials or processes that improve endurance, retention and cost reduction. This thesis targets the resistive switching character of oxides, which can be summarized as follows:

- Controlling the formation of the conductive filamentary channel in HfO_2 based RRAM devices by embedding highly-ordered metal nanoislands into the oxide thin film matrix, which greatly reduced the operating voltages and enhanced switching uniformity.

- Identifying the conductive channel morphology by three dimensional tomography to understand the origin of instabilities in RRAM devices.

- The development of a low cost and innovative approach for solution-processed nanoparticle assemblies, the study of their memristive behavior, the effect of the organic ligands, and the realization of flexible resistive switching devices with remarkable stability under 5% strain.

- Investigations of area dependent resistive switching in polycrystalline TiO_2 based RRAM devices to gain further insights towards device scalability and transport mechanisms.

This work outlines advances in three-dimensional AFM-based characterization techniques that enable the direct and complete observation of the conductive regime,

critical to VCM optimization. The goal of the thesis is to establish a clear correlation between nanoscopic features and performance metrics. The strategies and the resulting achievements are presented in six chapters.

Chapter 2 describes the basic scanning probe microscopy (SPM) techniques for electrical characterization, including conductive atomic force microscopy (c-AFM), Kelvin probe force microscopy (KPFM), electrostatic force microscopy (EFM) and scanning tunneling microscopy (STM). The major advantages and drawbacks of these techniques in characterizing RS will be discussed in detail. It covers the most progress to the outstanding challenges and potential opportunities for future study, including combined approaches to reach the intrinsic nature and origin of switching.

Chapter 3 demonstrates the direct correlation between variations in fabrication and annealing environment on the resultant electroforming, set, and reset voltages in TiO_2-based thin-film nanostacks. This study presents the influence of varying electrode sizes on the electroforming operation voltage and resistive switching properties across nanoscale $TiO_2/Nb:SrTiO_3$ junctions. The nanostructures displayed effective switching behavior, possessing highly stable and reproducible high resistance state to the low resistive state ratios (R_{HRS}/R_{LRS}) as large as three orders of magnitude. It compares the I-V character of samples with diameters ranging from 200 to 500 nm. Moreover, the switching polarity can be reversibly changed between eight-wise and counter-eight-wise due to variations in available oxygen vacancies.

Chapter 4 introduces a low-cost flexible blade deposition (FBD) method to create highly ordered STO memristive nanoribbons from colloidal STONCs building blocks. The FBD approach enables facile fabrication of high-quality perovskite oxide low-dimensional nanostructure arrays onto arbitrary substrates that retain their resistive switching functionality. Moreover, we demonstrate the transfer of the nanoribbons from the original substrate onto a second, arbitrary substrate possessing a different contact surface, posing significant implications for tailoring the resistive response type

through substrate selection. The original structures were released into deionized water and then transferred and redeposited the ribbons onto a flexible PET substrate with metal coating for examination via c-AFM. Virtually all studies involving resistive switching of thin films remain limited by the top-down lithographic processes to evaporate or sputter various top electrode materials on a fixed film/metal/substrate bottom electrode configuration. The FBD transfer process provides the unique advantage of selecting the bottom electrode material to induce or potentially enhance a desired transport mechanism within functional oxide nanostructures. The resistive switching character of nanoribbons was further determined to correlate directly with the organic capping layer length of their constituting HfO_2 nanoparticles, using oleic acid, dodecanoic acid, and undecenoic acid as model nanoparticle ligands. Through a systematic comparison of the forming process, operating set/reset voltages, and resistance states, we demonstrate a tunable resistive switching response by varying the ligand type, thus providing a base correlation for solution-processed RRAM device fabrication.

Chapter 5 demonstrates a superior uniformity within HfO_2-based memristors by embedding highly-ordered metal nanoisland (NI) arrays. Both SET and RESET voltages exhibit significant reduction, with enhanced uniformity of operating voltages and resistance states. This improvement is attributed to the concentration of electric field when metal NIs are inserted into the oxide film matrix. The interactions between the Pt and Ti metal nanoislands and local oxide environment display separate filamentary formations affecting the stability. To further optimize the uniformity the nanoisland position is shifted down the thickness dimension towards the bottom electrode. A comparison of the density and distribution of the oxygen vacancies responsible for the formation/dissolution of conducting filaments is made via combined electrostatic force microscopy (EFM) and conductive atomic force microscopy (c-AFM) studies. Finally, a c-AFM nanotomography technique enables complete observation of the

morphological evolution of conducting filaments produced by Pt and Ti, providing direct correlations to the overall switching performance.

Chapter 6 summarizes the study in terms of fabrication, electrical characterization and performance optimization of resistive switching memories. Potential future directions will be discussed based on the research results in these years. The contents of this chapter will concentrate on outlook of the field including the existing technical difficulties to be addressed as well as the proposed solutions.

CHAPTER 2

ADVANCED SCANNING PROBE MICROSCOPY CHARACTERIZATION

The emerging commercialization potential of RRAM has resulted in part to the rapid advances of nano-characterization technologies. Observations of conducting channels and studies of the underlying physics have frequently used *in situ* transmission electronic microscopy (TEM),[7] [31] [32] scanning probe microscopy (SPM)[8] [30] [33] [34] [35] or x-ray photoelectron spectroscopy (XPS)[36] [37]. Scanning probes have become a powerful suite of tools for studying RS behavior due to the ability to detect the local electronic response, map the current distribution, and profile the band bending and defect density across the MIM structure to provide extensive information on the surface potential in high lateral resolution before and after switching. Although there are a few examples of reviews introduce this technique from background to the observations of conductive channel in memristor,[20] [38] [39] [40] [41] the latest achievements and its potential functionality that may lead to future breakthrough is still missing.

2.1 Atomic Force Microscopy (AFM)

AFM is the most efficient tool for studying surfaces, allowing topographic characterization on the atomic level. Figure 2.1a illustrates the basic principles of AFM. It can be operated in non-contact, lift or contact mode, where non-contact mode operation is generally used as a nondestructive measurement method. The interaction between the tip and sample is altered as the tip-sample distance changes and

is represented as cantilever deflection, which is translated by the oscillating signal on the photodetector. During the scanning, height and phase image offers wealth of information about the topography and sample mechanical properties, respectively.

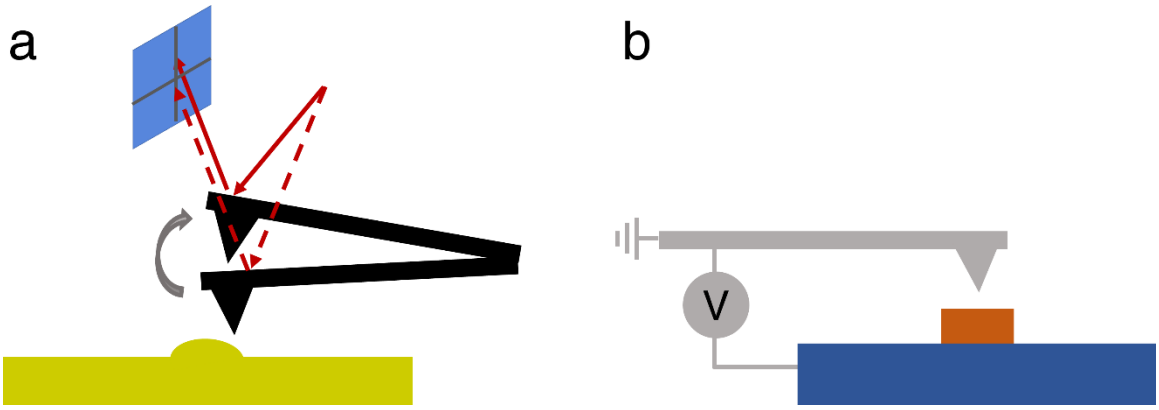

Figure 2.1. a. Basic working diagram of AFM. b. Illustration of c-AFM setup. The conductive probe uses as a movable top electrode. The bias is applied to the bottom electrode with the probe is grounded.

2.2 Conductive Atomic Force Microscopy (c-AFM)

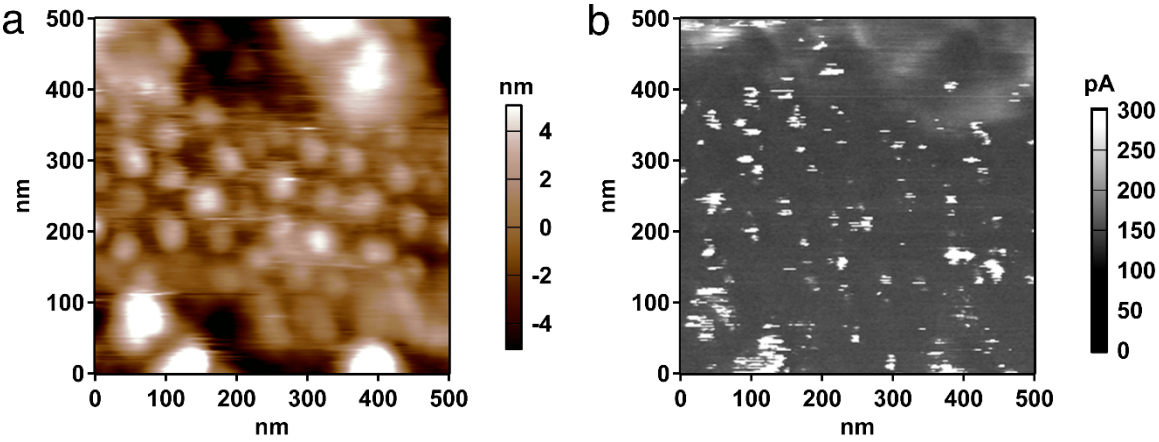

Figure 2.2. a. The AFM topography of Pt nanodot arrays embedded in HfO_2 thin film and b. the corresponding c-AFM current response under a voltage of -5V.

C-AFM is a contact mode method that enables current mapping via applying bias voltage between the sample and a conductive tip, which serves as a moveable top

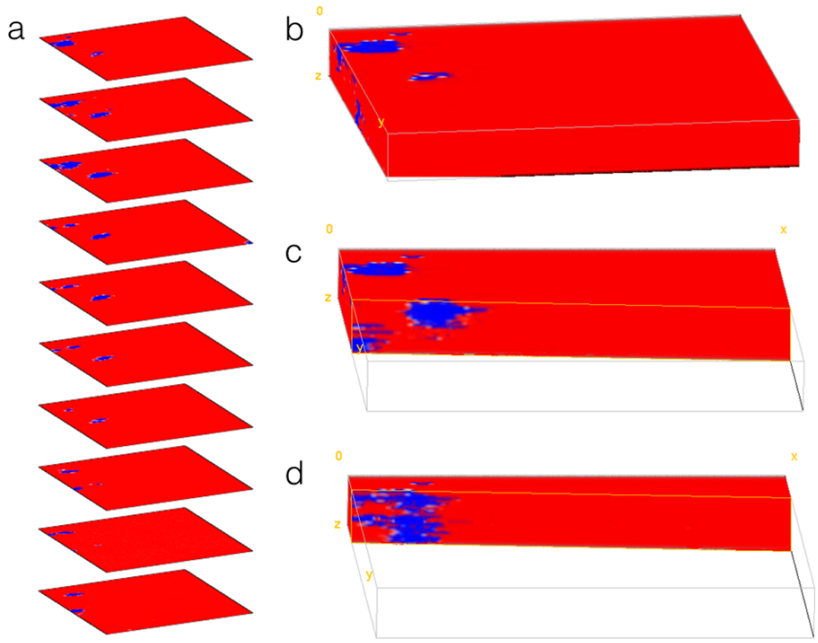

Figure 2.3. a. A stack of ten 2D slides collected by scalpel c-AFM on a HfO_2 memristor, demonstrating the varying shape of the conductive filament from top to the bottom. b, The 3D construction of the 2D slides c-d, with different cut-off interface which allows detailed observation of the conductive filaments.

electrode. Figure 2.1b shows a typical setup of c-AFM. With topography imaging, it directly detects local electrical properties to the region of interest with nanometer precision. The nanoscale dimension of the tips, enables current sensing of specific small features, and thus complements macroscale methods such as four-point probes that test an entire device. As the tip interacts with the sample surface, it is biased from a voltage source and the current flows through the sample into the tip which then passed into an amplifier using a feedback resistor and converted into an output signal. The topography and the current images can be recorded simultaneously, as shown in the example Figure 2.2. The sample is a 5 nm HfO_2 thin film embedded with nanodots at the interface between oxide layer and bottom electrode. The bright spots in Figure 2.2b correspond to the position of the nanodots which can be observed from the topography in Figure 2.2a. During the measurement of localized current-voltage (I-V) curves, the key factors include the force loading and the applied voltage.[42] In

this case, the tip is engaged to the surface at a user-defined position. While the tip is placed in contact with a large force, the noise is reduced and current signal can be improved with the sacrifice of the wear of the conductive metal coating. Worn coatings cause the failure of the tip at a high applied voltage because of the high electric field concentrated under the tip creates a suddenly high current. These obstacles are overcome by either decreasing the loading force appropriately or using solid metal probes as a replacement of the silicon probe with conductive coating. C-AFM offers high lateral resolution with sensitivity to carrier concentration, thus it can be used for semiconductor dopant profiling which is especially useful for studying the mechanism behind RS.[42] [43] [44] The electroforming process depends on the atmosphere [18] and the compliance current in the symmetric cells,[45] which determines the resulting switching type.

Major breakthroughs, such as the nature of conducting filament formation and the distribution of defects in interface-type switching have been realized by advanced SPM. C-AFM studies have demonstrated the nature of electroforming process in a $Pt/TiO_2/Pt$ crossbar device.[46] In this study, the AFM cross-sectional profile of a micro-sized device revealed considerable deformation within the topography image, where the formation of a bubble at the top electrode after forming was attributed to the drift of oxygen ions and subsequent oxidation reaction to form oxygen gas at the positive biased top electrode. Upon reduction of the device dimensions to the nanoscale the physical deformation disappears, and the performance metrics, including reproducibility and stability, were also significantly improved. The overall electroforming process for VCM made with transition metal oxides is thus defined by an electroreduction process that produces oxygen vacancies which are subsequently attracted to the anode to the form the conducting channel. Note in most cases an asymmetric metal/oxide interface displays Schottky-like barrier while the other maintains Ohmic contact.

Recent studies by Umberto et al.,[30] [47] demonstrated a remarkable approach that enables three-dimensional (3D) imaging of the conductive filament in both VCM and ECM. Here sequences of the scanned and etched slides are performed of the bare insulating layer using c-AFM under a low voltage bias after the removal of the top electrode. The high lateral resolution 2D c-AFM imaging provides information of single conducting filament in both HRS and LRS, permitting complete, multi-dimensional observation as well as more insight into the understanding of the switching nature. High resolution slices show that in a HfO_x layer the filament displays a size shrinking from 38.9 to 7.8 nm^2 with the constriction at the bottom electrode. However, the conical-shaped filament observed in ECM with Cu as the active electrode represents a much larger size compared to that in VCM. This confirms that the resistance of the conducting filament is determined by the number of defects at the narrowest point and suggests that VCM can be scaled down to sub-10nm. Figure 2.3 shows an example of the scalpel c-AFM of a HfO_2-based memristive device. The 2D current maps were obtained by the "remove-and-scan" method and stacked together, representing the evolution in conductive spot size from the top interface to the bottom with a sample slice spacing after removing the electrode. The three-dimensional integration shown in Figures 2.4b-d demonstrates the ability to collect nanoscopic information, such as the ability to distinguish only one larger primary filament that connects the top and bottom electrodes from two partial filaments that end inside the oxide layer.

2.3 Kelvin Probe Force Microscopy (KPFM)

KPFM is one of the most important techniques that provide information of the potential difference between the probe tip and the sample. It relies on an AC bias applied between the tip-sample that creates an electrostatic force arising from the differences in Fermi energy levels, which is interpreted by the following equation which considers the tip and the sample surface as a parallel capacitive structure,[38]

$$F = \frac{1}{2}\frac{\partial C}{\partial z}V^2 \tag{2.1}$$

where C is the capacitance, z is the separation among the tip and the sample. The contact potential difference will form when the system approaches an equilibrium state that the Fermi level to align through electron tunneling current.[48] Applying an external DC bias with the same magnitude of the potential difference can balance the force, and then consequently measure the local work function using the known tip work function.

Direct observation of filaments in many binary oxides presented in recent works provides the opportunity to predict the switching properties under operating conditions. Both BRS and URS phenomenon are frequently observed within NiO thin films, corresponding to alternating formation and rupture processes of conducting filaments that consist of oxygen vacancies.[16] [17] [49] [50] In order to realize the position that drives RS, a study of BRS NiO by Min et al. used a combination of c-AFM and KPFM.[39] Based on the c-AFM results, they suggested that the redox reaction at the interface between NiO and the probe dominants the conduction mechanism. KPFM imaging exhibited a more positive surface potential for the area scan with positive voltage and vice versa, indicating that oxygen ion extraction and incorporation occurs at the tip/NiO junction rather than in the NiO layer.

Grain boundaries play a crucial role in polycrystalline oxide switching materials, providing a fast pathway for the transport of oxygen vacancies. The higher current levels at leaky grain boundaries are the only sites to tune the RS phenomenon in polycrystalline materials such as HfO_2 because of the high concentration of oxygen vacancies.[43] Current imaging revealed that grain boundaries act as the preferential path while no RS can be observed within non-conductive grains. For amorphous HfO_2, however, the conduction was more homogeneous and no RS was detected at any

position by using the probe. For a better understanding of the conduction mechanism, a separate study by the same group showed the forming voltages at grain boundaries are significantly lower than those at the grains where no RS is observed, confirming the larger conductivity correlates with the favored formation of conducting filaments at the grain boundaries.[8] Note that charge trapping of metal ions diffusing from the probe tip into the insulator occurs when using a large applied voltage that yields a considerably high current density under the tip.[51] Alternative mechanisms proposed relate mechanical strength with RS behavior in HfO_2, where the grain boundaries are considered to be mechanically weaker than the nanocrystals which ultimately lead to the formation of reversible conducting filaments at those sites.

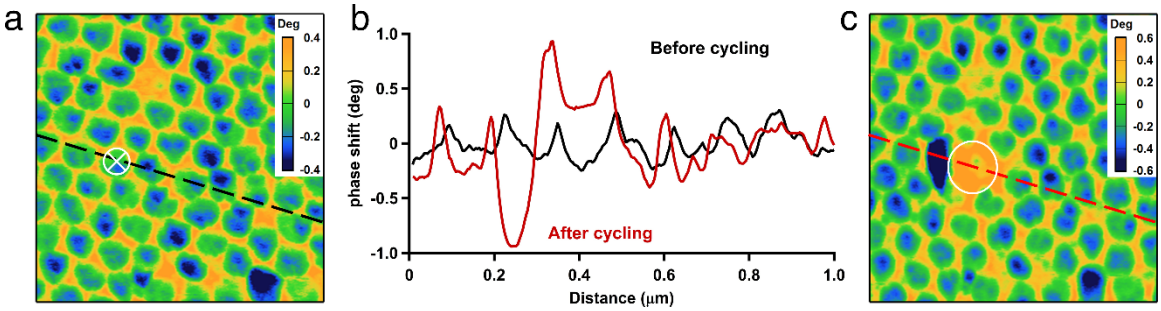

Figure 2.4. EFM image of Pt nanoislands embedded HfO_2 resistive switching structure a, before and b, after applying voltage sweeping locally. c. A comparison of the phase shift profile along the black dot line and red dot line in a and c, respectively.

2.4 Electrostatic Force Microscopy (EFM)

Electrostatic force microscopy (EFM) represents an effective means to detect the conductive inclusions within insulating matrix. EFM is a standard two-pass imaging mode to qualitatively measure the thin film's longer-range electrostatics forces, which is represented as a phase shift of the oscillating cantilever. It maps the force gradients generated by local variation in capacitance and conductors embedded in nonconductive materials. The variations originate from the trapped charge or potentials are sensed by the conductive probe. For these reasons, EFM is valuable for studying

memristive devices. In the first pass, a typical topography is obtained in tapping mode. In the second pass, a lift mode retraces the first topography line at a constant lift height above the sample surface. A DC bias between the tip and sample is applied during the lifted scan while the cantilever is driven by the tapping piezo, allowing shifts in the resonance frequency of the probe resulting from the electrostatic force to be collected. Figure 2.4 compares the EFM images of Pt nanoislands embedded HfO_2 thin film before and after applying a DC voltage sweep for 50 cycles. The Pt coated conductive probe has been lifted at 50 nm above the surface with a tip bias of +5 V. The phase change profiles along the dotted lines in marked in black (before) and red (after), respectively. A phase jump of the red line in Figure 2.4b indicates an accumulation of positive charges across the circled region in Figure 2.4c, confirming the results obtained via c-AFM images.

2.5 Scanning Tunneling Microscopy (STM)

Another important technique is scanning tunneling microscopy (STM), though it has been rarely reported for studying RS due to the lack of material systems with high conductivity.[20] [52] A recent study by Anja et al.[53] suggests that the generation of metallic filaments resulting from the diffusion of metal ions from the ultrathin oxide layer to the STM tip was responsible for the RS. It has been widely accepted for years that binary transition oxide such as Ta_2O_5 and TiO_2 are purely VCM materials due to the movement of oxygen vacancies under electric field. These STM measurements suggest that the electrochemical metallization process cannot be excluded when explaining the RS in such oxides, thus proposing both ECM and VCM switching phenomenon can be modulated and transformed between the two types, in agreement with the direct observation of Ta channel in HfO_2 memristor.[54] However, corroborating experimental studies have not been completed, so researchers continue

to debate whether the switching mechanism is either purely ECM or VCM, or if both are intimately coupled, considering the conduction characteristics.

2.6 Summary and Remaining Challenges

Rapid developments in nanoscale characterization techniques are advancing our understanding of how ionic and electronic charge transfer phenomena dominate the conduction mechanism, control filament growth, influence size scaling, and the improvement of reliability to push further optimizations in RRAM applications. The complexity of RS comes from the various mechanisms in different types of devices. The observation of metallic filaments in ECM comprising chalcogenides and Cu-SiO_2 has been confirmed by microscopic evidence; however, the intrinsic nature expected in VCM based on the anion mobility is only starting to be debated. In particular, HfO_2 and Ta_2O_5 based RRAM without using the typical electrochemically active metal electrode have been found to show ECM behavior[54] or a transition from VCM to ECM switching modes[55]. Although there are challenges for directly observing the morphology of anions due to the poor contrast between the reduced phase and the oxide matrix, conductive areas displaying orders of magnitude higher conductivity can be readily detected by current imaging or identifying the oxygen concentration variation with advanced characterization. For example, the conducting filament characteristics in HfO_2 based RRAM were recently revealed through a combination of electron holography and *in situ* low-energy-filtered imaging TEM methods, providing direct evidence that the formation and rupture of the filament are dominated by oxygen activity.[54] In order to further identify the mechanisms and understand the operation of the whole test structure nanoscale observation and analyses are necessary.

The underlying RS behavior and charge transfer properties of TaO based memory devices have been reported recently.[56] Here oxygen migration orthogonal to the applied field contributed to the switching phenomenon and was responsible for

the formation of a Ta-rich conducting channel surrounded by a stoichiometric Ta_2O_5 matrix. Thus the surrounding lateral region, in addition to the vertical movement produced by electric field, plays critical role in driving the components and enhancing the formation of the conducting channel. It is necessary to investigate the switching character of materials with different surrounding conditions, where it is expected to induce a change in the primary conduction mechanism in order to relate the active, participating species with the resistive state change. The radial migration of oxygen related species driven by thermal forces has been verified via probing the oxygen transmission intensity using X-ray absorption spectromicroscopy.[57] This study provided the direct observation and nature of the oxygen ion migration in tantalum oxide based memristive devices. How the surrounding region influences the switching character, i.e. whether those regions play essential role in the continuous movement, and where/how the oxygen defects participate requires additional study.

CHAPTER 3

EFFECT OF CONTACT SIZE AND OXYGEN ON TiO_2 MEMRISTOR

3.1 TiO_2 as a Switching Material

TiO_2 nanostructures garner intense interest due to their multi-switching mode, fast operation time, high R_{ON}/R_{OFF} ratio and high cyclic endurance. For virgin TiO_2 devices the RS character remains suppressed until a sufficiently large applied bias induces a conductive path within the insulator layer via electroforming. Vacancy-mediated transport drives the functionality of oxide-based nonvolatile memristive devices. Previous work demonstrated a polarity-dependent electroforming process in the Pt/Ti/TiO_2/Pt system resulting from the drift of oxygen/oxygen vacancies [58] and field-induced electro-reduction effects within Pt/TiO_2-x/Pt devices.[46] Studies of TaO_x thin films showed temperature dependence of filamentary binary oxide RRAM operation during the forming process,[59] [60] while Ta_2O_{2-x} layers exhibited current localization induced during filament formation,[56] resulting in electroforming scaling models.[61] [62] Studies that identify the size-dependent electroforming process of crystalline TiO_2, however, remain underexplored. Following the forming operation, a noticeable change in conductivity through the oxide layer is observed. Various proposed physical and chemical models describing the switching mechanism include the formation and rupture of conductive filaments,[63] the modulation of the Schottky-like barrier at the metal/oxide interface,[6] and trap-controlled space charge limited current along the oxide junction,[56] thus obfuscating the predominant underpinning mechanism. For oxide memristive devices, however, the content of oxygen vacancies

is universally considered one of the key factors affecting the switching behavior.[64] [65]

This work presents the direct correlation between variations in fabrication and annealing environment with the resultant electroforming, set, and reset voltages in TiO_2-based thin film nanostacks. This study also presents the influence of varying electrode sizes on the electroforming operation voltage and resistive switching properties across nanoscale $TiO_2/Nb:SrTiO_3$ junctions. The nanostructures displayed effective switching behavior, possessing highly stable and reproducible high resistance state (HRS) to the low resistive state (LRS) ratios (R_{HRS}/R_{LRS}) as large as three orders of magnitude. Comparing the I-V character of samples with diameters ranging from 200 to 500 nm shows that increasing size results in decreasing reset voltages and increasing R_{HRS}/R_{LRS} ratios. Moreover, this study demonstrates that the switching polarity can be reversibly changed between eight-wise and counter eight-wise due to variations in available oxygen vacancies, as controlled by the oxygen flow ratio during the deposition and post-annealing processes.

3.2 Device Fabrication

Oxygen-deficient TiO_2 thin films were grown on 0.7 wt% Nb-doped $SrTiO_3$ (Nb:STO) (STONba050505S1, MTI Corp.) single crystal substrates with resistivity of 0.007 ohm-cm using DC magnetron sputtering at 700°C, from a 99.9% purity Titanium target. The substrates were annealed at 950°C for 1 h after wet etching in aqua regia ((HCl (A144-212, Fisher Scientific.): HNO_3 (SHBD9358V, Sigma-Aldrich.) 3:1)) for 12 mins. Non-stoichiometric TiO_2 deposition was obtained in a mixed argon and oxygen atmosphere under various oxygen flow rates (25%- 60%) at a base pressure 10^{-6} Torr. The nominal thickness of the TiO_2 layer is approximately 15 nm. Nanoscale circular patterns from 50 nm to 1 μm were fabricated using e-beam lithography (JEOL JSM-7001F; EBL). Both Ti adhesion and a Pd capping layers were deposited suc-

cessively on both sides of the sample by DC sputtering, followed by a lift-off process to form the top electrodes. The topography of the nanostructures was characterized by Atomic Force Microscopy (Oxford Instruments/Asylum Research Cypher ESTM; Goleta, CA). All conductive AFM (c-AFM) electrical measurements utilized a platinum/titanium-coated silicon AFM tip (ASYELEC-01; Asylum Research; Goleta, CA) with a cantilever force constant of 2 N/m. Application of conductive silver paste (TED PELLA, INC; Leitsilber 16035) provided an Ohmic contact between the bottom electrode and the sample disk.

Figure 3.1 shows a representative topographic image of a highly-ordered dot electrode array ranging in diameter from 100 nm to 900 nm as fabricated by e-beam lithography. The cross-sectional profile, corresponding to the electrode in Figure 3.1a shows the height of the Pd/Ti electrodes on TiO_2 layer about 50 nm. Figure 3.1b shows the schematic illustration of sample structure and the electronic characterization setup. During c-AFM measurements, the bias was applied to the bottom of the sample, and the resulting currents were collected by a grounded tip (top) electrode connected to a dual-gain transimpedance amplifier cantilever holder (ORCA^{TM}; Asylum Research, Goleta, CA). A compliance current of 10μA was used to prevent the permanent hard breakdown of the device. The nanostack displayed non-volatile bipolar RS character and "counter-eightwise" type switching behavior, which exhibits a transformation from HRS to LRS and LRS to HRS at negative and positive biases, respectively.[66]

3.3 Area Dependent Resistive Switching Behavior

To investigate the area-dependence of the forming process we applied a sweep voltage in the negative branch from 0 to -10 V with the identical increasing step-interval for each device. The tip-induced electrical bias can be uniform applied to each pattern thus providing a reliable current sensing technique for nanoscale devices. Figure

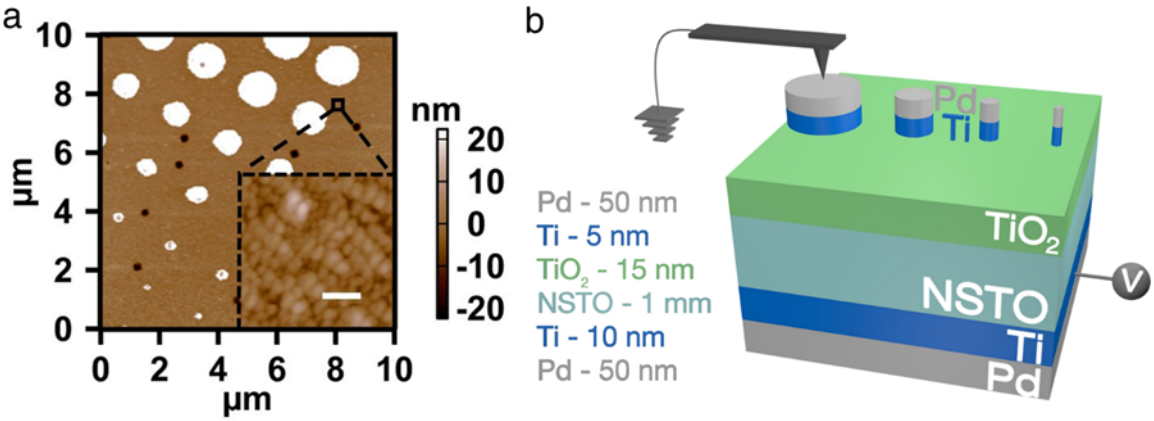

Figure 3.1. a, An AFM topography image of the highly-ordered electrode pattern. The inset shows the topography of a 400 nm x 400 nm zoomed-in region. The scale bar represents a length of 100 nm. b, Schematic drawing of the I-V measurement setup. The conductive AFM probe is ground while the bottom electrode is biased in this work.

3.2a presents a comparison of the I-V curves of different contact diameters (d = 100 nm - 600 nm). Contact diameters smaller than 100 nm exhibited no sudden current increases typically associated with the initial electroforming process after the first cycle, which is attributed to insufficient switching fields result from the instrument limitation of 10 V. Contact diameters between 100 nm - 600 nm display clear, size-dependent changes in their respective forming voltages. Switching induced by the 100 nm diameter contact occurred at approximately -9 V with decreasing forming voltages observed for increasing contact sizes. As the contact diameter approaches the microscale no forming process required for taking place the switching phenomenon. Figure 3.2b shows a semi-log plot of the average forming voltage as a function of contact area taken of ten devices measured for each size. The plot shows a linear correlation between increasing contact area and decreasing forming voltage exist for these mesoscale electrodes, comparable to the trends recently observed in (10nm-1μm) Hf/HfO_x crossbar resistive RAM[59] and TiO_2 nanocrosspoint junctions.[62] A positive bias applied to the top electrode during the initialization process results in local redox reactions and ionic migration. These phenomena heavily reduce the Ti/O

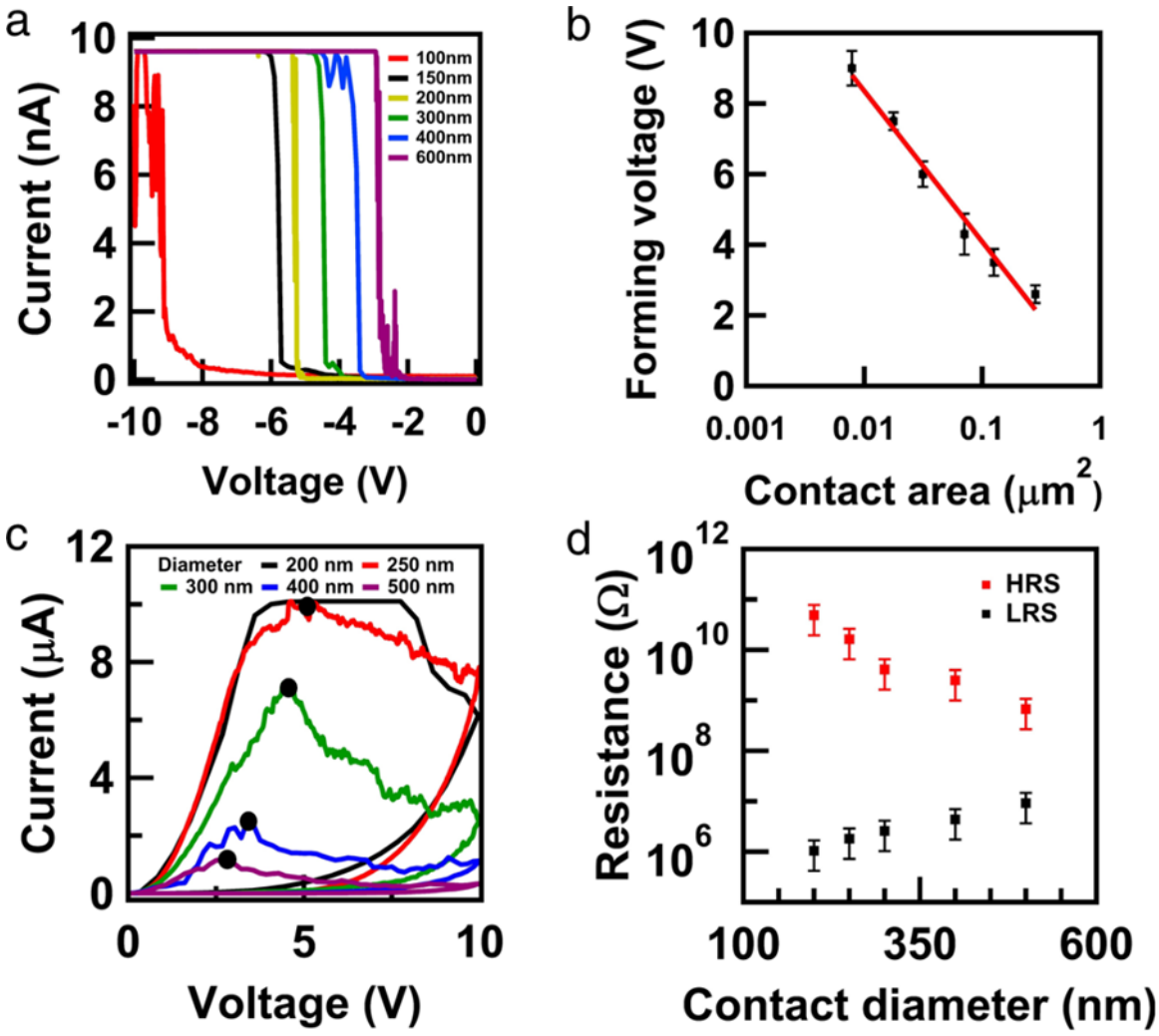

Figure 3.2. a, I-V curves of electroforming as a function of contact diameter between 100-600 nm. b, A semi-log plot of forming voltage VF versus the contact area ln(A), displaying a linear relationship. The errors for ten selected sizes of different diameters are at 10% ± 5%. c, Representative I-V responses of varying interface diameters showing a significant decrease of reset voltage with increasing contact size. The markers estabilish the point in terms of the voltage at where the reset process occurs. d, The resistance versus contact diameter for HRS and LRS read at -1V, indicating a decrease of the R_{HRS}/R_{LRS} when increases the contact size.

ratio and consequently create an appreciable density of oxygen vacancies near the Ti/TiO_2 interface.[6] Assuming a uniform electric field confined to the region under the electrode, the associated defects will migrate randomly across the entire device along the most favorable diffusion paths (i.e. grain boundaries). Increases in the number of grain boundaries under larger area electrodes facilitate the formation of the filamentary conductive path during electroforming process.[59] A larger electric field or a longer time is therefore required to initiate the electroforming process when the involved grain boundaries are relatively reduced. The topography of the deposited TiO_2 layer confirms that the grain sizes (20 ± 10 nm) are indeed much smaller size than the top electrode diameters. Figure 3.2b shows the fitting results for VF versus ln(A), displaying a clear, linear relationship. This consists with the simulation results presents by other groups. For contacts of equal size, however, the number of available vacancies plays a more critical role. If we consider a fixed number grain boundary for contacts of identical size, then modulating the amount of available oxygen vacancies is achieved by varying the oxygen gas partial pressure.

Figure 3.2c shows the I-V character for five chosen contact sizes under positive applied bias. No sudden increases in current are observed but rather a gradual transition from HRS to LRS for all sizes. This phenomenon is likely attributed to oxygen vacancy migration and resultant barrier modulation at the TiO_2/Nb:STO interface. Here the current increases incrementally with continual decreases in the barrier height, suggesting that the redox reactions occur during the switching process. The junction of 200 nm displays resistive switching with a reset voltage of 5.5 V and a large R_{HRS}/R_{LRS} ratio greater than 10^4. For a 250 nm diameter the reset voltage reduced to 5 V, and the R_{HRS}/R_{LRS} ratio slightly decreases to 10^4. The contact size of 300 nm exhibits a reset voltage of 4.7 V and an even smaller R_{HRS}/R_{LRS} ratio of $\sim 10^3$, which is then reduced again to only 2.9 V and ~ 100, respectively, for contact diameters of 500 nm. As shown in Figure 3.2d, the resistance at LRS increases slightly while at

HRS decreases, resulting in significant decreases of the resistance ratio about three orders of magnitude with increasing contact diameter. On one hand, smaller contact induces higher built-in electric fields, which alter local defect concentrations.[67] Therefore, due to the opposing signs of the applied external field and built-in electric field contributions, smaller contact sizes require larger voltages to induce the movement of oxygen vacancies. This explains the observed reduced reset voltage for the larger contact area. On the other hand, decreasing size of the electrodes leads to high electric fields at the edges which could dominate the SET process, for example, producing switching to LRS with a larger leakage current. We also observed differences of the loop area during the reset process, indicative of changes to the dissipation energy.[67] The decrease of the loop area indicates a decrease in power dissipation as interface areas decrease, which results from higher electric fields under smaller interfaces. The decrease in LRS resistance with interface diameter corresponds to larger filaments formed under larger contact areas.[64] Note that larger filaments generate higher Joule heating and further increase oxygen vacancy transport.[68] As such, higher reset currents and voltages are measured for smaller contact areas.

3.4 Oxygen/Argon Flow Effects

To further investigate the effect of oxygen vacancies on the RS behavior, we compared the hysteresis loops of 200 nm diameter nanostacks prepared under different oxygen flow ratios (O_2/(O_2+Ar); 20%-60%) as shown in Figure 3.3. Here the higher-oxidized sample shows a larger SET voltage and higher R_{HRS}/R_{LRS} ratio. By decreasing the oxygen flow ratio during deposition from 60% to 20%, the set voltage is reduced by 4V and the resistance ratio dropped two orders of magnitude. As shown in Figure 3.3b, the LRS resistance displays some modest fluctuation while the HRS resistance exhibits a three order of magnitude increase with increasing oxygen flow ratio, subsequently enhancing the resistance ratio significantly. This results from

variations in the amount of oxygen vacancies present. As discussed previously, the Schottky-like barrier at the TiO_2/Nb:STO interface is typically induced by high concentrations of Nb-dopants and oxygen vacancies within Nb:STO.[66] Since the carrier concentration in Nb:STO is much greater than that of TiO_2, the increased oxygen vacancy concentration resulting from decreasing the oxygen flow ratio consequently lowers the barrier height. Therefore, the HRS resistance becomes much more sensitive to the oxygen flux due to the strong dependence of leakage current on the vacancy concentration.[62]

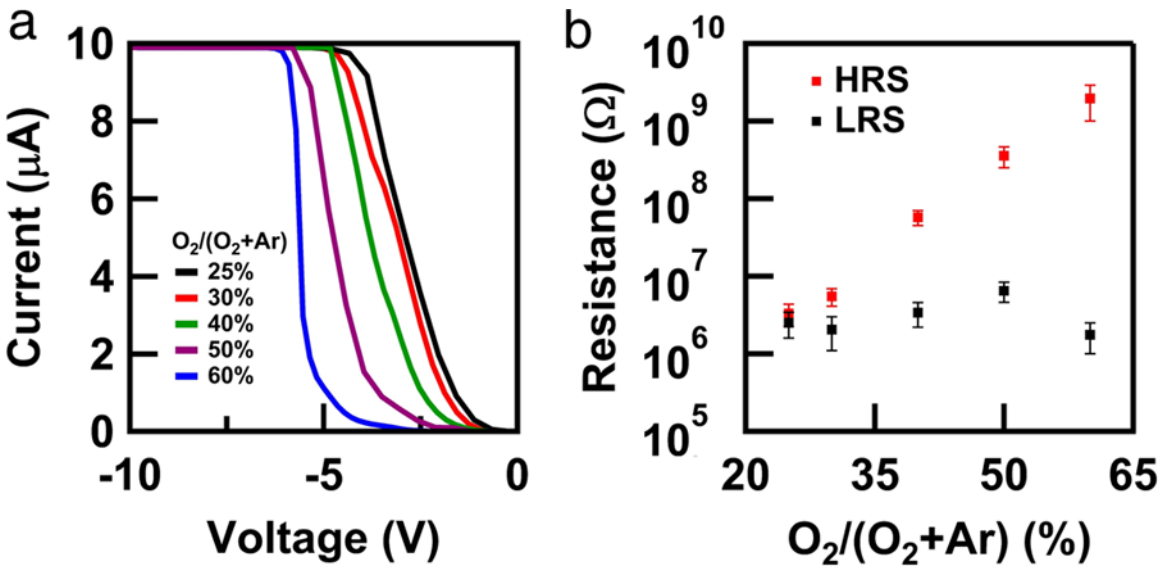

Figure 3.3. a, Representative dependence of onset voltage on oxygen flow rate at total gas flow rates (25% - 60%). b, The resistance versus oxygen flow rate for HRS and LRS.

In contrast to the area dependent case, however, the I-V curves here display no discernable variation in reset voltage, as both the electroforming and resultant filament formation processes are strongly driven by electric field. This confirms that during the reset process the migration of accumulated oxygen vacancies towards the top electrode depends more on the Joule heating effect rather than the contact size. Note that the stability, in terms of retention or endurance performance, improved within samples with increased oxygen content. As shown in Figure 3.4, wider fluctu-

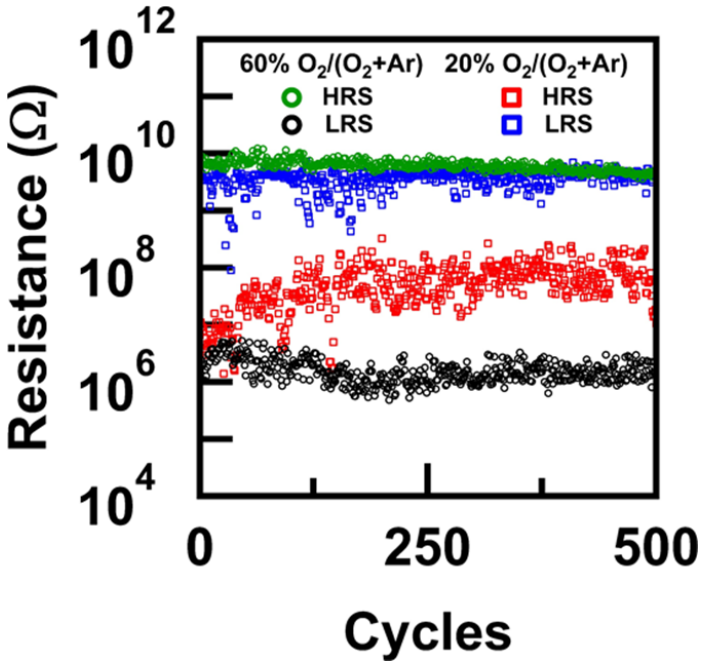

Figure 3.4. Switching endurance of 500 cycles voltage sweep at a read voltage of -1 V for 20% and 60% oxygen partial flow rate, which shows a significant improvement of the stability when reduces the oxygen vacancies.

ations occur as the oxygen content decreases, leading to a random and unpredictable switching process. This instability is likely attributed to various TiO_2 Magnéli phases induced under different oxygen nonstoichiometry.[69] [70] Thus, for nonstoichiometric TiO_2 the oxygen vacancies tune the conductive properties and simultaneously represent the critical obstacle to the stability.

3.5 Polarity Reversal Across Oxide Interfaces

To compare the I-V characteristics of TiO_2 thin films possessing the amount of oxygen vacancies at the extremes, we conducted local current measurements across junctions of identical 200 nm contact diameters after annealing in vacuum (10^{-6} Pa) at 450° for 1.5 hours and reannealing in O_2 condition (high pure) for the same period. Figure 3.5 shows the I-V characteristics of the single sample as-prepared (black), after the vacuum anneal (blue), and after reannealing in oxygen (red), respectively.

The nanostack displayed a higher current than the as-prepared state after the introduction of oxygen vacancies during the vacuum (O_2-poor) anneal. Interestingly, the nanostack exhibits changes in the LRS to HRS and HRS to LRS direction after application of positive voltages and negative voltage, respectively. This phenomenon corresponds to the "eightwise" type switching. Polarity reversal from "eightwise" to "counter-eightwise" switching, however, is observed after reannealing the sample under O_2-rich conditions. Previous reports of other oxide systems observed two types of bipolar switching coexisted within a single cell,[15] [21] [71] [72] [73] with proposed mechanisms ranging from device symmetry to changes in the active interface position explaining the polarity reversal phenomenon. There are two possible factors that result in the observed reversibility, one that involves the role oxygen vacancies play during switching process, and another involving variations in oxygen vacancy distributions induced by post-annealing. As-deposited, oxygen vacancies randomly distribute throughout the oxide thin film layer. Subsequently, oxygen vacancy migration toward the TiO_2/Nb:STO interface reduces the barrier under the application of positive bias to the top electrode. In this case, the modulation of Schottky barrier by the movement of oxygen vacancies dominates the conduction mechanism. The following vacuum annealing process increases the oxygen vacancy concentration, thus enabling the trap/detrap effects that cause the polarity conversion, as previously demonstrated in Au/Sr_2TiO_4/Nb:STO junctions possessing Au/Sr_2TiO_4 active interfaces. Switching behavior returns to "counter eight-wise" after reannealing under pure oxygen conditions. This can be explained by the fact that the migration of oxygen vacancies is favored in less defective switching layer which results from the oxidation process during annealing. The different roles oxygen vacancies play during both switching modes is illustrated by the schematic band diagrams in Figures 3.6a-d. In less defective layers the oxygen vacancies are more likely to migrate under electric field from the Ti/TiO_2→TiO_2/Nb:STO interface under positive bias (Fig.

3.6a; HRS→LRS) and from the TiO_2/Nb:STO→Ti/TiO_2 interface under negative bias (Fig. 3.6b); LRS→HRS). During eightwise switching, increases in the amount of available oxygen vacancies provide a high concentration of trap sites that modulate the Schottky-like barrier at the TiO_2/Nb:STO interface. Electron injection into the traps occurs at the interface under positive bias (Fig. 3.6c; LRS→HRS). Electrons are released from the traps along the interface into NSTO under negative bias (Fig. 3.6d; HRS→LRS).

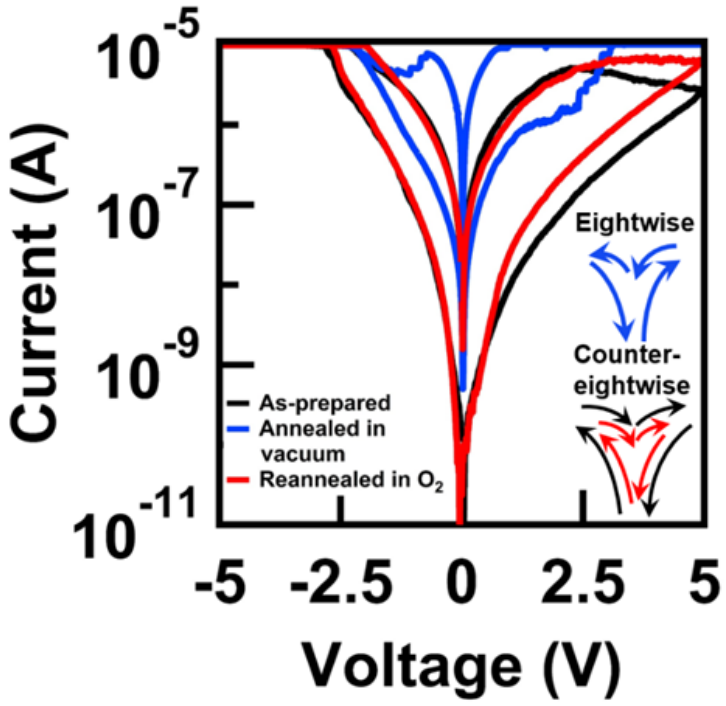

Figure 3.5. The I-V character of a 60% oxygen flow ratio sample as-prepared (black), after annealing in vacuum (blue), and reannealed in ambient oxygen (red); inset - an illustration of the switching polarity for the three conditions, highlFighting the reversibility of the switching mode between eightwise and counter-eightwise.

3.6 Summary of Chapter 3

The potential scalability to the nanometer regime is expected for future high density integration. It is well known that the active device area is defined by a

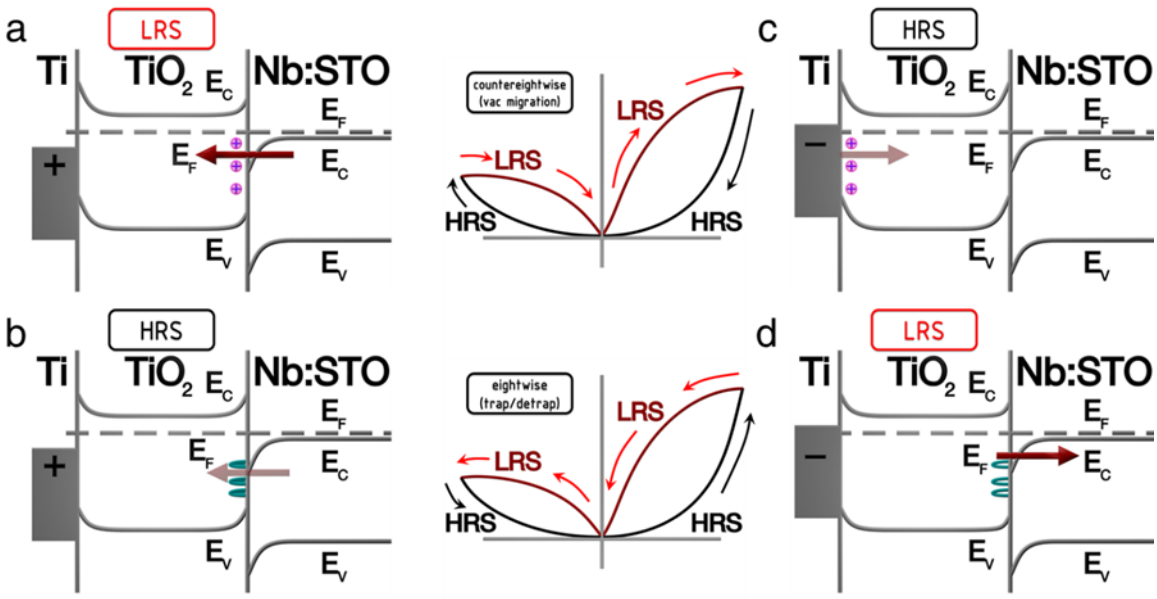

Figure 3.6. Schematic illustration of band diagram of a,b, Oxygen vacancy migration for "counter-eightwise" type switching and c,d, electrons trap/detrap at TiO_2/Nb:STO interface for "eightwise" type switching.

single conducting filament, which can be as small as a few atomic units, and that different underlying mechanisms are responsible for filament formation. In recent years, intense efforts have been expended to scale down the device dimension to sub-100 range by nanoimprint lithography and e-beam lithography,[74] however, further scaling is still facing the resolution limit of lithography or etching techniques. In addition to minimizing the feature size of the device, it is important to retain the performance while scaling. In fact, devices may lose their uniformity or reliability when scaling to extremely small sizes, thus research must prioritize understanding the correlation between scalability and performance optimization.

The I-V character of Pd/Ti/TiO_2/Nb:STO/Ti/Pd nanostacks were measured locally as a function of contact diameter and oxygen flow ratio. The electroforming voltage exhibits a linear dependence on logarithm of contact diameter due to an increased number of grain boundaries as the electrode area increased. The linear trend between reset voltage and contact area in log scale demonstrates the influ-

ence of varying filament sizes and resultant Joule heating conditions. Controlling the oxygen flow ratio during deposition alters the amount of available oxygen vacancies and subsequently modulates the Schottky barrier height, resulting in significant variations in onset voltage and R_{HRS}/R_{LRS} ratio. Changes in available vacancies also cause reproducible, reversible changes in switching polarity between eightwise and counter-eightwise modes. These results reveal significant design implications for scaling oxide-based resistive switching nodes that require controlling defect distributions via deposition processes to alter overall device performance.

CHAPTER 4

SOLUTION-PROCESSED MEMRISTORS

4.1 Importance of Nanocrystals

Zero-dimensional nanostructures received a significant boost over the last decade with the advancement of high-performance and unique properties resulting from the quantum phenomena. While the fabrication and characterization of resistive switching oxide thin films,[69] [75] [76] [77] nanoparticles,[78] and nanowires [79] have received considerable attention, the development of rapid and low-cost solution-processed alternatives to complicated multi-step lithographic approaches remains stunted. The low/high resistance states (LRS; HRS) across metal-oxide interfaces within the conventional metal-insulator-metal structure, as reduced to true nanoscale dimensions, become greatly influenced by concomitant local electric field effects,[67] Schottky barrier modulation,[15] [80] and defect distribution dominated transport.[42] In order to harness unique size-dependent resistance phenomena, other recent studies demonstrated resistive switching character within vertically-aligned carbon nanotubes,[81] individual perovskite nanotubes,[82] binary oxide nanowires[79] and individual TiO_2 nanoparticles.[78] Studies involving these quasi-zero dimensional and one-dimensional nanostructures remain rather scarce as device fabrication involves complicated multi-step lithographic processes or suffer from the lack of order or periodicity requisite of memory architectures. Many studies of charge transport within solution-processed semiconductors such as colloidal CdSe quantum dots and PbS photovoltaic nanoparticles exist,[83] [84] however few studies demonstrate resistive switching between nanoparticles, where the ligand interparticle interface profoundly affects the

response.[85] [86] Studies of the memristive character of individual, sol-gel produced TiO_2 nanoparticles revealed both complementary and bipolar switching character that exhibited high sensitivity to annealing and partial redox processes involving the sub-stoichiometric core.[78] Ag/Ag_2Se nanoparticle film/Au[87] and Ag/Ag_2Se NP/MnO NP/Au bilayer devices[88] exhibited low power consumption, high retention, and high endurance properties that were retained upon the application of $\pm$ 0.4% stress states. Most studies of resistive switching within colloidal systems observe the electrical characteristics of spin-coated films comprising binary oxide[89] or perovskite complex oxide[90] nanoparticles, dip-coated thin films,[91] [92] [93]or compact pellets.[94] These assemblies are annealed, forming dense structures free of ligands. Other approaches use electrostatic accelerating voltage during film growth to induce interparticle bonding.[95] These studies remove the ligands between the nanoparticles, effectively transforming the low-dimensional nanostructures into thin films. To improve the performance of solution-processed memristive systems the correlation between changes in ligand chemistry and properties such as operating voltages, device stability, and switching type must be systematically evaluated.

In this study we have demonstrated memristive behavior in nanoribbons comprising perovskite strontium titanate ($SrTiO_3$) nanocubes capped with oleic acid that either retained or altered its switching mechanism upon transfer from the original substrate to a second, arbitrary substrate.[96] Subsequent studies extend to systematically compare the dependence of resistive switching behavior on ligand length within individual HfO_2 nanoribbons capped with oleic, dodecanoic, and undecenoic acid. Hafnia, HfO_2, is a prototypical resistive switching binary oxide that exhibits excellent scalability, reliability, and CMOS compatibility in both amorphous and crystalline form.[97] Here a facile, low-cost method is used to prepare highly ordered nanoribbon arrays comprising single-crystalline HfO_2 nanocrystals via convective self-assembly. This approach addresses typical issues facing nanocrystal assembly (i.e. scalability

and periodicity) to produce ordered nanostructure arrays without the complexity of fabrication templates or lithographic patterning.[98] The HfO_2 nanoribbons exhibited both threshold switching (TS) and bipolar resistive switching (BRS) induced by manipulating the conductive filament morphology, similar to recent studies of NiO thin films.[99] Both the forming voltage and SET voltage scale with ligand length, suggesting that the interparticle tunnel distance heavily influences the carrier transport within HfO_2 nanoribbons. Motivated by these results, we finally demonstrate the fabrication and characterization of a solution-processed hafnia thin film device that exhibits lower operating voltages, higher uniformity, and larger ON/OFF ratios than its ALD-prepared counterpart.

4.2 Synthesis and Assembly of Nanocrystals

4.2.1 Colloidal STO Nanocrystal Synthesis

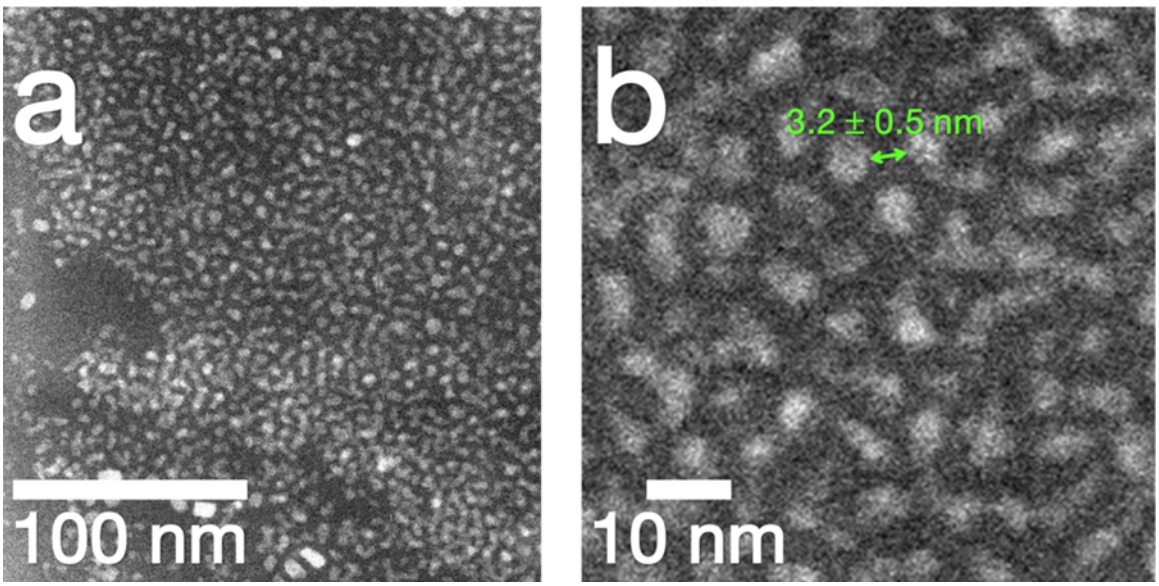

Figure 4.1. High angle annular dark field (HAADF) TEM images of a, monolayer nanoribbon segments displaying b, an average interparticle distance of 3.2 ± 0.5 nm.

Colloidal undoped $SrTiO_3$ nanocrystals (STONCs) were prepared using a modified hydrothermal method without hydrazine as prepared by the Kittilstved group.

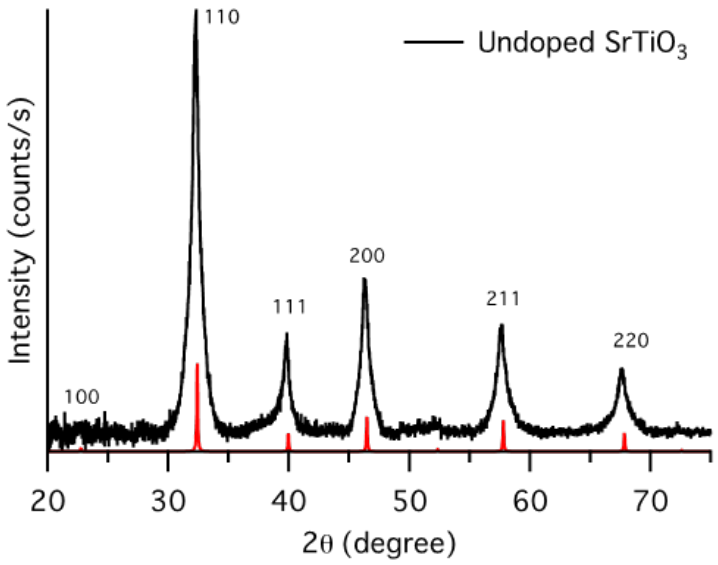

Figure 4.2. Powder X-ray diffraction patterns of undoped $SrTiO_3$. The grain sizes estimated from the Scherrer equation are 15 nm for $SrTiO_3$. The red lines indicate the powder diffraction pattern of bulk $SrTiO_3$.

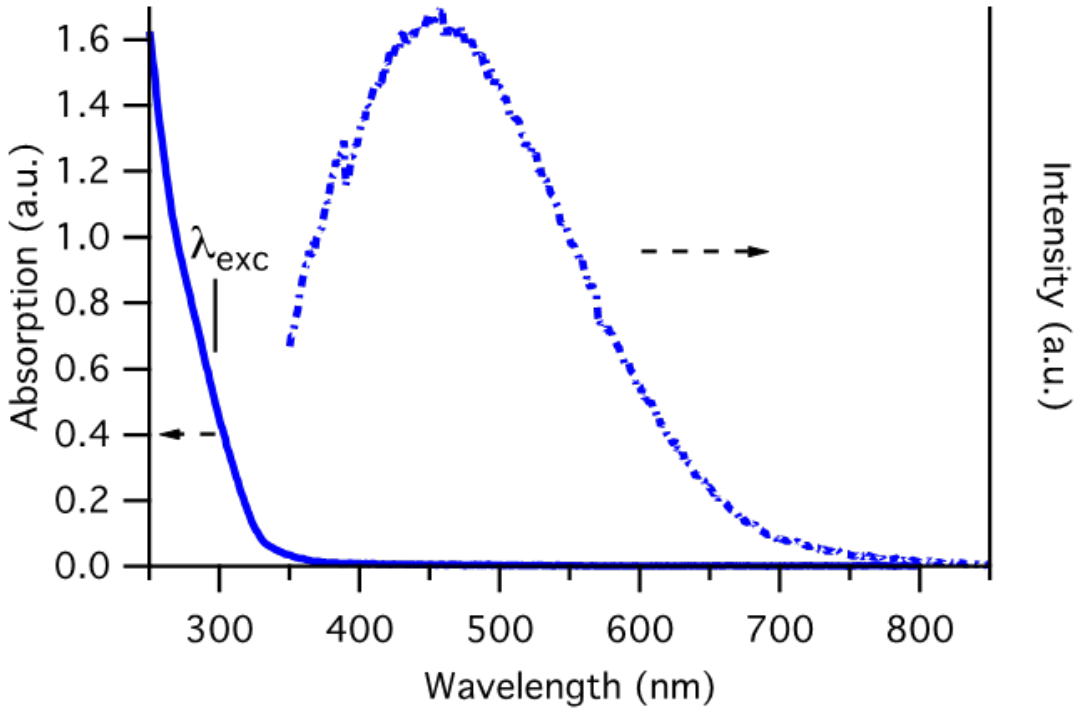

Figure 4.3. Room temperature absorption spectra of $SrTiO_3$ suspended in Hexanes (Solid blue line). Uncorrected emission spectra excited at 300 nm (dashed).

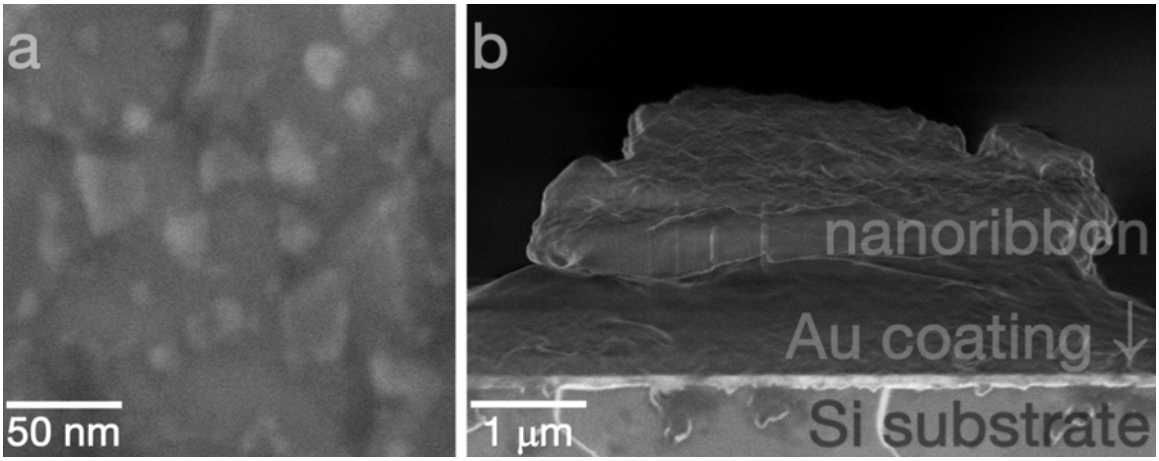

Figure 4.4. a. top view and b. cross-sectional SEM images of a STONC nanoribbon, respectively.

Nanocrystals were characterized using powder X-ray diffraction (Figure 4.2), absorption/emission (Figure 4.3) and TEM (Figure 4.1). The nanocrystals display a broad emission peak centered at ∼465 nm that has is assigned to self-trapped excitonic emission associated with oxygen vacancies. The powder X-ray diffraction pattern of these nanocrystals display only the cubic perovskite phase of strontium titanate. Figure 4.1a shows high resolution TEM images (JEM 2200FS-JEOL) of colloidal STONCs deposited on a 3 nm carbon film supported on 400 mesh copper TEM grids (Electron Microscopy Sciences). HAADF-TEM images of a STONC nanoribbon (Figure 4.4), the image shows the boundary edge of the nanoribbon. The images were obtained at room temperature, using ultrathin carbon film on lacey carbon support film (3nm thickness), 400 mesh copper grid (Ted Pella, Inc.) and a JEOL 2200FS EFTEM unit at an accelerating voltage of 200 kV. TEM analysis reveal that the nanocrystals are cuboidal with average edge dimensions of ∼10 ± 2 nm. The nanocrystal concentration was estimated from analysis of the Ti concentration obtained by inductively coupled plasma optical emission spectroscopy (ICP-OES, PerkinElmer 4300 DV) and the average particle size from TEM, which yielded a particle concentration of 25 μM (micromolar, 10^{-6} mol/L). This was determined by dissolving 1 mL of the particle

in 20 mL of aqua regia and then using ICP-OES by the standard addition method. The concentration obtained is for the total titanium concentration in the unknown stock solution. The estimate is then based on the average particle size the number of Ti atoms per STONC and then divide the total Ti concentration by this number (∼1100 for a 9 nm cube) to obtain this particle concentration

4.2.2 Hafnia Nanocrystal Synthesis

HfO_2 nanocrystals (0.4 mmol HfO_2) were synthesized by Jonathan De Roo at Columbia University from HfCl4 and benzyl alcohol in a recently developed solvothermal process.[100] [101] After solvothermal synthesis and washing with diethyl ether, the nanocrystals are redispersed in chloroform (4 mL). Then, 0.2 mmol fatty acid (oleic acid, dodecanoic acid, or 10- undecenoic acid) was added to the milky suspension. In case of 10-undecenoic acid, 5% of dodecanoic was also added to ensure colloidal stability. Under stirring or ultrasonication, oleylamine (0.15 mmol or 50 μL) was added until a transparent and colorless suspension was obtained. Finally, the particles are purified three consecutive times by adding acetone to induce precipitation, followed by centrifugation and resuspension in chloroform. After the last purification, the nanocrystals were dispersed in toluene.

4.2.3 Nanoribbon Stop-and-Go Assembly

Nanoribbon Stop-and-Go Assembly The "stop-and-go" flow coating method described previously[98] was used to create STO nanoribbons from colloidal STONCs building blocks. The custom-built instrument uses a poly(ethylene terephthalate) film (82 ± 7 μm in thickness, supplier McMaster-Carr) as a flexible blade, with a "scored" region (2 mm) at the edge. This blade is attached to an adapter with pitch and roll variability, allowing the scored region of the blade to be aligned parallel to a substrate and brought into contact. The substrate is attached to a nanopositioner (Burleigh Inchworm controller 8200), which is programmed to perform a series of stop-and-go

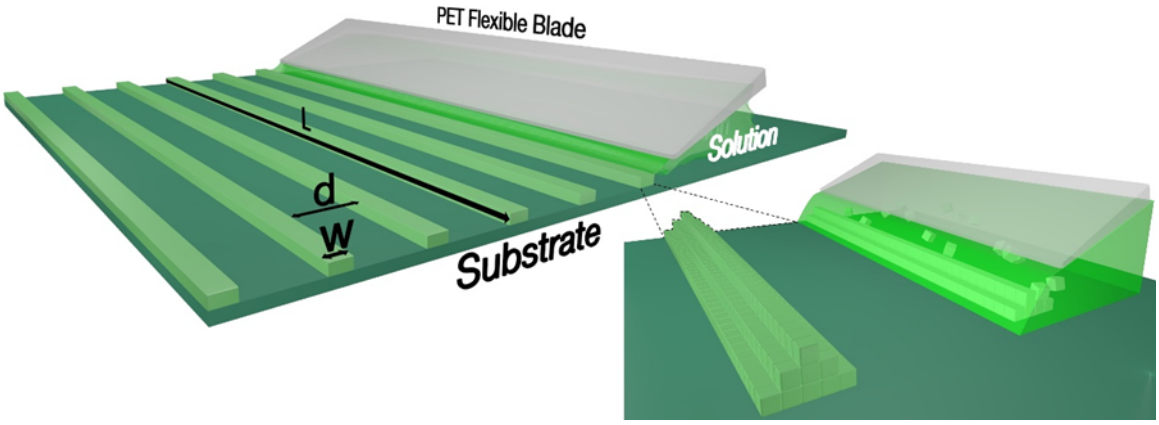

Figure 4.5. An illustration of the stop-and-go flow coating process. The inset provides an illustration highlighting the long, bell-shaped nature of the STONC nanoribbons.

steps, with stop time (td), velocity (v), and spacing (d) as user-defined variables. STO colloidal solution (8 μL) is injected between the substrate and scored region of the blade. The capillary forces confine the injected solution to the scored region and meniscus height is dictated by the capillary interactions. STO nanoribbons are flow coated on commercially available Nb-doped STO (0.7 wt % Nb, MTI Corp.) and silicon (P(100) 0-100 ohm·cm; single-side polished; University Wafer Inc.) substrates. The height and width of the ribbon can be precisely controlled from nanoscale to bulk dimensions by varying the stop time of the stop shift, thus enabling the direct fabrication of nanostructures ranging from individual nanoribbons to thin films.To deposit HfO_2 nanocrystals, the similar approach was applied while a silicon wafer (University Wafer Inc.) cut to an edge length of 15 mm used as a fixed blade. The HfO_2 nanoribbons in this study were prepared using the following parameters: v = 1500 μm/s, solution concentration = 1 mg/mL, d = 200 μm, and a td between 1000 and 6000 ms. Different stop times were used to vary the nanoribbon height (h) and width (w), td = 1000 ms (h = 80 nm, w = 8 μm), td = 3000 ms (h = 160 nm, w = 13 μm), and td = 6000 ms (h = 230 nm, w = 17 μm). A fixed volume of 1 mg/mL HfO_2 NC solution (10 μL) is injected between the fixed blade and the substrate, where

capillary forces confine the solution to the blade edge. The HfO_2 NC nanoribbons were deposited directly on silicon wafer substrates (undoped <100>, University Wafer Inc.) coated with 5 nm Ti/30 nm Pt thin films. Before deposition, all substrates and blades were rinsed with isopropyl alcohol and toluene and then dried after each step with a filtered stream of N_2 gas.

Figure 4.6 shows the nanocrystalline morphology of the HfO_2 nanoparticles and schematic illustration of the 'stop-and-go' flow coating method. The transmission electron microscopy (TEM) image of HfO_2-D in Figure 4.6a shows the as-prepared nanocrystal structure, while the inset shows a high-resolution TEM image that indicates NC dimensions on the order of 5 nm. The x-ray diffraction (XRD) in Figure 4.6b reveals the phase pure, monoclinic structure of HfO_2 NCs. The stop-and-go flow coating method, as illustrated in Figure 4.6c, deposits nanoparticles onto a hard substrate by flowing a NC solution under the rigid silicon blade. The height and the width of the ribbon can be precisely controlled from nanoscale to bulk dimensions by varying the stop time of the stop shift, thus enabling the direct fabrication of nanostructures ranging from individual nanoribbons to thin films. The optical microscopy image in Figure 4.6d shows highly ordered arrays of individual HfO_2 nanoribbons prepared by 'stop-and-go' flow coating. Figure 4.6e shows the three-dimensional topographic profile of an individual HfO_2 nanoribbon collected via atomic force microscopy (AFM), indicating that nanoribbons possess a wedge-like cross sectional profile, with an average width of 8 μm and an average height (maximum; top of the wedge) of 100 nm.

Figure 4.7 demonstrates an optical micrograph (scale bar: 500 μm) showing highly scalable arrays of STONC nanoribbons (length = 1.5 cm) with highly regular periodicity. A plot of STONC nanoribbon height and width dimensions versus the stop time of the flow coating process, illustrating the scaling trend of the approach. Both height and width of the ribbon increase with increasing stop time, displaying a linear

relationship and thus indicates a highly scalability of the flow coating approach. By varying the stopping distance, the width of the ribbon can be simply extended to thin film scale, favoring the solution processed device manufacturing.

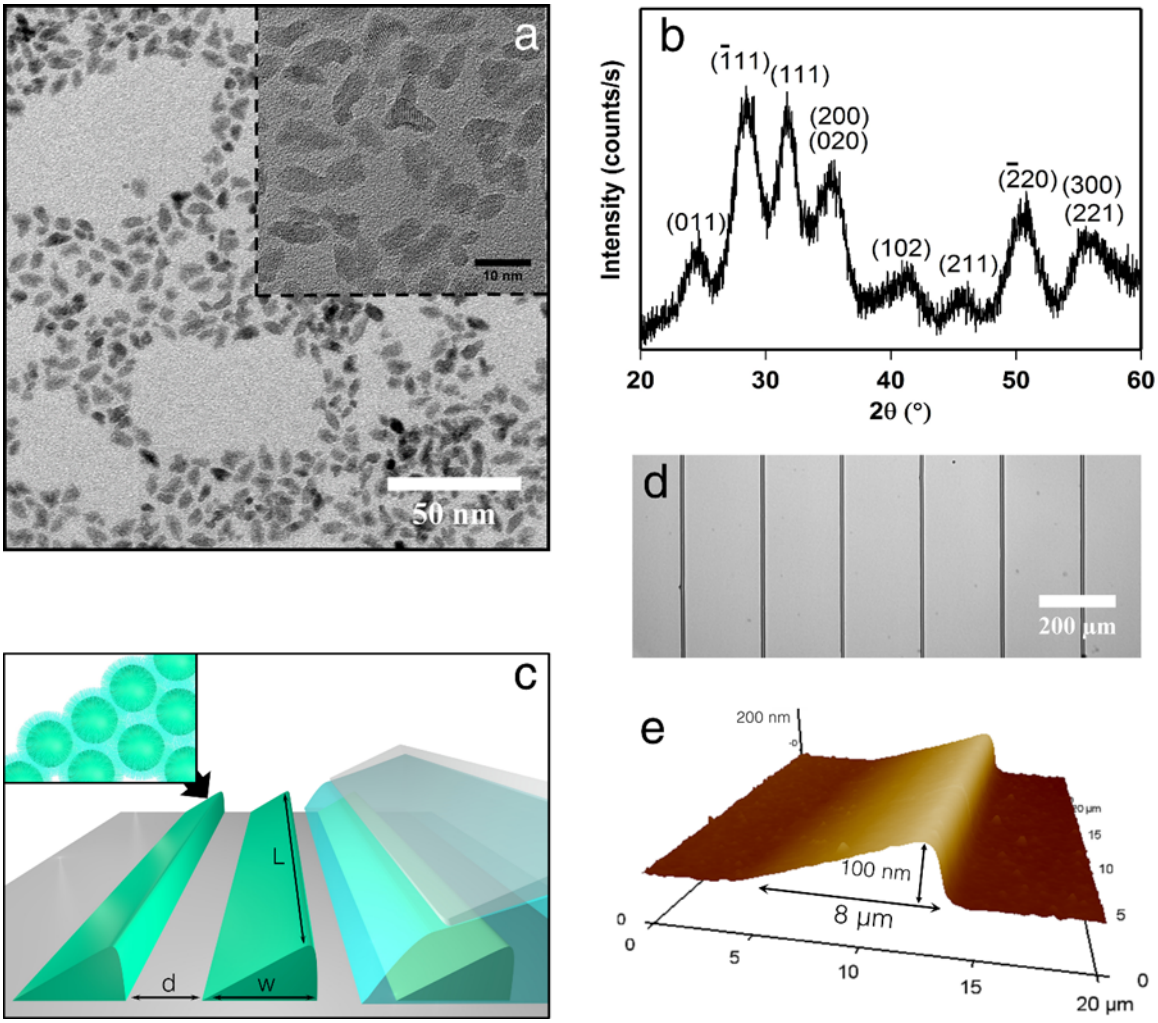

Figure 4.6. a, TEM image shows the crystalline structure of HfO_2 nanoparticles with the scale bar denotes 50 nm. Inset: HRTEM image of NCs indicates the lattice fringe and size of 5 nm. b, X-ray diffraction patterns of monoclinic HfO_2. c, An illustration of the "stop-and-go" flow coating process. Inset shows the assembly of the NCs driven by solvent evaporation. The shape and profile of the ribbon are confirmed by d, three-dimensional AFM image. e, An optical micrograph (scale bar 200 μm) showing highly ordered ribbons comprising HfO_2 nanoparticles. The width and height of the wedge are approximately 8 μm and 100 nm, respectively.

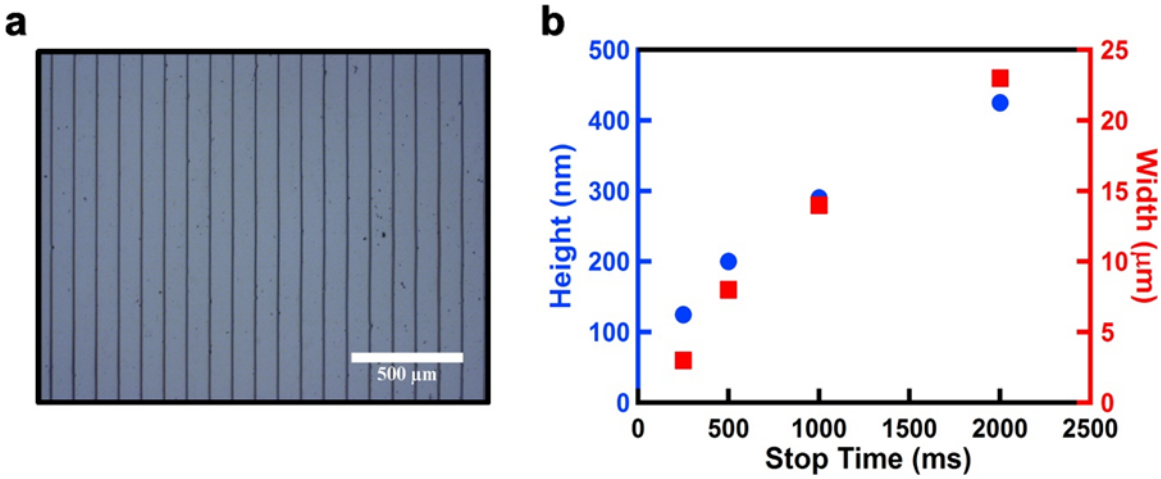

Figure 4.7. a, An optical microscopy (scale bar: 500 um) showing highly scalable arrays of STONC nanoribbons (length = 1.5 cm) with highly regular periodicity. b, A plot of STONC nanoribbon height and width dimensions versus the stop time of the stop-and-go process.

4.3 Tip-Induced Current Measurements

Conductive AFM (c-AFM) is a powerful tool for studying RS behavior with the ability to spatially resolve local heterogeneities within the electronic response, and probe the current distribution simultaneously.[38] [40] [78] The electrical measurement was conducted at room temperature on ORCA-Conductive AFM (Cypher ES, Asylum). A silicon probe with Pt/Ir tip coating with a frequency of 70 KHz and a spring constant of 2 N/m (ASYELEC-01) was used. Each bottom electrode was attached to the sample holder via silver paint (TED PELLA, INC.) to form an electrical path between the sample bias and the sample surface. During the measurement, the sample was biased between +/- 10 V at the bottom electrode using while the tip is held at 0 V potential. Current was collected through the tip and subsequently passed through a dual gain ($ORCA^{TM}$) transimpedance amplifier. Prior to I-V measurements, the topography of the sample surface was taken in AC mode. To do a local I-V plot, the tip was moved to a different position of the ribbon and engaged to it with a set point of 0.02 V. In the initial electroforming, a negative voltage of -10

V was applied to the bottom electrode to switch the system into LRS. The general c-AFM setup placed a Pt-Ir coated silicon tip in direct contact with the surface of individual HfO_2 nanoribbons, creating a Pt-Ir/HfO_2 NCs/Pt test structure. The bias is applied to the bottom Pt electrode, with the current flowing through the ribbon vertically, which is then read via a grounded, conductive tip rastering along the top surface of the nanoribbon.

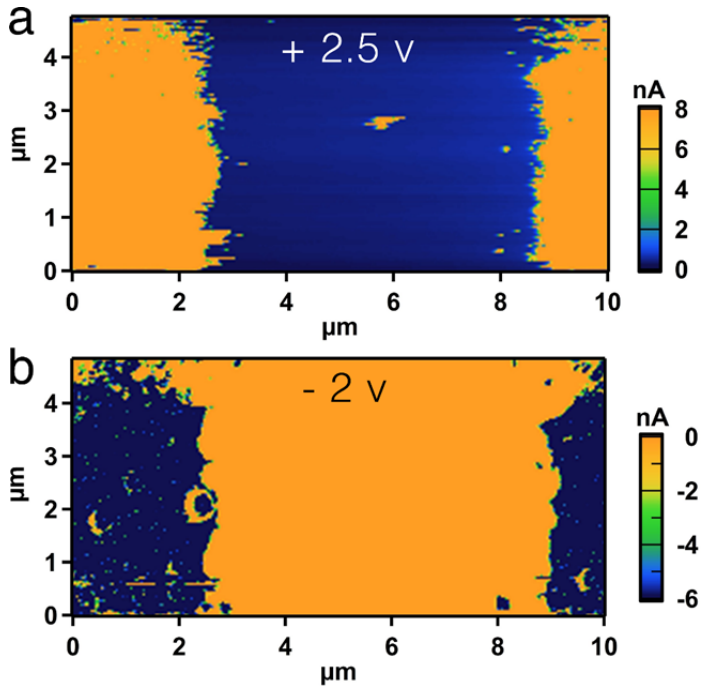

Figure 4.8. a, Current mapping of individual HfO_2-D ribbon with an applied voltage of +5.7 V, displaying a yellow conducting spot formed after a forming voltage of +6 V. b, Corresponding current mapping of the area with an applied voltage of -2 V. No observed conducting spot indicates the locally reset process occurred.

No current is measured across the nanoribbons before a forming process is induced under a large voltage applied to the middle of the ribbon. The large applied field creates and initiates the migration of oxygen vacancies, manifesting as a bright spot corresponding to a highly conductive region, as shown in Figure 2b on the HfO_2-U system. Current imaging was conducted by scanning the nanoribbon with an applied voltage of +5.7 V (Figure 4.8a), suggesting the conducting path formed locally during

forming/SET process and its nonvolatile property. The LRS is then recovered in the followed scan with -2 V applied bias (Figure 4.8b).

4.4 Resistive Switching and Transport Mechanism Between Nanocrystals

The electrical examination was employed by conductive AFM (c-AFM) with the tip placed in direct contact with individual nanoribbons, acting as a removable top electrode. Conductive AFM represents a powerful tool in the study of resistive switching especially for tedious manipulation of nanocrystals displays a typical current-voltage (I-V) response of an individual STONC nanoribbon, as collected using a sweeping Figure 4.9b.

The ("1-2-3-4") set-reset hysteresis observed in Figure 4.9b represents an "eight-wise" (counterclockwise) resistive switching response (opposite to the polarity based on biasing the TE).[5] [21] [24] [66] [75] [102] This result contrasts the "counter-eightwise" (clockwise) response observed in 10 nm thick epitaxial intrinsic STO thin films.[103] Though the nanoribbon height is approximately equivalent to the thickness of the epitaxial film previously reported, the primary difference is the apparent reduction in dislocation density[104] [105] within the individual STONC component nanocrystals. Extended defects such as dislocations typically enable the migration of oxygen vacancies via the filamentary conduction mechanism that dictates "counter-eightwise" switching within single crystalline STO.[4] [5] [21] [24] [66] [75] [102] [104] [106] [107] [108]

Figure 4.9c and d illustrate the possible mechanisms driving these phenomena, which closely resemble those recently determined for tip-induced resistive switching of individual TiO_2 nanocrystals.[78] In that study sandwich test structures comprised individual TiO_2 nanoparticles sandwiched between a Pt/Ir tip electrode and a Pt/Ir planar bottom substrate electrode. They subsequently applied a negative bias formed

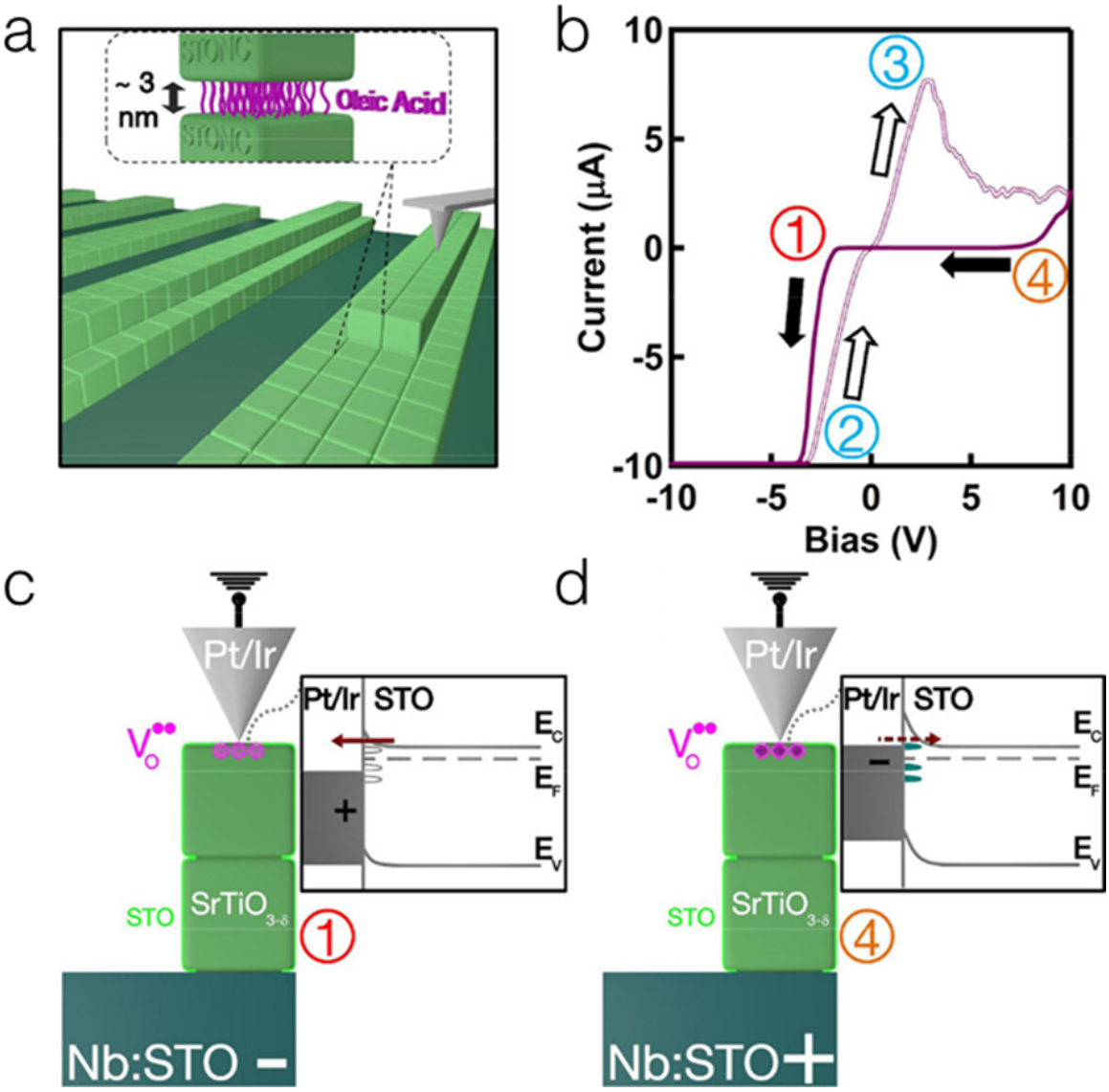

Figure 4.9. a, An illustration of the c-AFM measurement setup. The conductive AFM probe was acting as the movable top electrode, allowing current passes through the thickness direction. b, I-V response of individual nanoribbon displaying "eight-wise" resistive switching behavior, as indicated by the arrow markers. An illustration of the operating switching mechanism and the band structure across the multi-cube Pt/STONC interface. c, Applying a negative voltage injects electrons from the trap sites (oxygen vacancies or ligands; magenta spheres) to the top (tip) electrode, resulting in unfilled traps that narrow the Schottky-barrier and induces the HRS → LRS transition (a, ①). d, A positive applied voltage fills the interfacial traps with electrons (black dots in magenta spheres) and recovers the Schottky-like barrier, yielding a LRS → HRS transition (a, ④).

a depletion region at the bottom electrode as vacancies migrated towards the top electrode (tip), resulting in a LRS to HRS transition. Here we ruled out possible Schottky-like barrier modulation effects via oxygen vacancy migration due to the opposite polarity dependence observed, the down-scaling of the particle size and the resulting reduction in vacancy conducting pathways that typically occur along extended defects (dislocations, interfaces) of single crystalline STO. In this study the moveable top Pt/Ir tip electrode maintains ground while the bias is applied to the bottom NSTO electrode. Previous studies suggested a higher volume of oxygen vacancies concentrate along the extended defects due to increased reducibility compared to bulk.[108] In this study it is assumed that vacancies accumulate at the interfaces between individual STONC. Electronic absorption studies showed that the majority of defects populate the surface of the nanocrystal.[109] An oxygen deficient surface therefore creates a space-charge depletion region that effectively hinders oxygen diffusion.[75] [104] [105] This accordingly explains the observed lower current flow at low voltage region. For these reasons we assume the positively charged oxygen vacancies remain fixed at the Pt/Ir(tip)/STO interface and form a trap state for the following switch. The rectifying I-V response of HRS (Figure 4.9b; solid purple portion between points "①" and "④") results from the Schottky-like barrier formed along the (Pt/Ir)tip/STO interface. The initial bias sweep injects electrons into the STONC film and fills the trap sites at the tip-STONC interface. Applying a sufficiently large negative voltage to the bottom electrode releases the electrons, thus yielding unfilled traps and reduces the Schottky-like barrier width. This process enables electron tunneling, hence we observe a HRS→LRS transition (Figure 4.9c; "①"). Applying a large positive voltage to the bottom electrode refills the traps at the tip-STONC interface with electrons that neutralize the positive charge of the oxygen vacancies (Figure 4.9d; "④"). This process forms a strongly insulating interface and increases the barrier width, thus inducing the LRS→HRS transition. Note the extent that vacancy accu-

mulation/depletion occurs at the nanoribbon/Nb:STO interface must vary appreciably compared to heteroepitaxial STO/Nb:STO thin films. Recent studies of distorted STO/Nb:STO heterointerfaces observed rectifying behavior attributed to the modulation of interfacial vacancy depletion, where the electrode configuration used resulted in a symmetrical hysteresis, hallmark of two Schottky-junctions. The hysteretic response in Figure 4.9b is identical to those of Au/Nb:STO/Ag and s-In/NSTO/o-In nanostacks possessing asymmetric Schottky/Ohmic contacts. Therefore the local c-AFM I-V response of as-deposited STONC nanoribbons on NSTO are governed by conduction mechanisms at the tip-sample interface that enable tunneling via charge trapping/detrapping cycles defined by interfacial oxygen vacancy electron traps [5] [24] [67] [71] [110] [111] or Schottky barrier modulation.[15] [80] [112] [113] [114]

Figure 4.10 highlights the results of LRS/HRS switching endurance testing across STONC nanoribbons as collected locally by c-AFM. The semi-log I-V plot exhibits relatively robust endurance properties, as demonstrated by the overlap after 1 (red), 100 (purple), 500 (light blue), and 1000 (green) cycles, respectively. The FBD process likely results in incomplete deposition of STONC towards the ribbon edges in multilayer ribbons, yielding a possible thickness dependence. Local endurance tests were also performed at different tip positions along the nanoribbon from left-right at the locations marked by the red $\odot$, black ◭, and green $\otimes$ marks on the topographic image found in Figure 4.10a, respectively. Endurance profiles of LRS/HRS switching current collected at a read voltage of -1.5 V are shown in Figure 4.10c, where blue (square marker) lines indicate the LRS and red (diamond marker) lines indicate the HRS, respectively. The results shown in Figure 3c demonstrate robust and thickness-independent LRS/HRS values for the nanoribbons. The average R_{ON}/R_{OFF} ratio exceeds 10^3 over a span of 1000 switching cycles with no apparent position dependence. While the ratio does not quite approach the reported value (10^6) of UHV pulsed laser deposition-prepared 10-nm thick epitaxial thin films,[103] the value does

compare favorably with higher quality Pt-STO interfaces created by DC-Sputtering and e-beam evaporation (10^2 - 10^4),[80] or with sol-gel processed thin films with Pt electrodes (10^3).[115] Note that STONC nanoribbons display a more triangular than rectangular geometry, hence the stability displayed in the position-based endurance tests further confirms that a trap/detrap mechanism at the tip-(top)STONC interface defines transport, as no discernable thickness dependence is observed along either edge of the nanoribbon.

4.5 Nanoribbon Removal and Transfer

A key advantage of STONC nanoribbons produced by FBD is the ability to release the nanoribbons into a liquid for redeposition onto a second, arbitrary substrate or surface topology (Figure 4.11a). Previous studies successfully demonstrated this process for releasing CdSe stripes and grids into an aqueous solution.[98] [116] Figure 4.11b shows an optical micrograph of STONC nanoribbons floating on the water surface upon micrograph of STONC nanoribbons floating on the water surface upon removal by dissolution of a poly(acrylic)acid sacrificial layer, and of nanoribbons forming helical mesostructures when released away from the liquid-air interface (inset). In order to release the STO nanoribbons from the substrate, poly(acrylic) acid (PAA) is used as a sacrificial layer. An aqueous solution of PAA (20 mg/ml) is spun-coat (3000 rpm, 30s) on a pre-washed silicon wafer. Nanoribbons are released by dissolving the PAA sacrificial layer (height $\sim$ 50 nm) with water. Once the nanoribbons were released, transfer was completed by placing the second, arbitrary substrate in direct contact with the surface of the water meniscus. The STO helical shape of the released nanoribbons from the original structure (Figure 4.12a) can be found in Figure 4.12b and c. All commercial materials were used as received. The Ag and Pd electrode deposition (thickness = 100 nm) was performed by RF- and DC-sputtering of metal targets (Kurt Lesker; 99.99%) at room temperature and a base pressure

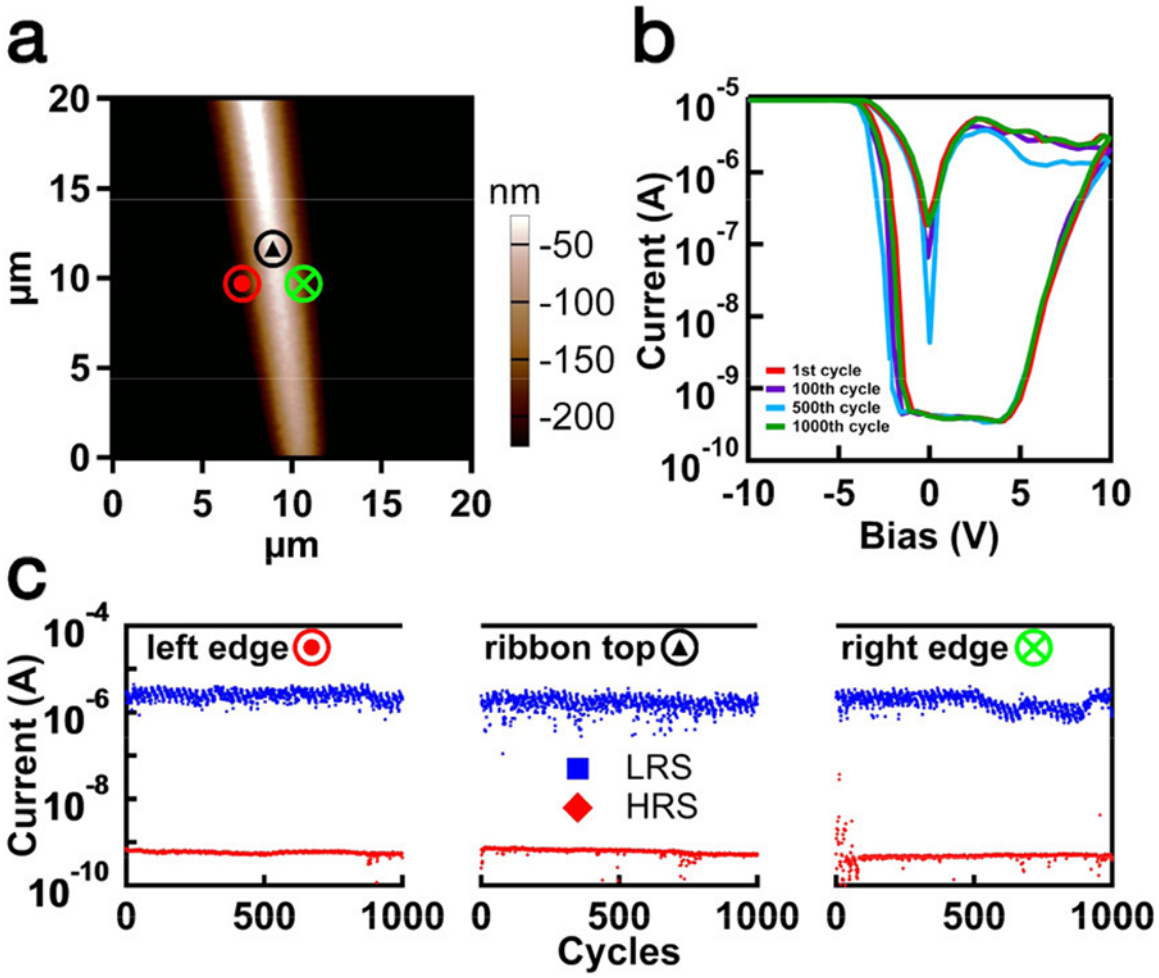

Figure 4.10. a, A topographic AFM image of an individual STONC nanoribbon (height = 400 nm). b, A semilog I-V plot of the STONC nanoribbon for the 1st (red), 100th (purple), 500th (light blue), and 1000th cycle (green). c, An endurance plot of log current vs number of cycles between the LRS (blue squares) and HRS (red diamond) measured locally over the left edge (a, red ⊙), top (a, black ▲), and right edge (a, green ⊗) at a read voltage of -1.5 V, respectively. The average R_{ON}/R_{OFF} ratio exceeds 10^3.

of 10^{-6} Torr. The metallized-PET films and substrates were rinsed with isopropyl alcohol and toluene and dried with a filtered stream of compressed air.

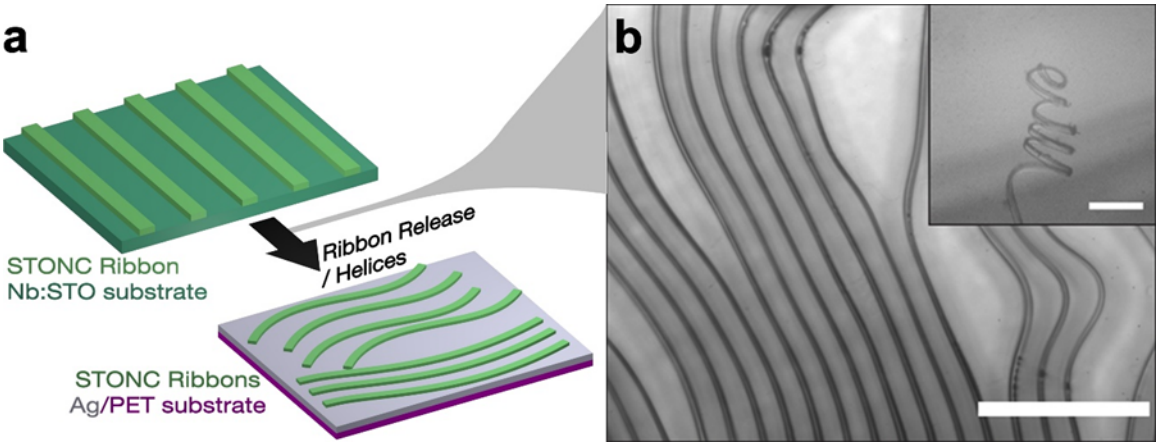

Figure 4.11. a. Illustration of the STONC nanoribbon to STONC nanohelix release/transfer cycle. After the FBD process samples are submersed in water, creating a suspension of STONC nanohelices that are redeposited onto arbitrary substrate (Ag-coated PET substrate, lavender-purple shown). b An optical micrograph of STONC nanohelices released into water from the Nb:STO substrate (scale bar: 500 μm). Inset: an optical micrograph of an individual STONC nanohelix displaying its flat-ribbon-like geometry (scale bar: 200 μm).

To demonstrate the versatile nature of the FBD-deposition process nanoribbons were removed from the original hard substrate and transferred onto a flexible PET substrate with Ag and Pd metal coating for examination via c-AFM. Virtually all studies involving resistive switching of thin films remain limited by the top-down lithographic processes to evaporate or sputter various top electrode materials on a fixed film/metal/substrate bottom electrode configuration. The FBD transfer process provides the unique advantage of selecting the bottom electrode material to induce or potentially enhance a desired transport mechanism within functional oxide nanostructures.

The I-V response of the STO/Ag/PET structure shown in Figure 4.13a exhibits switching characteristics opposite of the eightwise switching displayed by the same nanoribbons on the NSTO substrate in Figure 4.7a. The I-V response displays highly

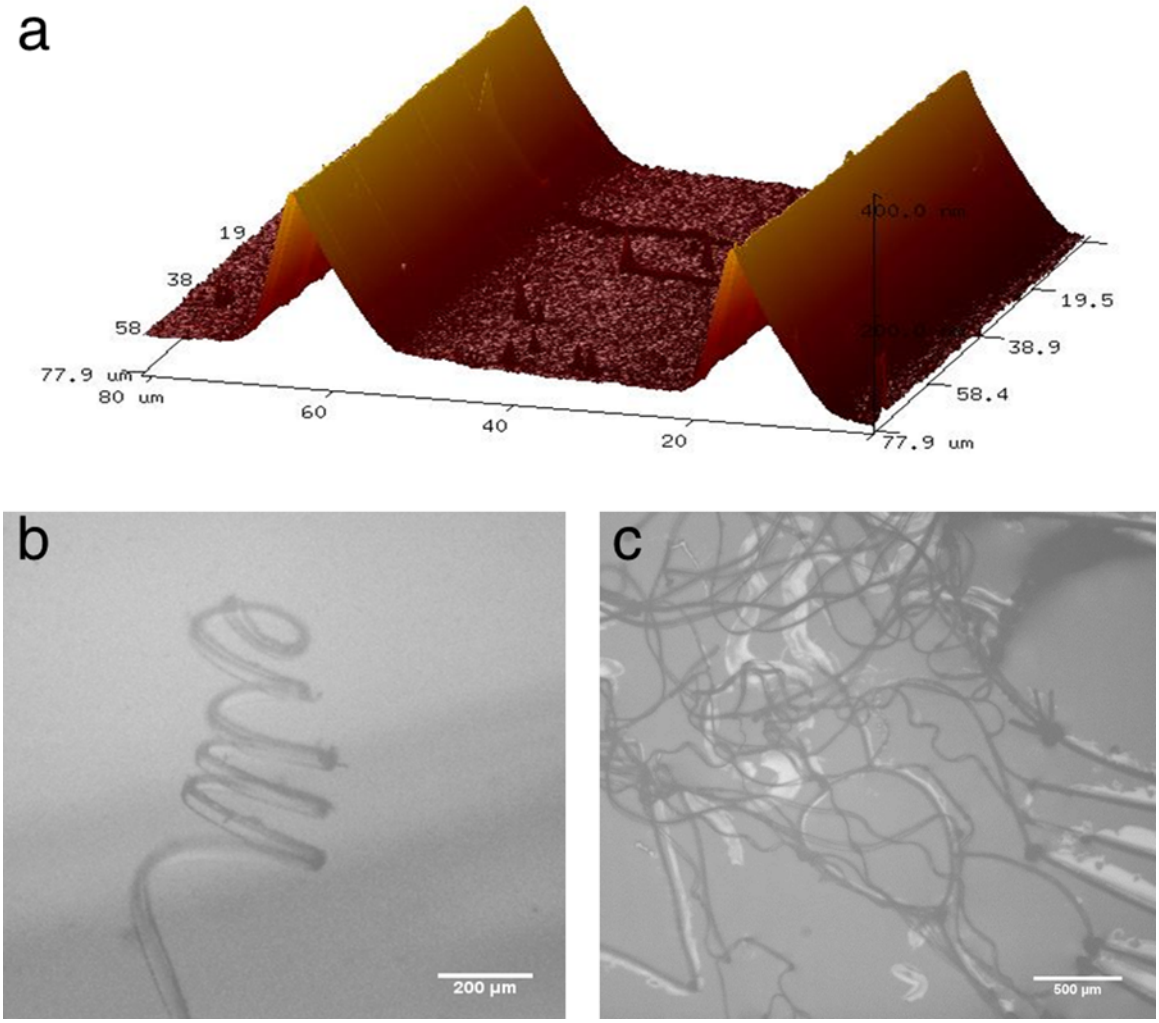

Figure 4.12. a, 3D AFM image of the STO nanoribbons deposited on the substrate by FBD approach. Optical image of b, STO helix and c, STO ribbons in water.

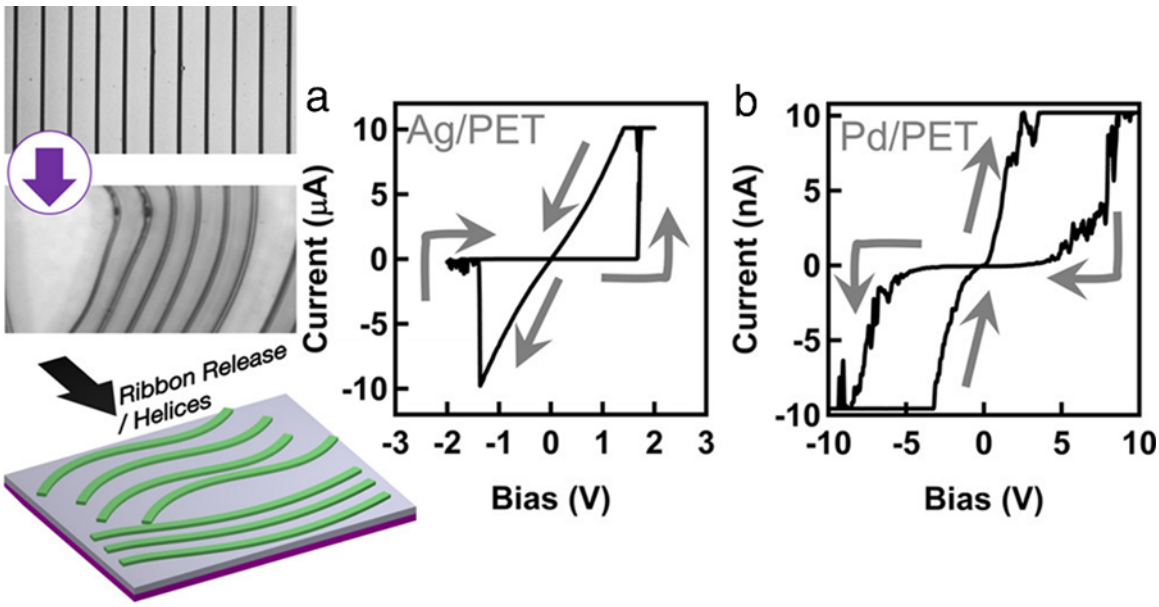

Figure 4.13. a, The I-V response of an individual STONC nanoribbon post-transfer on a Ag-metallized PET substrate. b, The I-V response of an individual STONC nanoribbon post-transfer on a Pd-metallized PET substrate, exhibiting "eightwise" switching character.

linear Ohmic behavior under the LRS and sharp, pronounced LRS↔HRS transitions, indicative of formation and dissolution processes of filament induced by cation migration with the chemical active electrode being Ag. This curve fitting of the log-log response confirmed the LRS exhibits Ohmic-character, with a slope of 1, which confirms the formation of metallic filaments (Figure 4.14a). Applying a positive bias to the Ag bottom electrode creates Ag cations that drift through the STO nanoribbons towards the top (tip) counter electrode, where they subsequently reduce to Ag atoms and form the highly conductive filaments responsible for the steep current increase. Conversely, an applied negative voltage induces Joule heating and oxidizes the Ag atoms at the counter electrode, which causes the conductive filament to rupture and starts the LRS→HRS transition. The slight variation in LRS current during endurance testing is attributed to the randomly branched growth of filaments near the inert Pt electrode.[117] Improving the endurance stability within transferred nanorib-

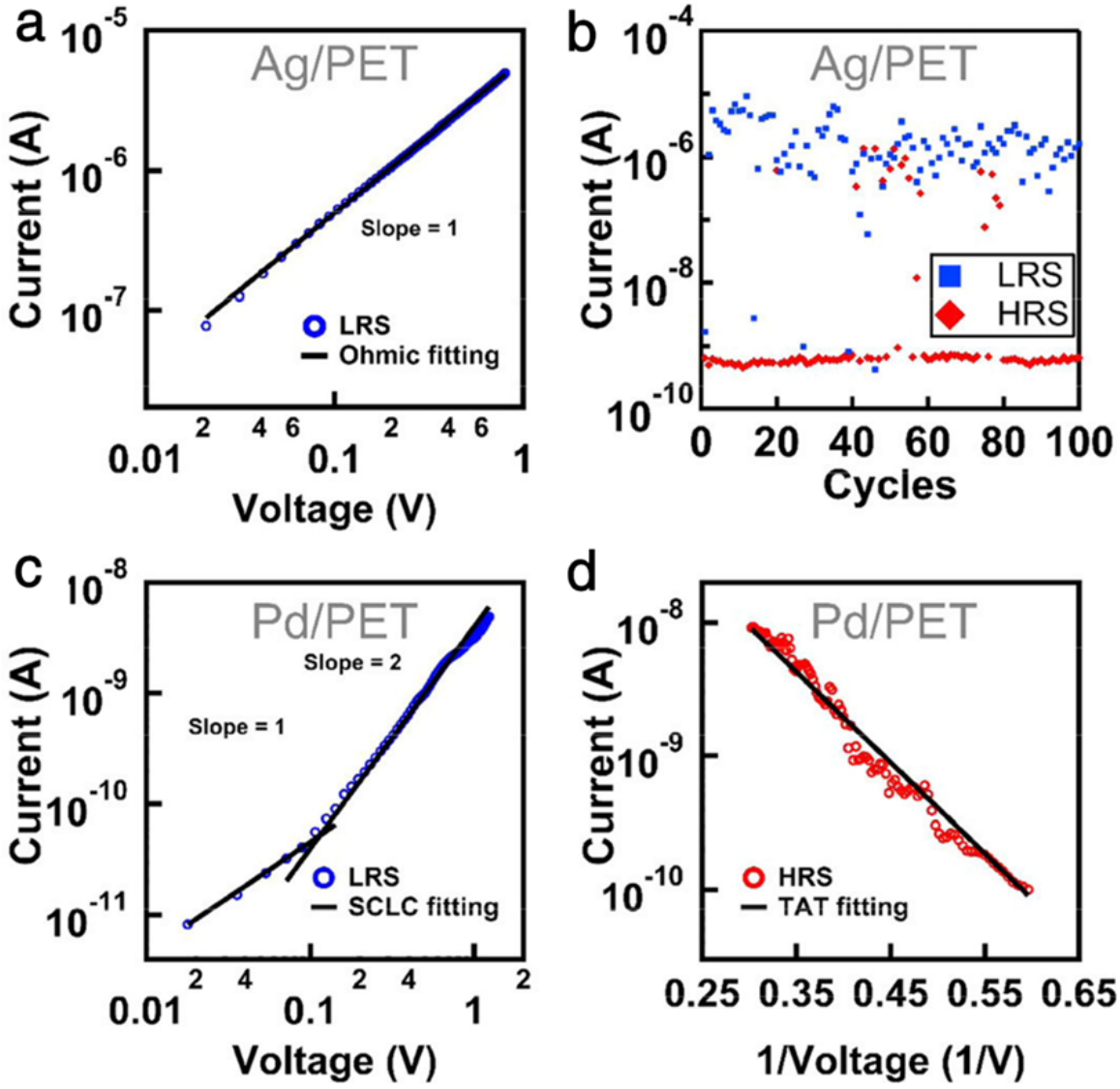

Figure 4.14. a, The STO/Ag/PET LRS branch on a log-log scale, which displays a linear slope of 1 corresponding to the Ohmic conduction model. b, The resistance plot of STO/Ag/PET under voltage sweeping for 100 cycles. c, The STO/Pd/PET LRS branch on a log-log scale, displaying a slope of 1 at low voltages and an increased slope ($\sim$ 2) at higher voltages, corresponding to the space charge limited current (SCLC) conduction model. d, The STO/Pd/PET HRS branch of the I-(1/V) response on a log-log scale, which exhibits a negative linear slope indicative of trap-assisted tunneling (TAT) conduction.

bons warrants further studies involving optimization of the release, redeposition, and secondary substrate/contact selection.

The I V curve (Figure 4.13a) shows a sudden increase of the current level when reaches a threshold voltage, corresponding to the typical electrochemical metallization memory (ECM) which consists of an electrochemically active electrode metal, i.e. Ag and Cu. Here the switching mechanism is attributed to the redox and migration of Ag ions, which possess higher mobility than oxygen vacancies.[4] As a positive voltage is applied to the Ag electrode, oxidation occurs, of the form:

$$Ag - \ e^{-} \xrightarrow{\text{Oxidation}} Ag^{+} \tag{4.1}$$

The cations in the STO nanoribbons drift towards the counter electrode under the electric field and reduces there accords the reaction:

$$Ag^{+} \xrightarrow{\text{Reduction}} Ag + \ e^{-} \tag{4.2}$$

leading to the formation of highly conductive filaments responsible for the steep increase of the slope. Conversely, an applied negative voltage dissolves Ag atom from the counter electrode driven by the Joule heating. This causing the conducting filament to rupture, and switching back to the HRS. Moreover, the transferred nanoribbons possessed an increased R_{ON}/R_{OFF} ratio (10^4) and a reasonable endurance lifetime of $\sim$ 100 cycles. The slight variation in LRS current during endurance testing is attributed to the randomly branched growth of filaments near the inert Pt/Ir electrode.[48] Improving the endurance stability within transferred nanoribbons warrants further studies involving optimization of the release, redeposition, and secondary substrate/contact selection.

STONC nanoribbons were also transferred onto Pd-metalized flexible PET substrates to create a Pt/Ir/STO/Pd/PET test structure, which displayed entirely dif-

ferent switching characteristics, as observed in Figure 4.13b. In this case, the nanoribbons possessed counter-eightwise switching character but showed no rectifying behavior at the HRS. This is due to the relative symmetry of the sample structure. Figure 4.14c shows the LRS response in a log-log scale, exhibiting an increasing slope from 1 (I $\propto$ V) to 2 ($I \propto V^2$) with increasing applied voltage, thus suggesting transport based on the space charge limited current model (SCLC). The HRS response (Figure 4.14d) displays a linear response that trends with $\ln I \propto \frac{1}{V}$, fitting the trap-assisted tunneling model (TAT)[118] and emphasizing the critical role that traps play during switching at the Ir-tip/STO interface. To induce an HRS→LRS transition, an applied negative voltage to the Pd bottom electrode injects electrons into the STONC ribbons, which are then captured by the trap sites along the Ir-tip/STO interface and subsequently emitted to the tip. This two-step tunneling process is likely assisted by oxygen vacancies and the oleic acid ligands between nanocubes.

4.6 Local c-AFM of Pt tip/STO-(Pd/PET)substrate Under Bending

We also explored the effect of the resistive switching behavior of nanoribbons under bending force, the c-AFM I-V response of transferred STONC nanoribbons on flexible, Pd-metallized PET substrates were also collected under a fixed curvature, as shown in the inset of Figure 4.15. STO/Pd/PET assemblies were affixed to a stainless steel nail shaft, inducing a strain of ∼3%. The stability exhibited by the nanoribbons in a bending state demonstrates enormous promise as a candidate for flexible electronic device platforms where electrical and mechanical reliability still present significant challenges. The strain value of the bent STO/Pd/PET structure is approximated as:

$$\varepsilon(\%) = \frac{t}{D}, \tag{4.3}$$

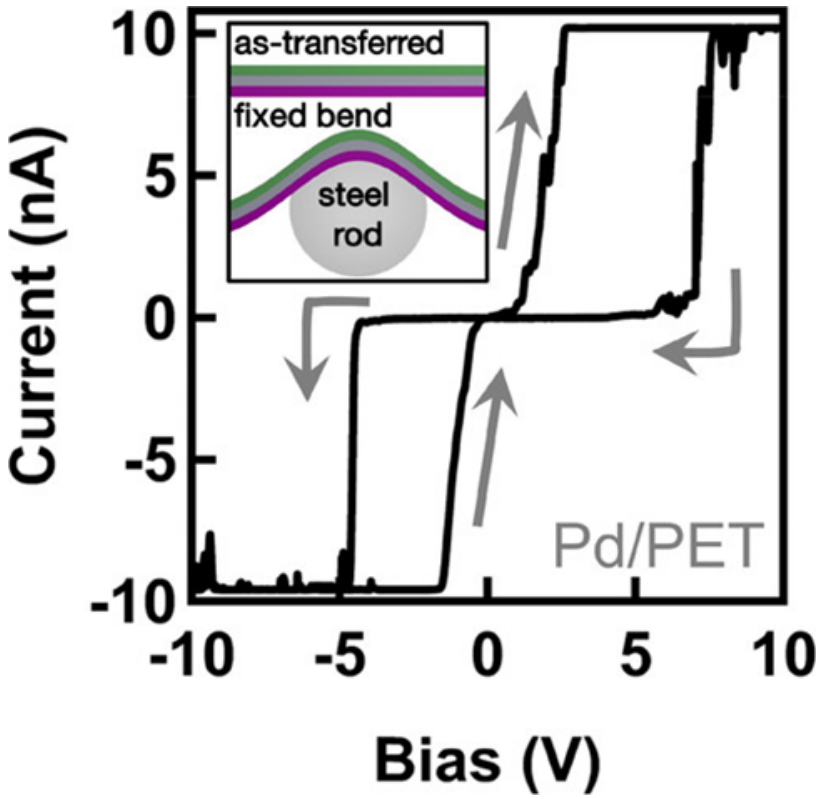

Figure 4.15. a, The I-V response of an individual STONC nanoribbon on a Pd/PET substrate under strain. (inset) The as-transferred nanoribbons are affixed to a steel rod of known diameter, inducing a substrate strain of ∼3%.

where ε is the strain in percentage, t is the thickness of the PET substrate and D is the diameter of the bending radian, in this case a stainless-steel nail shaft.

Figure 4.16 shows the fitting results of the LRS response using the space charge limited current model (SCLC; Figure 4.16a) and of the HRS response using the trap-assisted tunneling model (TAT; Figure 4.16b), which emphasizes the important role that traps play during switching at the Pt/STO interface. These curve fitting of the I-V response in confirmed the nanoribbons retained both the SCLC-based LRS and TAT-based HRS character displayed by the as-transferred STO ribbons on the Pd/PET substrate. To induce an HRS→LRS transition, an applied negative voltage on the Pd bottom electrode injects electrons into the nanocubes, which are then captured by the trap sites along the Pt/STO interface and subsequently emitted to the tip. This two-step tunneling process is likely assisted by oxygen vacancies and the oleic acid ligands between nanocubes. The following equation represents the TAT mechanism:

$$J_{TAT} = A \exp(\frac{-8\pi\sqrt{2qm^*}}{3hE}\phi_T^{\frac{3}{2}}) \tag{4.4}$$

where ϕ_T is the energy of the electron traps with respect to the conduction band edge of the oxide.

4.7 Thickness Dependency of Memristive Nanoribbons

As shown in Figure 4.6e, an individual nanoribbon presents varying thickness along the cross-sectional profile. Figure 4.17 shows part of topography of the ribbon and indicates the increasing height start from left. To study how the thickness affects the switching behavior, three different spots have been chosen with the same space as marked in the topography. The thickness can be approximated as 30 nm, 90 nm and [119] nm, respectively. The first sweeping (-10V - +10V) and a typical switching I-V

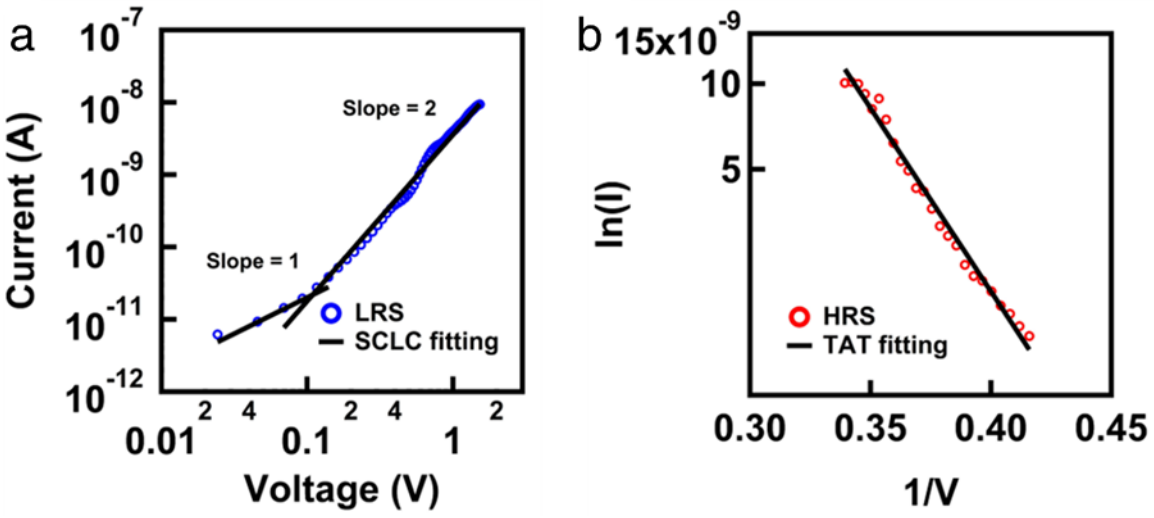

Figure 4.16. Curve fitting of a typical switching cycle of STO/Pd/PET after bending for a, LRS and b, HRS, respectively.

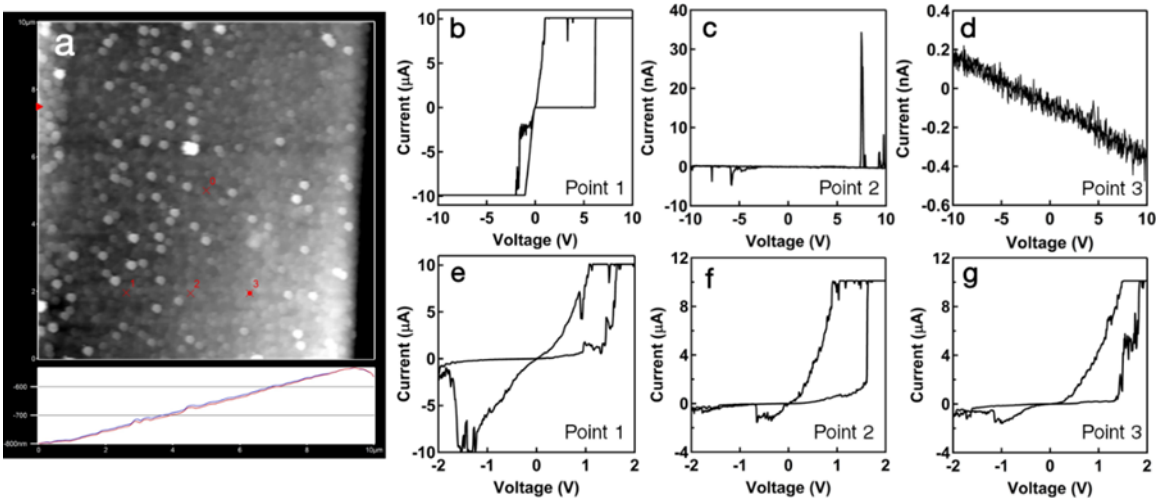

Figure 4.17. Thickness dependent measurement of HfO_2-U. a, 10 μm $\times$ 10μm AFM topography of HfO_2-U sample. The red makers indicate the three different points with increasing height that picked for the measurement. b-d, the I-V characteristic of the first voltage sweeping ($\pm$10V) collected at point1, 2 and 3 respectively. e-g, the corresponding I-V responses after the electroforming process at different positions. All of them represent BRS behavior and show similar operating voltage.

response (-2V - +2V) at each point were illustrated in Figure 4.17 b-g. Point 1 was switched to LRS at around +6 V and the resistive switching behavior can be observed after the first cycle. For larger thickness, however, the first cycle was not sufficient to initiate the switching character so that extra voltage sweeping was required. After forming, the I-V curves are similar including the SET and RESET voltages.

4.8 Effect of Ligands on Memristive Behavior

4.8.1 The Conduction Mechanism After Removing Ligands

For STO nanoribbons transferred onto a Pd-metalized, silicon substrate, the sample was annealed at 500°C for 2 min under ambient conditions to remove the all the ligands. The fitting results are presented in Figure 4.18c, d. The LRS character remains identical for the flexible Pd/PET substrate and the hard Pd/Si substrate, as both follow a linear relation at low voltages and a quadratic behavior at higher voltages. However, the HRS character in the Pd/Si case deviates significantly from the TAT model, as shown in Figure 4.18, which suggests a reduced trap-assisted effect. As the annealing step removed the presence of ligands, the change in conductive mechanism here confirms that the ligands play a critical role as traps for assisting electron tunneling.[120] Note that the ligands can effectively reduce the current level up to two orders of magnitude, thus demonstrating the potential role of ligands in reducing power consumption. Instead the HRS displays the character of Fowler-Nordheim tunneling (F-N), which follows the model:

$$J_{FN} = \frac{q^2}{8\pi h\phi_B} E^2 \exp\left(\frac{-8\pi\sqrt{2qm^*}}{3hE}\phi_B^{\frac{3}{2}}\right) \tag{4.5}$$

where ϕ_B is the barrier height, m^* is the electron effective mass and h is the Planck's constant.

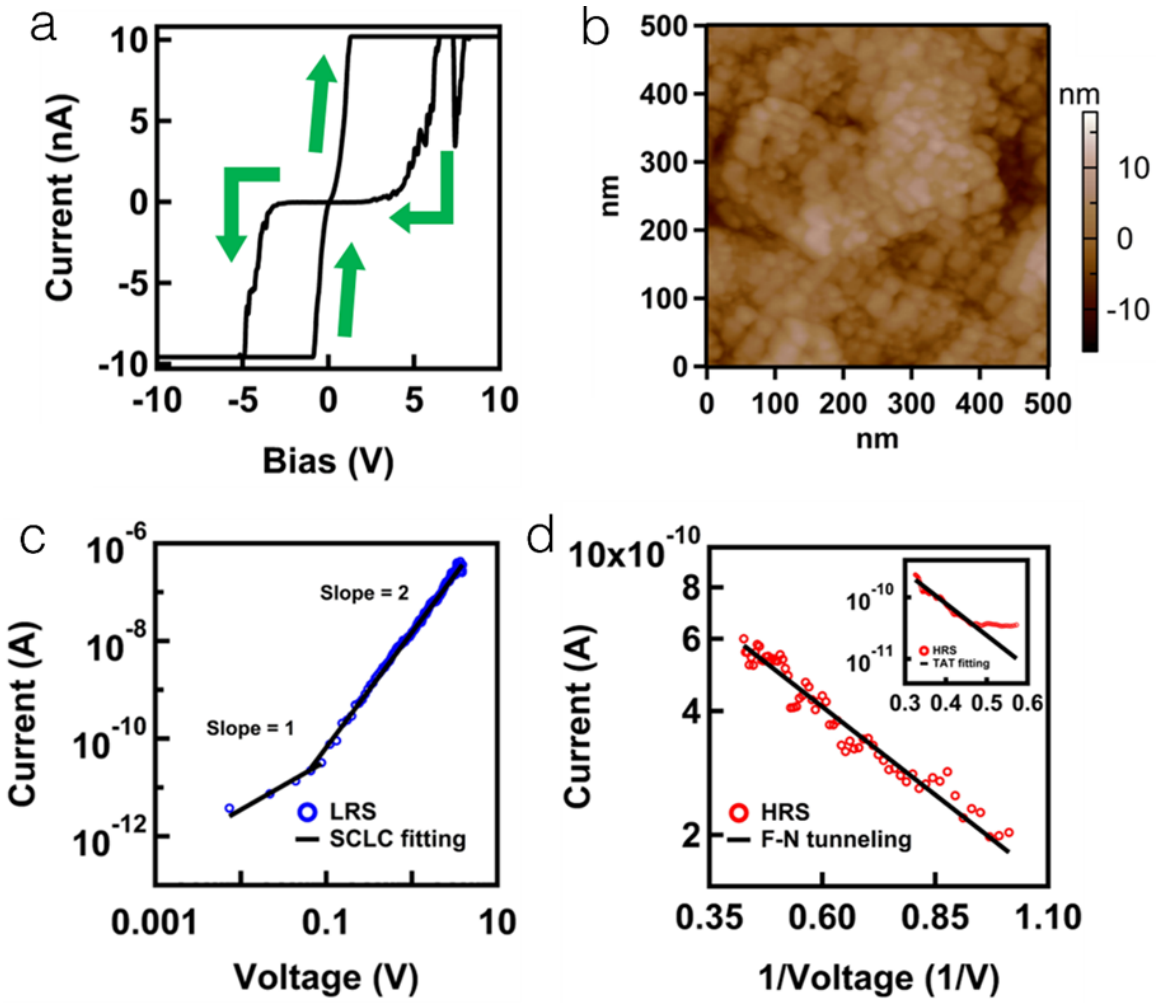

Figure 4.18. a, Representative I-V curve of the STO/Pd/Si structure. b, AFM topography of transferred STO nanoribbon on Pd/Si substrate after annealing at 500°C for 2 min. c, d The curve fitting of the I-V characteristic of STO/Pd/Si structure for LRS and HRS, respectively. The HRS follows the F-N tunneling model while the LRS follows the SCLC model, which shows different mechanism from the STO/Pd/PET structure. Inset shows the deviation of the HRS from the TAT model.

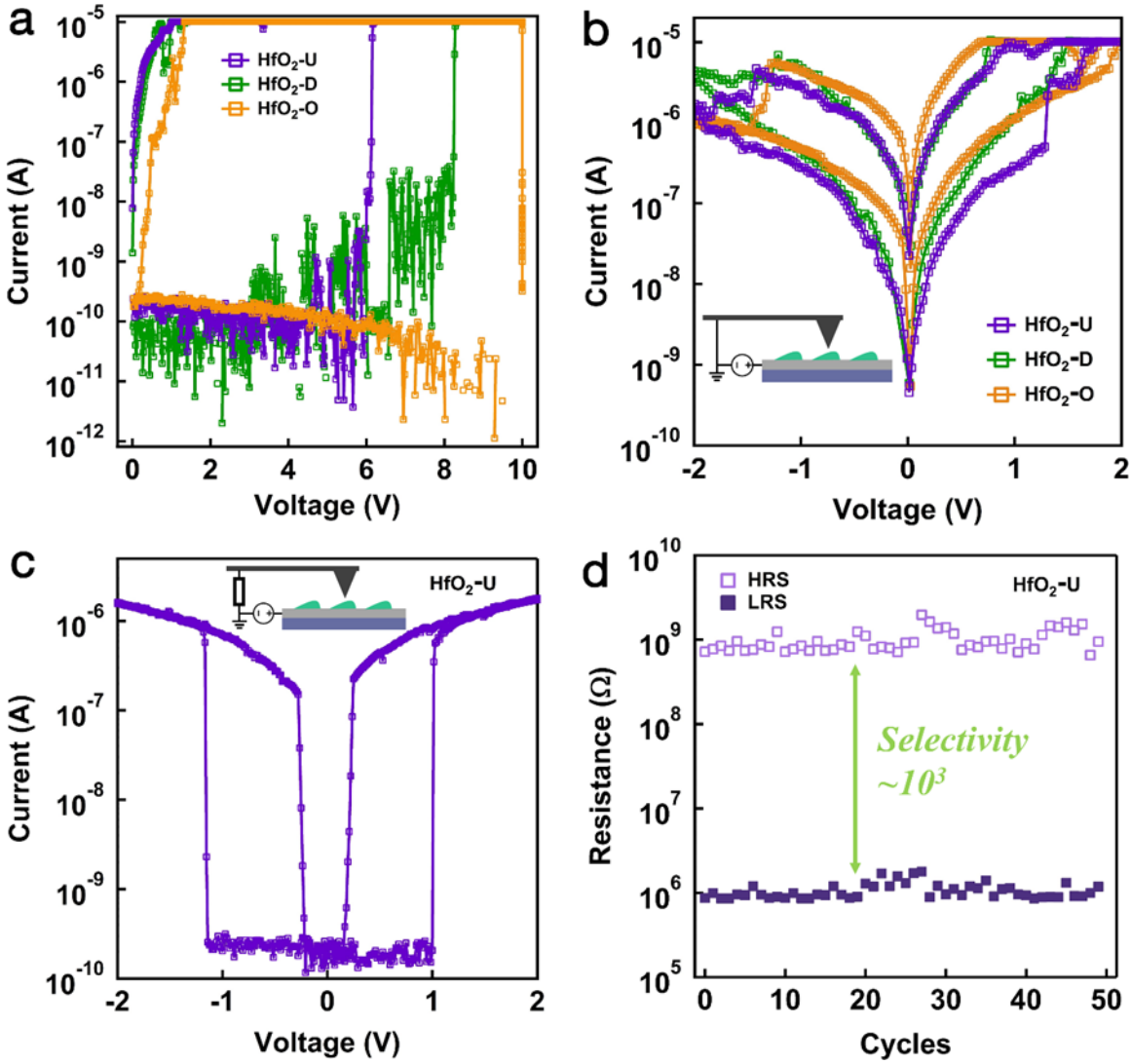

Figure 4.19. a, I-V curves for the forming process of HfO_2-U, HfO_2-D and HfO_2-O, respectively. b, Representative I-V response of BRS for three samples. c, I-V curve of the TS behavior of HfO_2-U sample. d, 50 cycles endurance of TS by sweeping at a read voltage of 0.5 V, showing a selectivity of 10^3 between the HRS (light purple; open symbols) and LRS (dark purple; closed symbols).

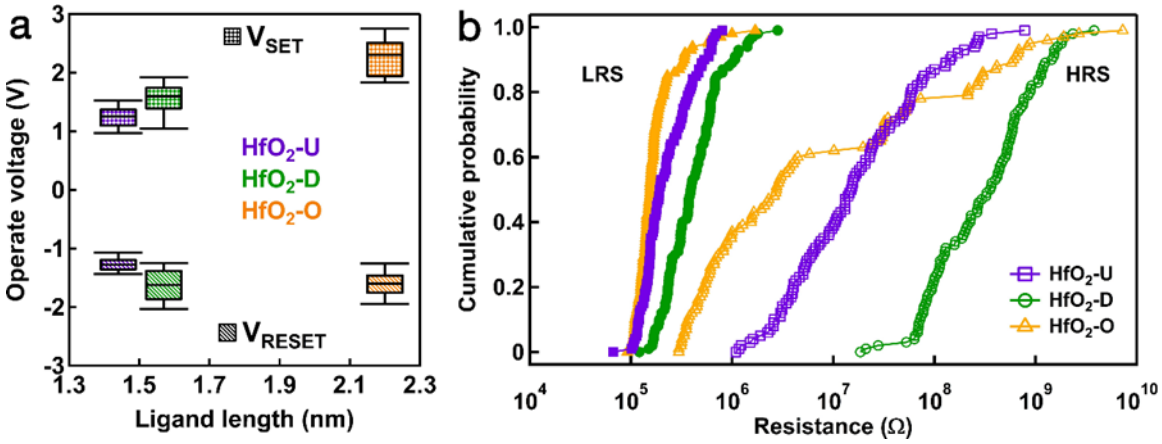

Figure 4.20. a. The statistical distribution plot of switching voltages as a function of ligand length. Both V_{SET} and its distribution scale with increasing ligand length. b, The cumulative probability for the LRS (filled symbols) and HRS (open symbols) of HfO_2-U (purple; square), HfO_2-D (greengreen; circle), and HfO_2-O (orange; triangle), respectively

4.8.2 How Ligand Length Affects Memristive Behavior

Nanoribbons comprising HfO_2 NCs capped with three types of ligands; oleic acid, dodecanoic acid, and undecenoic acid, labeled hereafter as HfO_2-O, HfO_2-D and HfO_2-U, were deposited onto silicon substrate coated with 5 nm Ti/30 nm Pt as the bottom electrode. The electroforming process induced filament formation within HfO_2 nanoribbons capped with the three ligand systems is shown in Figure 4.19a, where the HfO_2-U, HfO_2-D and HfO_2-O systems displayed forming voltages of 6.1 V, 8.2 V and 10 V, respectively. As 10 V represents the limit of the internal bias source of the AFM, electroforming HfO_2-O required applying the bias of 10 V for longer time periods (between 30 - 60 sec). Figure 4.19b shows the semi-log I-V response of the three ligand capped HfO_2 nanoribbons. They all display typical bipolar switching character, where the SET and RESET process occur under positive and negative voltage, respectively, and exhibit a variation in operating voltage, current level and the resistance ratio between them. A standard 1 MΩ resistor was used to transition between operative bipolar resistive switching and threshold switching modes in the

nanoribbons. The current-voltage (I-V) character observed in Figure 4.19c represents the threshold behavior under voltage sweeping (± 2 V, 1 Hz) when the resistor is connected in series with the HfO_2-U system. Unlike the bipolar switching, the threshold switching shows a symmetric I-V curve. Moreover, it shows a high resistance (10^9 Ω) initially followed by an abrupt increase in current level upon reaching a threshold voltage of approximately +1 V. The ribbon maintains LRS and recovers to the HRS suddenly at a hold voltage of +0.25 V. This threshold behavior can be tuned with the external resistor for each sample, exhibiting similar operating voltage ranges and stability. Figure 4.19d shows 50 switching cycles within a single HfO_2-U nanoribbon, suggesting the TS behavior remains stable, with a selectivity of 10^3. When the resistor is removed, the typical bipolar resistive switching hysteresis is observed.

To evaluate the effect of ligand length on memristive behavior, we estimated the interparticle spacing of the three samples based on the carbon-carbon covalent chain length: HfO_2-U (1.44 nm), HfO_2-D (1.57 nm), HfO_2-O (2.2 nm). Figure 4.20a plots the SET and RESET voltage distribution for bipolar switching as a function of the ligand length. The SET voltage clearly scales with increasing ligand length, while the RESET voltage exhibits a smaller dependence on length. An increase in the V_{SET} distribution can also be observed in the statistical plot with the increased ligand length, while for V_{RESET}, however, no clear correlation is found. Figure 4.20b presents the cumulative distribution function of the LRS and HRS of the three ligand types. The results were collected using DC sweeping mode at a read voltage of 0.5 V. The resistance in LRS exhibits a much smaller variation compared to the large variations observed for HRS for all three types. The HfO_2-O system shows a large HRS fluctuation range of about 10^4 while the HfO_2-U and HfO_2-D systems show improved uniformity of about 10^3 and 10^2, respectively.

Previous studies of PbSe NCs showed that the carrier mobility depends on nanoparticle size and the ligand length, the latter of which determines the interparticle tun-

nel distance.[85] As the same nanoparticle size was used for all samples, the observed difference in RS behavior is therefore attributed to the variation in the ligand length. The charge transport mechanism involves sequential electron hopping through nanoparticles, as described by a tunneling model where the mobility strongly depends on the interparticle distance.[86]

Here both the forming (Figure 4.19a) and the subsequent SET process (Figure 4.20a) display a ligand length dependence, as both V_F and V_{SET} increase with increasing ligand length. During the charge transfer process the ligand facilitates electron tunneling by effectively serving as an insulating spacer.[121] Using the c-AFM tip as the top electrode forms a Pt-Ir tip-HfO_2 NCs-bridge-metal structure, where the term bridge indicates the capping ligand separating neighboring NCs and the metal bottom electrode with the bulk HfO_2 NCs. When a positive voltage is applied to the bottom electrode during the electroforming process, the high electric field enables the creation of oxygen vacancies within the NCs and induces migration toward the tip along the grain boundary to form a low resistance conductive path.[8] The electrons injected from the tip under the negative voltage thus pass through the conductive channel and tunnel between NPs, inducing a transition from HRS to LRS. When a negative voltage is applied to the bottom electrode, the oxygen vacancies migrate towards the counter electrode as driven by the electric field of opposite sign, thus severing the conductive channel.

When a negative voltage is applied to the bottom electrode, the oxygen vacancies migrate towards the counter electrode as driven by the electric field of opposite sign, thus severing the conductive channel. The mechanism driving the formation and rupture of conducting filaments in HfO_2-based RRAM is typically attributed to oxygen vacancy migration.[8] [97] [122] [123] For the inorganic:organic capping ligand system presented here we cannot fully exclude the possibility of more complicated switching mechanisms involving ligand-mediated vacancy transport, however as the

ligands comprise long hydrocarbon backbones and possess limited available oxygen sites compared to the oxide nanoparticles, this process is highly unlikely to occur.

The coexistence of tunable TS and BRS character within HfO_2 and NiO thin films [99] [123] [124] [125] has been attributed to current-controlled morphology changes of the dominant conductive filament. Joule heating also contributes to thermally-assisted processes and thus facilitates the formation and rupture of the conducting path.[124] Limiting the current flow with an external resistor significantly reduces the current and subsequently induces an instability within the filament, ultimately resulting in filament rupture after the applied voltage is removed. Conversely, the current increases when the external resistor is removed such that a stronger filament is formed by continuous growth, thus producing an active conducting path even after the removal of external voltage.

The significant ligand length dependent RS behavior is observed in both electro-forming and subsequent switching processes. In general, variations in V_{RESET} (Fig. 4.20a) and the LRS (Fig. 4.20b) result from either changes in the filament diameter or the number of conducting filaments formed during the SET process, while variations in V_{SET} (Fig. 4.20a) and the HRS (Fig. 4.20b) highly depend on variations in the tunneling gap.[97] HfO_2-O nanoribbons exhibit a larger distribution in V_{SET} and HRS compared to the other two ligand systems, suggesting that the large variation in the reset process occurs due to the longer ligand length of oleic acid. Also, HfO_2-U possesses a lower HRS resistance compared to HfO_2-D since it possesses the shortest ligand length for electron tunneling at HRS.

4.9 HfO_2 Nanoparticles Crossbar Devices

To demonstrate a solution-processed memristive platform, a crossbar device was fabricated with a flow-coated HfO_2-U thin film sandwiched between Ti top and Pt bottom electrode. The schematic of the cross-point HfO_2-U test structure is shown

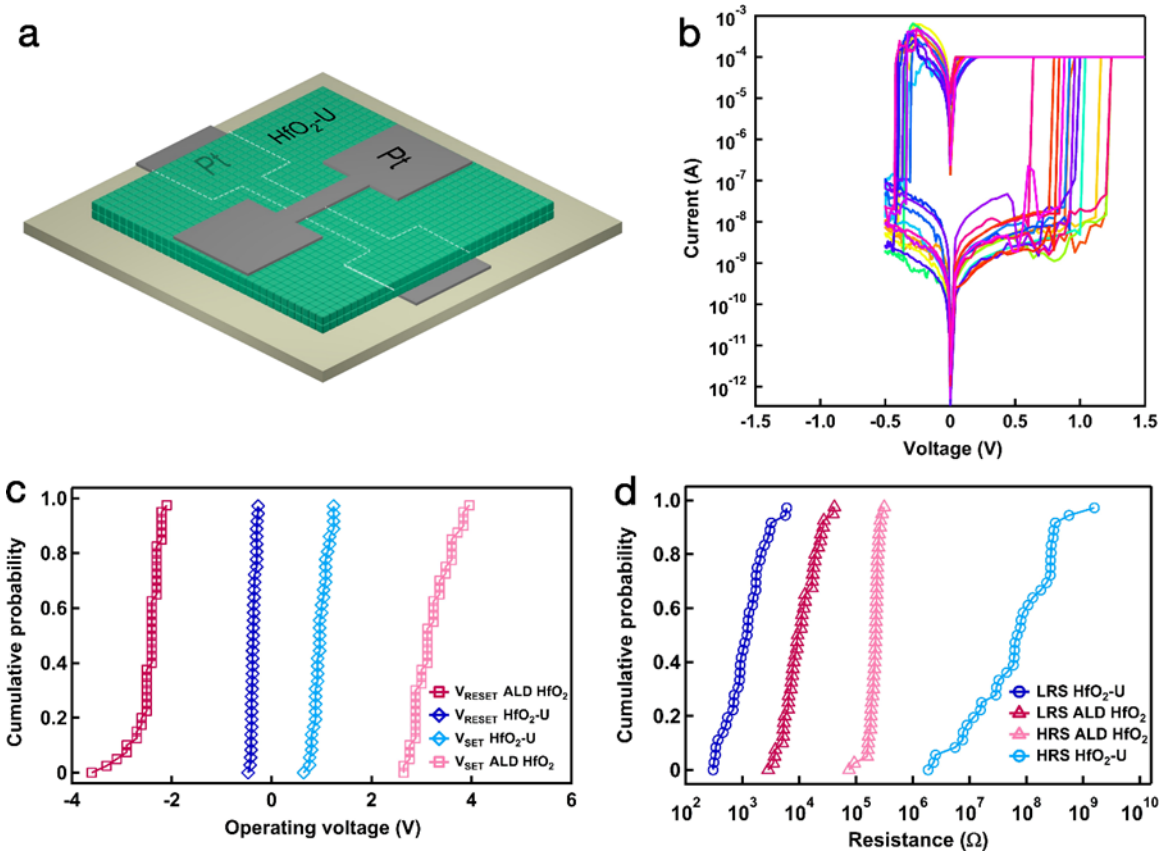

Figure 4.21. a, Schematic of a single Pt/HfO_2-U/Pt ReRAM device. b, The representative I-V characteristics of Pt/HfO_2-U/Pt ReRAM device. c, Comparative statistic cumulative probability of the operating voltage for HfO_2-U and ALD-prepared HfO_2. d, The cumulative probability of the resistances in each state of HfO_2-U and ALD-prepared HfO_2.

in Figure 4.21a. Using the same solution concentration, the width of the ribbon is simply extended by varying the stopping distance and substrate velocity. Using the longer stopping distance, we fabricated a 5x5 μm^2 crossbar type device comprising a 40 nm thick HfO_2-U thin film sandwiched between 30 nm thick Pt electrodes. The bipolar resistive switching I-V response was measured by sweeping a DC voltage from -0.5 V to +1.5 V after a forming process using a compliance current of 100 μA (Figure 4.21b). An ALD-deposited 10 nm HfO_2 RRAM device with the same area was fabricated for comparison. Here the solution-processed HfO_2-U device clearly exhibits smaller operating voltages, narrow distribution/increased uniformity, and larger ON/OFF ratio as shown in Figure 4.21c, d. The average SET and RESET voltages were 0.97 V and -0.36 V, respectively for HfO_2-U; the ALD-deposited HfO_2 displayed values of 3.2 V and -5.7 V, respectively. The ON/OFF ratio improved from 10 for ALD HfO_2 to 10^5 for the HfO_2-U at the expense of a small decrease in the uniformity of the resistance. Thus, the solution-processed device exhibits both stable switching behavior and small operating voltages that are competitive with more commonly employed ALD-deposited HfO_2 thin film-based devices.

4.10 Summary of Chapter 4

Top-down, ultrahigh vacuum (UVH) deposition approaches for MIM nanostructures yield highly crystalline, heteroepitaxial interfaces, but limit the number of electrode configurations due to a fixed bottom electrode. Therefore a facile, inexpensive, scalable fabrication method was introduced that yields memristive nanoribbon structures comprising solution-processed, single-crystalline complex oxide nanoparticles possessing complete transferability to arbitrary substrates. As-fabricated $SrTiO_3$ nanoribbons displayed stable eightwise switching, in contrast to the counter-eightwise polarity exhibited by single crystal STO thin films with appreciable dislocation densities. The endurance of memristive behavior was also demonstrated, including switch-

ing ratios up to 10^4, after nanoribbon redeposition onto polyethylene terephthalate (PET) flexible substrates. The combination of ambient, aerobic prepared nanocrystals and convective self-assembly deposition herein provides a pathway for facile, scalable manufacturing of high quality, functional oxide nanostructures on arbitrary surfaces and topologies. The ability to transfer nanoribbons to arbitrary substrates creates a rich parameter space by which any desired polarity response, improved R_{ON}/R_{OFF} ratio, and switching type is potentially tailored through bottom electrode metallization selection (or change). The transferability and durability of memristive properties post-transfer or in a strained state boast promise as flexible and printed electronic elements.

Subsequently the ligand length was shown to directly affect the resistive switching behavior through the comparison of three commonly employed ligand chemistries. Our c-AFM results showed that individual HfO_2 nanoribbons demonstrated both threshold switching and bipolar resistive switching modes, dependent upon an external resistance applied to the system, which limits current and further changes the filament morphology. Oxygen vacancies formed during hydrothermal process and under high applied voltage drive the switching behavior, while the operating parameters and stability correlate directly with ligand length. Finally, a solution-based device displays promising advantages, including low cost, lower operating voltages, increased uniformity, and larger ON/OFF ratio compared to the typical ALD thin film HfO_2 memory device. The chosen ligands for this study are frequently used for nanoparticle stabilization, and thus should immediately apply to optimizing resistive switching behavior in other solution-processed, complex oxide nanoparticle systems.

CHAPTER 5

ENHANCED CYCLE-TO-CYCLE UNIFORMITY

5.1 Cycle-to-Cycle Variability

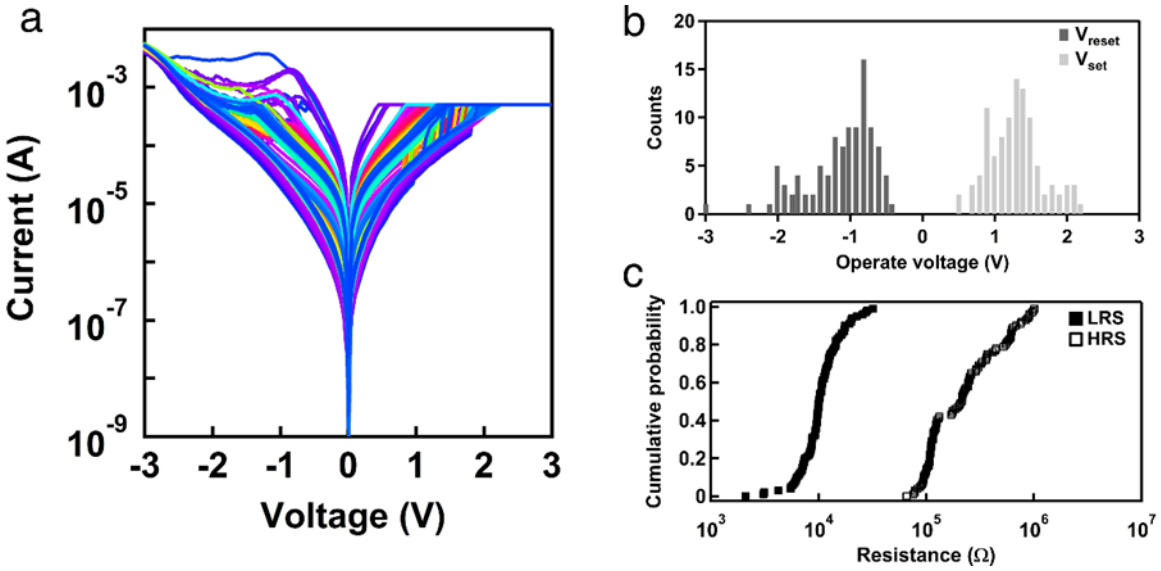

Figure 5.1. a. I-V curve during 100 cycles DC sweeping on Ti/HfO_2/Pt RRAM device. b. histogram of the set and reset voltage over 100 cycles. c. The corresponding cumulative probability of the resistance values at HRS and LRS.

As the most promising candidate for the next generation nonvolatile memory device with high scalability, high speed and low power consumption, the large-scale manufacturing of RRAM is targeting to replace the conventional flash memories for future data storage. The commercialization of RRAM has progressed rapidly in the last decade. At the same time, several challenges still remain, in terms of device uniformity, endurance, retention and high density integration.[97] [126] [127] Among the performance issue today, poor uniformity becomes a major task for commercial

realization. Intense parameter fluctuation may occur from cycle to cycle or device to device, leading to serious reliability problems as well as programming and readout issues. The cycle-to-cycle uniformity includes the variation of the operate voltage, V_{SET} and V_{RESET}, and the HRS/LRS resistance values.

For CF-based RRAM devices, the underlying origin of the fluctuations is considered to be the stochastic nature of filaments generated from the continuous switching process, including the ion motion associated with the generation and recombination of oxygen vacancies or variation on number/size of conducting filaments formed in the SET process.[128] [129] The switching process does not typically form a single columnar unit bridging the top and bottom electrodes within the oxide film, but forms multiple local, competitive pathways during CF formation. Even a small variation may induce intense parameter fluctuations including operate voltages, HRS/LRS resistance and reset current and further cause retention and endurance problems. Especially, the fluctuation of V_{SET} may be explained in terms of the varying tunneling gap between the filament tip and the counter electrode generates in the RESET process. Remarkably, simulation results show that a small variation, i.e. 0.1 nm, in tunneling gap distance can create a significant resistance change of 10^2, thus gives rise to large distribution of V_{SET}.[130] Pushing forward studies revealing the details of the continuous filament formation and rupture from a microscopic point of view provide a potential pathway to solve the difficulties in controlling the filamentary activity during the resistive switching process. Figure 5.1 shows a typical I-V characteristic of traditional HfO_2 memristor during 100 cycles. It represents a typical bipolar switching behavior with a poor repeatability from cycle to cycle. The histograms in Figure 5.1 b shows the operating voltage range and cumulative probability in Figure 5.1c demonstrates the resistance value distributions transferring from the I-V curves. A large voltage range exists from -3 to -0.4 V and 0.5 to 2.2 V for V_{SET} and V_{RESET}, respectively.

One effective approach to control the growth of CF is the inclusion of metallic nanostructures embedded within oxide films. These systems exhibit multilevel switching, enhanced retention, higher on/off ratios, and lower operating voltages, all attributed to enhanced local electric fields and higher vacancy concentrations.[131] [132] Previous studies proposed possible solutions for solving the uniformity problems, and one is by choosing the proper material system. TiO_2, a well-studied prototype switching material is facing serious reliability issues result from the large range of its non-stoichiometry at room temperature, which due to its complicated oxidation state in TiO_x matrix.[69] In this case, an effective way is to use metal oxide that presents stable chemical states, Ta_2O_5 and HfO_2 for instance, decreasing the possible different resistance levels.

An alternative type of solution has been reported is engineering the interface structure, such as inserting a buffer layer between the metal oxide and electrode. Here the buffer layer can typically be, but not limit to, metal, oxide or nitride thin film, providing improvement in uniformity and reliability. It has been observed excellent switching uniformity and reliability by introducing an Zr metal layer.[133] The induced ZrO_x/HfO_x bilayer precisely controls the oxygen vacancy concentration in HfO_2 and creates a tunneling barrier within HfO_x for the reset process. Another recent study relates to the interface engineering technique utilized the highly ordered Ag nanocones, serving as the electric-field concentrators so that achieving selective and controlled filament growth.[134] In this work, the conventional cell and the nanopatterned cell have been compared, implying the narrowed operating voltage distributions is attributed to the guided growth of Ag filament. Moreover, the confined conducting path is visualized as bright spots by c-AFM, indicating the correlated locations of the nanocones and the Ag filament.

The third method regards to the confinement of conducting filament by concentrating the local electric field at the region where nanoparticles are inserted, but not

achievable by the continuous intermediate layer. Efforts towards embedding metal nanoparticles into oxide thin film for memristors have been presented as both modeling and experimental evidence that prove the enhanced resistive switching properties. Many type of metal nanoparticles, such as Ag,[132] [135] Au,[136] [137] Co,[138] Ni,[53],[139] Pd,[140] Pt,[141] Ru,[142] [143] Ti,[144] and Hf[145], have been embedded in bulk oxide material acting as an electric field concentration center.

One notable work published by Jung Ho Yoon et al[143] reported the highly improved uniformity in resistive switching behavior by inserting the Ru nanodots in TiO_2 memristor. They confirmed the reduced variation in different parameters for chosen device sizes, nanodots diameters and inserting positions. Note that the t-Ru and b-Ru, which is near anode (t-top) interface and cathode (b-bottom) interface, respectively, play different roles change from field-enhancer to field-suppressor as injecting at different positions. Tsung-Kuei et al[140] recently reported resistive switching characteristics in HfO_x memristor with embedded Pd nanocrystals into different locations. However, they did not present a reference sample for comparison, so there is no significant improvement can be observed. Furthermore, they conclude that the resistive switching character is closely related to the forming process, which is unreasonable due to the missing analysis of V_{SET}/V_{RESET} distribution. In fact, the cycle-to-cycle uniformity and device failure phenomenon display strongly dependency on the repeating set and reset process. Although these works pointed out the direction for solving the main problems and improved the performance to some extent, the randomly dispersed nature, unpredictable density and large size distribution of nanoparticles remain an issue, thus hindering the maximization of filament confinement origins from asymmetric electric field. Min Ju Yun et al[144] demonstrated optimized resistive switching properties using several metal nanocrystals embedded in NiN-based memristor. The different work functions between metal nanocrystals and bulk NiN are claimed to introduce different conduction mechanism,

which enables further improvement by precisely calculating the induced potential barrier height. However, investigation of comparing different metal nanoparticles in oxide-based memristor is still lacking, where associated issues need to consider including their different oxygen affinity and mobility when involved in oxide material. Importantly, although the embedded species is known to be field concentrator, the additional correlations between metal and the oxide matrix are not yet clear. Indeed, oxygen sink or vacancy sink behaviors are believed to form closely around the nanoparticle based on the electrochemical active level of the metal type.

In these cases, however, the embedded nanostructures suffer from random distributions, unpredictable density, and highly variable sizes of metallic nanoclusters in the oxide layer, which are typically fabricated either by ion bombardment or an annealing/dewetting process. The recrystallization process is highly dependent on temperature and environment. While the cluster size has been shown to depend on metal electronegativity,[144] the size and distribution of embedded metal nanocrystals has not been systematically varied or controlled. This may further cause the device-to-device uniformity issues due to the spatial variety of the nanostructures. On the other hand, the inclusion of these metals to modulate the barrier height and help dictate the conduction mechanism motivated us to confine, pre-define, and directly probe the ionic interactions between the embedded nanocrystals and the surrounding oxide. Though the embedded species is known to locally concentrate the electric field, additional correlations between the metal and the oxide matrix, such as the effects of oxygen affinity and mobility, remain unclear.

5.1.1 Summary of the embedding nanoparticles approach

- Inserted nanoparticles of different types of metal with varying sizes.☑
- Improved the uniformity and reliability to some extent.☑
- Showed observation of conductive filament and composition analysis.☑

- Built the simulation model of electrical field distribution for embedded sample.☑
- Thermal dewetting yields nanoparticles of random dispersion and density.☒
- No experimental evidence towards the correlation between the position where the conducting filament formed and the nanoparticles.☒
- The understanding of the roles that different metals play within the oxide switching layer is still missing.☒

Aiming at improving the variability on redox-based resistive switching devices, we established a simple, versatile template-assisted fabrication scheme to embed ordered metallic arrays in the archetype switching oxide hafnia HfO_2, the first demonstration of fully patterned nanostructures in a memristive oxide film, thus eliminating the random spatial distribution that plagues currently employed approaches to prevent the further issue of device-to-device variability. We illustrated thin films embedded with ordered arrays of Pt, Ti, and Ag nanoislands (NIs) all exhibit significantly reduced operating voltages and drastic improvements in overall uniformity of the LRS and HRS.

5.2 Templated-Directed Device Fabrication

As a low-cost approach competing with complicated multi-step lithographic processes, ultrathin anodic aluminum oxide (AAO) template provides highly ordered individual patterns meanwhile with attractive advantages involving large scale fabrication. AAO boasts additional advantages such as large scale fabrication, and tunablility of the nanopore size, thickness and interpore spacing, motivating its use in recent studies of RRAM devices.[146] [147] [148] [149]

Figure 5.2 shows the templated-directed process developed for embedding ordered metal nanoisland (NI) arrays within the oxide layer of M-O-M structures. The process begins with the deposition of i) a bottom electrode by evaporation; ii) the initial

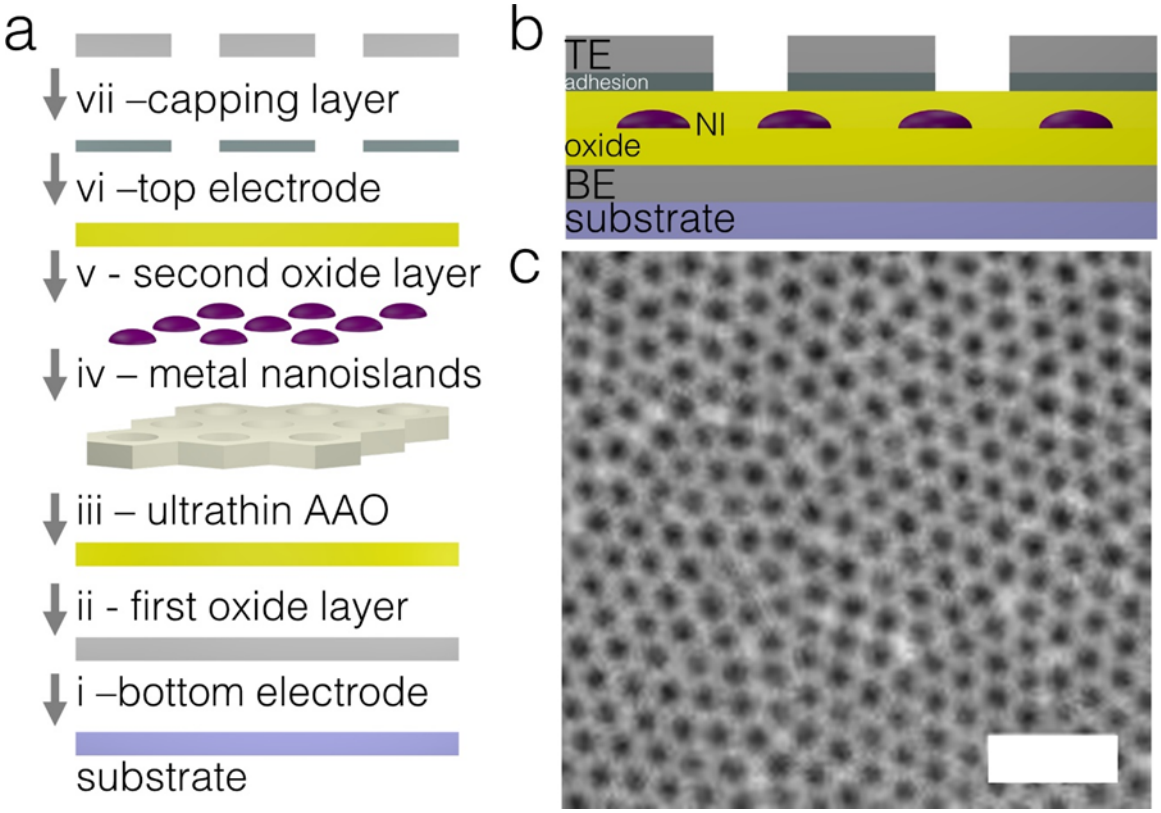

Figure 5.2. a, Illustration of the template-directed device fabrication approach. b, The cross-sectional schematic of the nanoisland embedded HfO_2 RRAM devices. c, SEM image of the ultrathin AAO template after transferring on the substrate.

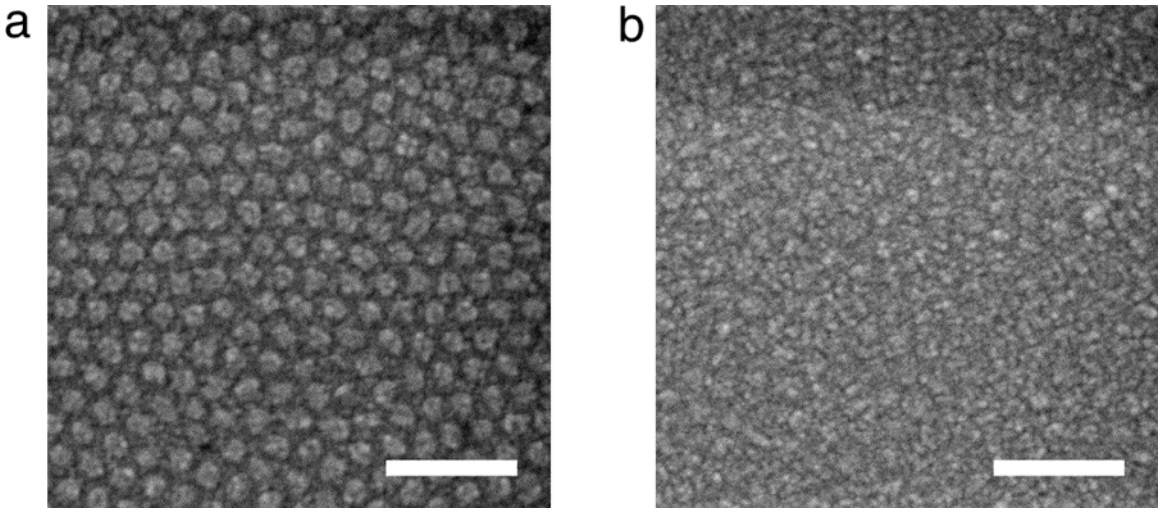

Figure 5.3. a, SEM image of the D90 nm NIs deposited on HfO_2. b, SEM image of top surface after depositing the second layer HfO_2. Scalebar: 500 nm.

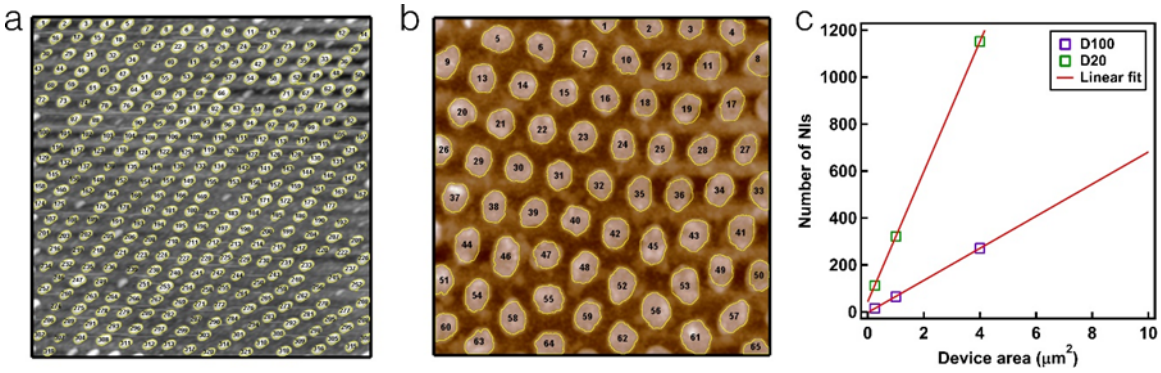

Figure 5.4. The particle analysis of the Pt nanoislands deposited on HfO_2 after removing the AAO template. a-b, Surface topography of highly-ordered nanoisland arrays for D30 and D90, respectively. c, A plot of the number of nanoislands versus the device area, indicating a controllable density of the nanostructure by using template-driven approach.

oxide layer by atomic layer deposition (ALD); iii) transfer of ultrathin (aspect ratio < 8) AAO templates on the first oxide layer; iv) templated metal nanoislands by evaporation; v) a second oxide layer by ALD; patterned vi) top electrode and vii) capping layers. The NIs are deposited via AAO templates with two different pore sizes (30 and 90 nm), follow by a mechanical removal of the template allowing well-ordered. NI arrays comprising three types of metals (Pt, Ti, Ag) of two different diameters were embedded into ALD-prepared HfO_2 thin films, denoted Pt-D30/Pt-D90, Ti-D30/Ti-D90, and Ag-D30/Ag-D90 hereafter. A SEM image of ultrathin AAO template (Fig. 5.2c) after transferring, periodic NI arrays achievable through the simple template-assisted deposition approach in Figure 5.3. The nanoisland diameter, inter-island spacing and the resulting area density are precisely controlled through changes in the pore size by varying the anodization voltage during template fabrication. The highly ordered, consistent structure of the NI arrays has been confirmed by SEM images in Figure 5.3a. After the second oxide layer deposition, the topography has also been examined by SEM in Figure 5.3b.

In order to prepare the device, a 5 nm Ti adhesion layer and 30 nm Pt bottom electrode was deposited by evaporator sequent on the SiO_2/Si substrate. 5 nm HfO_2 oxygen layer were grown by (ALD) at 250°C with Tetrakis(dimethylamino)hafnium and H_2O as Hf precursor and oxygen source, respectively. The AAO template (Top-Membranes Inc., Shenzhen, China) was transfer onto HfO_2 with two different pore sizes (20 and 100 nm), follow by the deposition of metal thin film (Ti, Pt, Ag) of 3.5 nm using evaporation. After removing the template, another HfO_2 layer of 5 nm in the same conditions was obtained using ALD. Finally, 30 nm Ti top electrode and 15 nm Pt capping layer with diameter of 50 μm was deposited to form the memristor device. A Ti/HfO_2(10 nm)/Pt structure with no embedded NIs was prepared for reference propose. The cross-section of embedded sample was observed by high resolution transmission electron microscopy (HRTEM). The topography was characterized by atomic force microscopy (AFM) and scanning electron microscopy (SEM).

The number and density of the NIs have been thoroughly examined by the particle analysis in ImageJ software. Figure 5.4 demonstrates the well-ordered NI arrays of Pt after template removal. The calculated average sizes based on a 1 μm topography scan was 29.7 $\pm$ 3.0 and 92.2 $\pm$ 6.7, respectively. Therefore, we use D30 and D90 indicate the different size of the NIs in this chapter. Furthermore, the number of NIs increases with increasing device area as shown in Figure 5.4c, indicating a precisely controlled density which can be determined according to the linear relationship between number of NIs and the device area. The density is approximated as $227 \pm 2\mu m^{-2}$ and $68 \pm 1\mu m^{-2}$, respectively.

5.3 Switching Performance of Embedded Memristors

To demonstrate the electrical performance of the embedded devices, the I-V character was analyzed over 100 cycles of DC voltage sweeps using a probe station. Figure

Table 5.1. The statistical results of $V_{SET}$and V_{RESET}comparing the bare HfO_2 and embedded HfO_2 memristors.

	SET voltage (V)			RESET voltage (V)		
	Average	STDEV	Reduction (%)	Average	STDEV	Reduction (%)
Pt-D30	0.953	0.220	26.4	-0.806	0.034	28.1
Ti-D30	0.943	0.138	27.2	-0.813	0.167	27.5
Ag-D30	0.398	0.122	69.3	-0.414	0.091	63.1
Bare HfO_2	1.295	0.363	0	-1.121	0.484	0
Pt-D90	0.743	0.238	42.6	-0.533	0.099	52.5
Ti-D90	0.849	0.151	34.4	-0.737	0.212	34.3
Ag-D90	0.373	0.129	71.2	-0.371	0.115	66.9

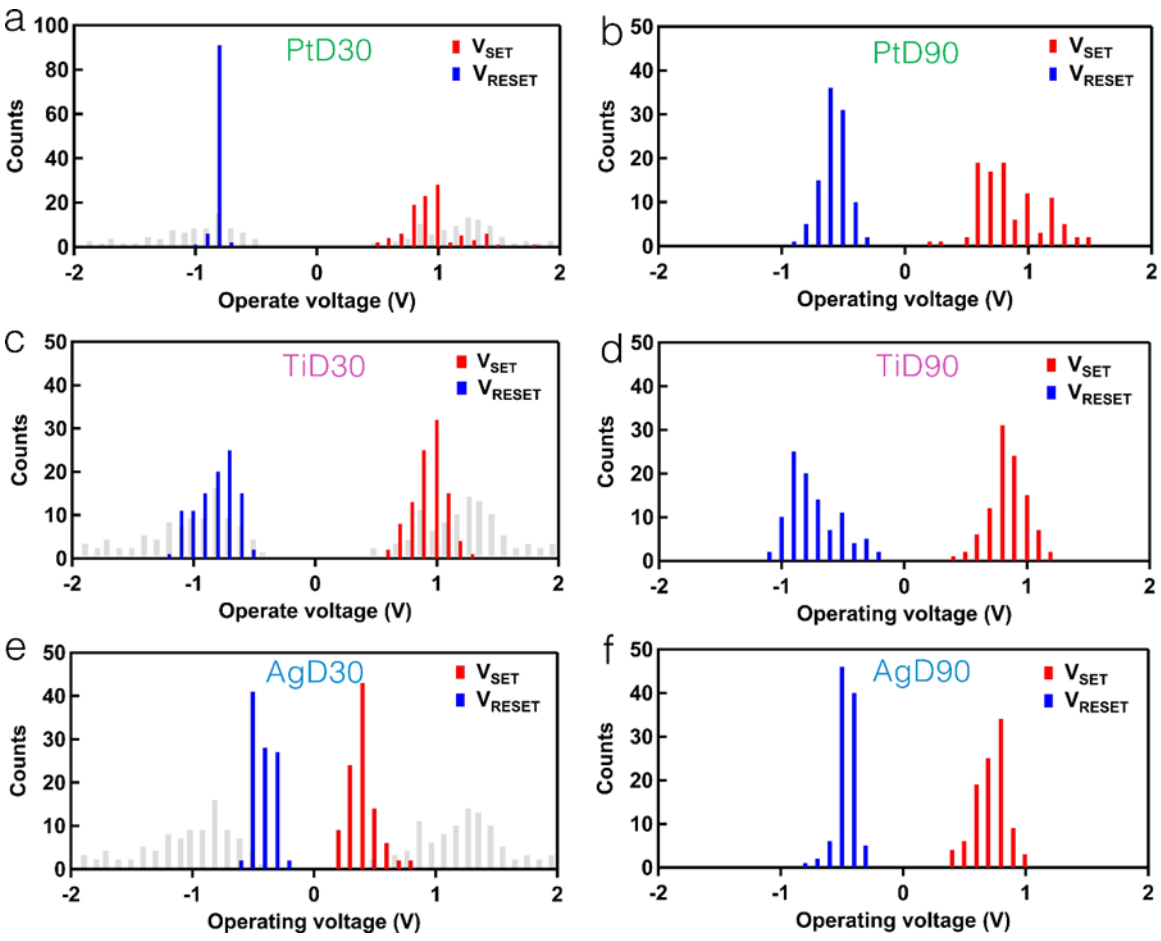

Figure 5.5. Histograms of operating voltage distribution of embedded HfO_2 with Pt, Ti and Ag nanoislands with diameter of a-c, 90 nm and d-f 30 nm. A gray histogram indicates the operating voltage of bare HfO_2 memristor inserted as the background for the purpose of comparison.

5.5 compares the histograms of the set (red) and reset (blue) voltages of Pt (Figs. 5.5a,b), Ti (Figs. 5.5c,d) and Ag (Figs. 5.5e,f) embedded memristors to that of a bare HfO_2 control film without any embedded nanoislands (grey; Figs. 5.5a-f). Table 5.1 summarizes the details of the statistical data found in the histograms of the metal nanoisland-embedded films (Figs. 5.5a-f). The reference control films exhibited an average V_{SET} and V_{RESET} of 1.295 $\pm$ 0.363 and -1.121 $\pm$ 0.484, respectively. The ordered embedded nanoisland arrays of all metal types and diameters yielded a significant reduction in operating voltage. Two distinct trends are observed in the performance of the ordered, embedded nanoisland arrays. The first trend shows Ag nanoislands of either size lower both V_{SET} and V_{RESET} more effectively than either Pt or Ti nanoislands; for the D30 systems the order of highest to lowest percentage reduction is Ag > Ti > Pt, for D90 systems Ag > Pt > Ti. These devices exhibit both VCM and electrochemical metallization process (ECM), where electrochemical metal deposition/dissolution cycles enable switching between active and inert electrodes, has been illustrated in Ag nanoparticle-embedded Al_2O_3 thin films. The second trend shows that generally the larger diameter D90 systems reduce both the V_{SET} and V_{RESET} values more effectively than their smaller D30 counterparts, but display slightly broader distributions (higher standard deviation).

The ordered, embedded nanoisland systems also significantly enhanced the cycle-to-cycle resistance uniformity compared to the bare HfO_2 thin films, as shown in the plots of the cumulative probability of resistance for 100 cycles between the HRS and LRS of both the embedded and reference devices in Figure 5.6. Full statistics can be found in Table 5.2. The bare HfO_2 reference films exhibit significant changes in the resistance values and consequently large coefficients of variation (CV) for the LRS (Figs. 5.6a,b; grey open) and HRS (Figs. 5.6a,b; grey solid). The Pt-D30 system displayed exemplary uniformity enhancements (Fig. 5.6a, green), with an overall 95% reduction in CV of the LRS and 89% reduction in CV of the HRS! The Pt-

D90 system (Fig. 5.6b, green) also significantly reduced the CV by a factor of 68% (LRS) and 79% (HRS), respectively. The Ag-embedded films similarly yielded stark improvements to the uniformity, with a reduction in CV of the set/reset voltages of 55% and 75% for the Ag-D30 system and 41% and 56% in the Ag-D90 system, respectively (Figs. 5.6a,b; azure). Devices embedded with ordered Ti nanoisland arrays, however, exhibited only nominal improvements ($\sim$ 5% or less) in uniformity for the Ti-D30 system (Fig. 5.6a; magenta) and moderate improvements (41% in CV of V_{SET}; 56% in CV of V_{RESET}) for the Ti-D90 system. Based on the results shown in Figure 5.5, 5.6 and Tables 5.1 and 5.2, the embedded nanoislands clearly reduced the operating voltage (Ag, the most) while improving the cycle uniformity (Pt, the most). We attribute the differences in performance between the embedded nanoisland systems to the properties of the metal types itself. While the embedded Ag systems work under the ECM principles involving cation migration mentioned earlier, the Pt and Ti systems leverage the filamentary dynamics of oxygen vacancies to enable a valence change mechanism, the evolution and manipulation of which serves as the focus of this study. Figure 5.7 shows the resistance versus number of cycles at HRS and LRS for the reference, m-TiD90 and m-PtD90, respectively. Note that both reference and m-TiD90 display an extensive degradation of the resistive level during 100 cycles, which is significantly improved in the m-PtD90 system. In other words, a large ON/OFF ratio as 10^3 can be maintained with an increasing number of cycles by embedding PtD90.

The physical origin of the resistance fluctuations arises from the variation in the number and/or size(s) of the conductive filaments or ion motion associated with the generation and recombination of oxygen vacancies. The enhanced performance uniformity is attributed to the confinement of the conductive filament growth pathway. Simulations of the electric field distribution surrounding embedded species within a dielectric film matrix showed that the highest field concentration occurs at the

edge of nanostructure, favorable for both electrochemical reduction and oxygen vacancy migration processes.[143] Embedding metal nanoislands within the oxide thin film concentrates the electric field such that the fast oxygen reduction occurs only between the Ti top electrode and the location of the nanoisland array. Controlled growth of the conductive filamentary channel is subsequently achieved by electric field modulation, manifested as a reduction in operating voltages and a narrowing of their subsequent distributions.

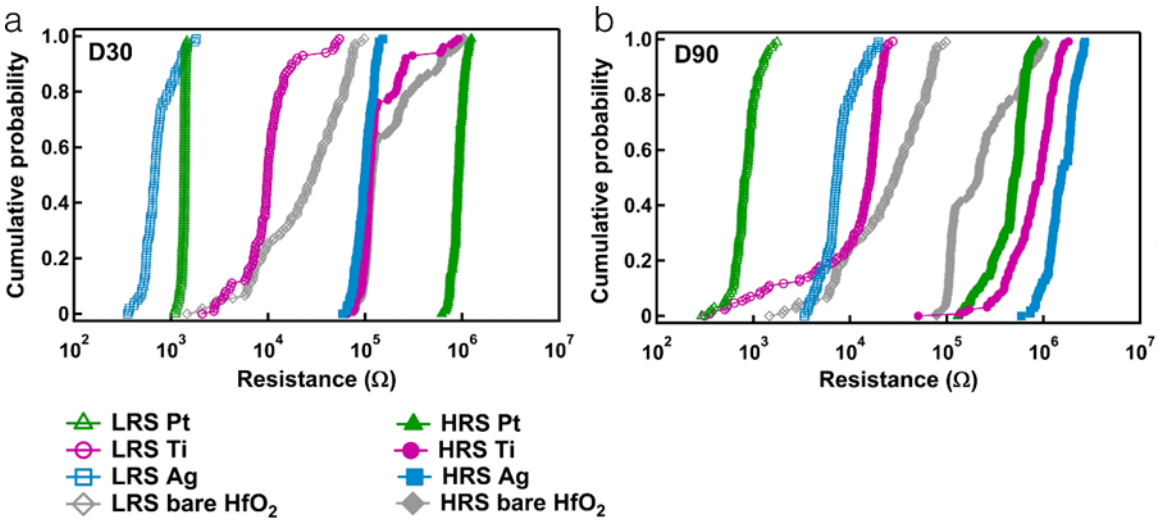

Figure 5.6. Resistance cumulative probability of different embedded memristor with nanoisland diameter of a, 30 and b, 90, respectively.

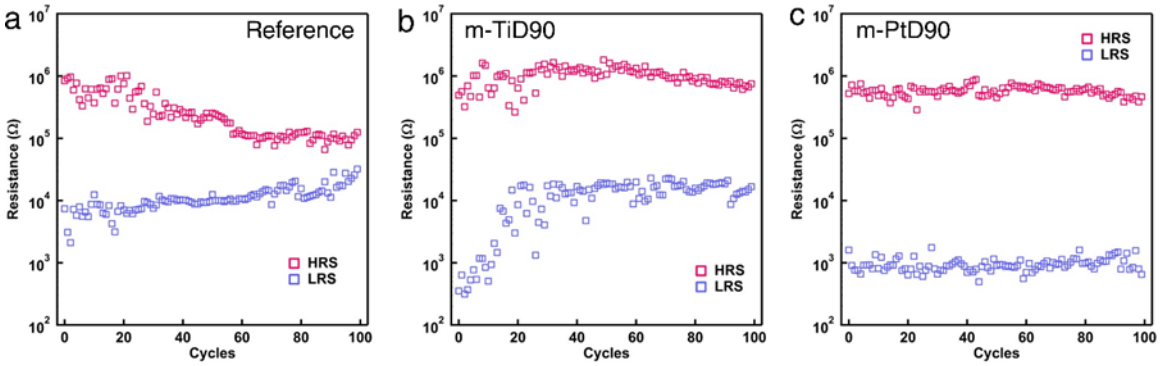

Figure 5.7. Resistance values at HRS and LRS read at 0.2 V during 100 cycles for a. reference device, b. m-TiD100 and c. m-PtD100, respectively.

Table 5.2. The statistical results of resistance at LRS and HRS comparing the bare HfO_2 and embedded HfO_2 memristors.

	Low resistance (KΩ)			High resistance (MΩ)		
	Average	STDEV	CV (%)	Average	STDEV	CV (%)
Pt-D30	1.351	0.072	5.3	0.919	0.101	11.0
Ti-D30	12.051	9.999	83.0	0.165	0.155	93.9
Ag-D30	0.750	0.285	38.0	0.096	0.024	25.0
Bare HfO_2	26.441	22.491	85.1	0.229	0.227	99.1
Pt-D90	0.939	0.253	26.9	0.550	0.115	20.9
Ti-D90	13.862	6.983	50.4	0.877	0.386	44.0
Ag-D90	8.134	3.562	43.8	1.601	0.515	32.2

The ordered, embedded nanoisland systems also significantly enhanced the cycle-to-cycle resistance uniformity compared to the bare HfO_2 thin films, as shown in the plots of the cumulative probability of resistance for 100 cycles between the HRS and LRS of both the embedded and reference devices in figure 5.6. Full statistics can be found in Table 5.2. The bare HfO_2 reference films exhibit significant changes in the resistance values and consequently large coefficients of variation (CV) for the LRS (Figures 5.6a,b; grey open) and HRS (Figures 5.6a,b; grey solid). The Pt-D30 system displayed exemplary uniformity enhancements (Figure 5.6a, green), with an overall 95% reduction in CV of the LRS and 89% reduction in CV of the HRS! The Pt-D90 system (Figure 5.6b, green) also significantly reduced the CV by a factor of 68% (LRS) and 79% (HRS), respectively. The Ag-embedded films similarly yielded stark improvements to the uniformity, with a reduction in CV of the set/reset voltages of 55% and 75% for the Ag-D30 system and 41% and 56% in the Ag-D90 system, respectively (Figs. 5.6a,b; azure). Devices embedded with ordered Ti nanoisland arrays, however, exhibited only nominal improvements ($\sim$ 5% or less) in uniformity for the Ti-D30 system (Figure 5.6a; magenta) and moderate improvements (41% in CV of V_{SET}; 56% in CV of V_{RESET}) for the Ti-D90 system. Based on the results shown in figure 5.5, 5.6 and Tables 5.1 and 5.2 , the embedded nanoislands clearly reduced

the operating voltage (Ag, the most) while improving the cycle uniformity (Pt, the most). We attribute the differences in performance between the embedded nanoisland systems to the properties of the metal types itself. While the embedded Ag systems work under the ECM principles involving cation migration mentioned earlier, the Pt and Ti systems leverage the filamentary dynamics of oxygen vacancies to enable a valence change mechanism, the evolution and manipulation of which serves as the focus of this study. figure 5.7 shows the resistance versus number of cycles at HRS and LRS for the reference, m-TiD90 and m-PtD90, respectively. It should be noted that both reference and m-TiD90 displace an extensive degradation of the resistive level during 100 cycles, which has been significantly improved in m-PtD90 system. In other words, it can be maintained a large ON/OFF ratio as 10^3 with increasing number of cycles by embedding PtD90.

The physical origin of the resistance fluctuations arises from the variation in the number and/or size(s) of the conductive filaments or ion motion associated with the generation and recombination of oxygen vacancies. The enhanced performance uniformity is attributed to the confinement of the conductive filament growth pathway. Simulations of the electric field distribution surrounding embedded species within a dielectric film matrix showed that the highest field concentration occurs at the edge of nanostructure, favorable for both electrochemical reduction and oxygen vacancy migration processes. Embedding metal nanoislands within the oxide thin film concentrates the electric field such that the fast oxygen reduction occurs only between the Ti top electrode and the location of the nanoisland array. Controlled growth of the conductive filamentary channel is subsequently achieved by electric field modulation, manifested as a reduction in operating voltages and a narrowing of their subsequent distributions.

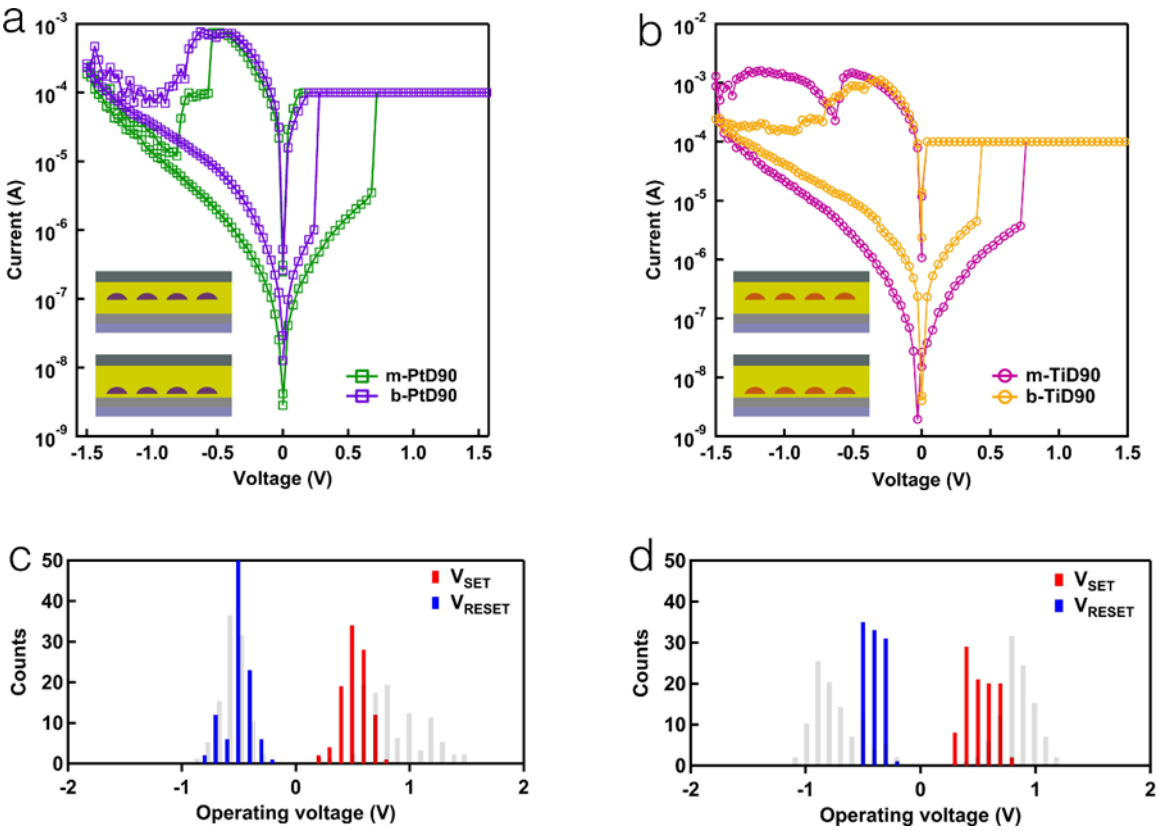

Figure 5.8. The comparison of the resistive switching characteristics of PtD90 embedded memristor in different thickness dimension. a. I-V response of m-PtD90 and b-PtD90 with b-PtD90 shows a reduced and narrowed range of V_{SET}. b. histogram of the operating voltage of b-PtD90. The gray histogram in the background indicates the operating voltage distribution of m-PtD90, showing an improved uniformity by moving the NIs towards bottom electrode. c. representative I-V curve of m-TiD90 and b-TiD90, respectively. d. histogram of the operating voltage of b-TiD90. Inset of a and d shows the position of the embedded NIs.

Table 5.3. The statistical results of operating voltages of Pt and Ti embedded HfO_2 devices inserted at different thickness position

	SET voltage (V)			RESET voltage (V)		
	Average	STDEV	Reduction (%)	Average	STDEV	Reduction (%)
m-PtD90	0.953	0.220	26.4	-0.533	0.099	52.5
b-PtD90	0.734	0.132	43.3	-0.499	0.115	55.5
Bare HfO_2	1.295	0.363	0	-1.121	0.484	0
m-TiD90	0.849	0.151	34.4	-0.737	0.212	34.3
b-TiD90	0.560	0.127	56.8	-0.393	0.078	64.9

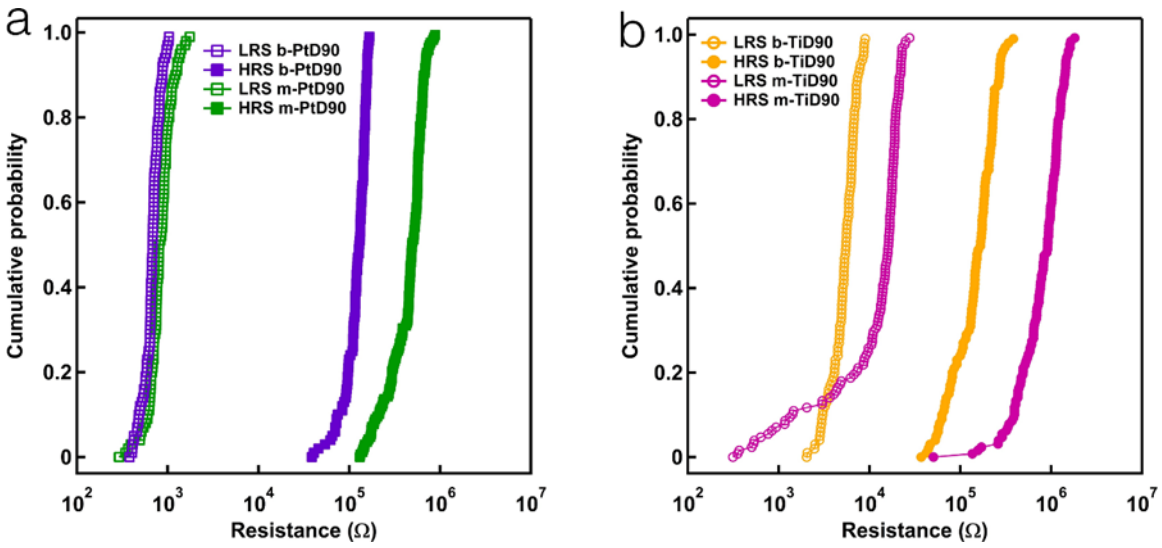

Figure 5.9. a, Comparison of the cumulative probability of the resistance in LRS and HRS, suggesting a decreased HRS can be observed in b-PtD90. b, comparison of the cumulative probability of the resistance in LRS and HRS, suggesting a decreased HRS and resistance distribution in each state.

5.3.1 Inserting NI Arrays Near the Bottom Electrode

Embedding ordered nanoisland arrays to effectively limit the variability that occurs in bare HfO_2 memristive films generates a secondary challenge of narrowing the V_{SET} and the reset resistance distributions. To address these issues, the position of the nanoisland array was moved along the film thickness dimension and then its influence on the switching performance was explored. Altering the sequence in Figure 5.2a to deposit only a 1 nm HfO_2 thin film in step iii) shifted the placement of a Pt-D90 nanoisland array from the film middle to the film bottom (defined by the thickness of the film in step iii above the bottom electrode), labelled hereafter as b-PtD90 as shown within the inset of Figure 5.8a. Figure 5.8 compares the I-V responses of m-PtD90 (green) and b-PtD90 (purple) (Fig. 5.8a) and the operating voltages (Fig. 5.8c), respectively. Figure 5.8b shows the b-PtD90 system exhibits a stark reduction in V_{SET} (red) and V_{RESET} (blue) compared to the m-PtD90 system (grey), and a narrower overall V_{SET} distribution. Their statistical summary can be found in Table

Table 5.4. The statistical results of resistance at HRS and LRS of device with embedding NI at varying thickness positions.

	Low resistance (KΩ)			High resistance (MΩ)		
	Average	STDEV	CV (%)	Average	STDEV	CV (%)
m-PtD90	0.939	0.253	26.9	0.550	0.115	20.9
b-PtD90	0.684	0.140	20.5	0.122	0.030	24.6
Bare HfO_2	26.441	22.491	85.1	0.229	0.227	99.1
m-TiD90	13.862	6.983	50.4	0.877	0.386	44.0
b-TiD90	5.354	2.177	40.7	0.175	0.075	42.9

5.3 and 5.4. Similar improvements were also observed for m-Ti90 vs b-TiD90 systems, as shown in Figures 5.8c,d, further demonstrating the strong correlation between the reset process and the position of the nanoisland arrays along the film thickness dimension. This reduction likely originates from adjusting the space between the tip of the filament and the bottom electrode, a gap that ultimately dictates the high resistance state and set voltage. Figure 5.9 compares the cumulative probability of the resistance of m-PtD90 and b-PtD90 (Fig. 5.9a) as well as m-TiD90 and b-TiD90 (Fig. 59b). The b-PtD90 system produces a lower HRS due to the smaller gap formed by reset process compared to the m-PtD90 system; the reduction in gap distance also produces larger electric fields that further facilitate ion migration, thus explaining the observed reduction in set voltage. Similar trends were observed in recent studies that showed decreases in gap distance yielded electric field enhancements that restricted the self-accelerating filament growth to specific sites during the set process.

5.4 EFM and c-AFM

We demonstrated the face that the difference in the volume of oxygen vacancies leads to the varying conductive regimes examined via c-AFM. The current images show significant differences in the (dark blue) local conductive spot areas for Pt-D90 ($2250 \pm 5\text{nm}^2$; Fig. 5.10e) and Ti-D90 ($4460 \pm 4\text{nm}^2$; Fig. 5.10f) systems, as measured using a tip voltage of 7 V during scanning. The presence of a second,

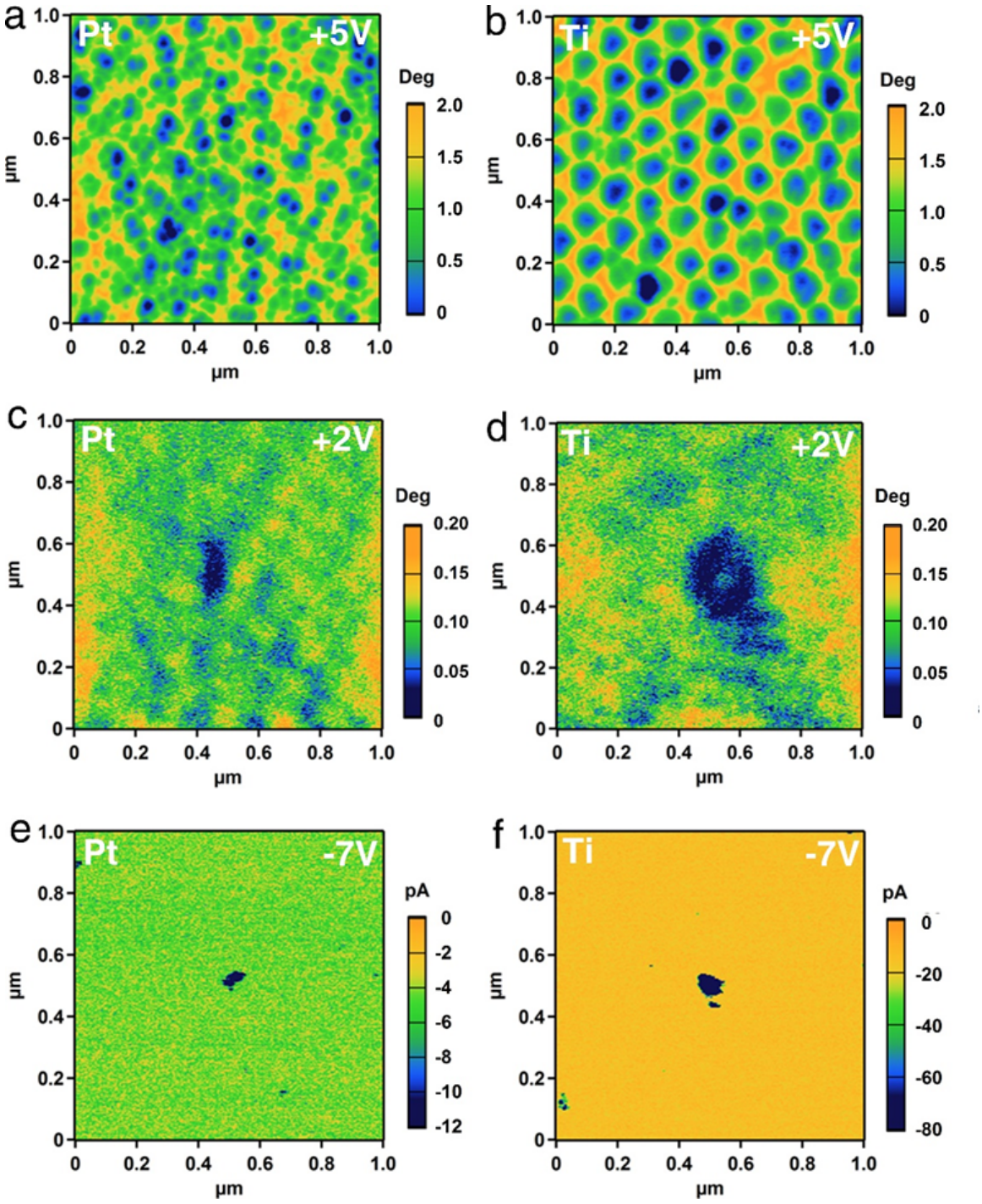

Figure 5.10. EFM and c-AFM measurements. a, EFM result of PtD90 under +5 V, the blue area represents the embedded nanoisland in HfO_2 thin film. b, EFM result after 50 cycles of locally voltage sweeping, suggesting an accumulation of oxygen vacancies under the conductive probe. c, c-AFM image shows a conductive channel around the oxygen vacancy cluster. d, EFM result of TiD90 under +5 V. e, a much larger area of oxygen vacancy accumulation can be observed under +2 V. f, c-AFM shows a conductive channel with larger size and multi-filamentary behavior.

satellite conductive spot observed in the Ti-D90 system (580 $\pm$3 nm^2; Fig. 5.10f) likely results from one of two possible formation mechanisms; i) multiple filaments formed due to a higher oxygen vacancy concentration, in agreement with a similar phenomenon reported for subfilamentary structures,[119] [150] [151] or ii) the formation of a filament network comprising multiple smaller filament branches connected to the main conducting region subsurface. A multi-branched structure likely affects the resistance level significantly, while the morphological complexity generated from each subsequent reduction cycle drives the instability observed for both the V_{SET} and ON/OFF ratio.

5.4.1 3D Observation of Conductive Channel

Nanoisland-embedded memristors of all metal types exhibit strongly enhanced switching uniformity while the apparent change in local oxygen vacancy concentration surrounding various metal nanoislands suggest different filament morphologies exist. As conductive filaments dictate both the location and mechanism of transport, and ultimately enables information storage and multi-functionality, obtaining spatially-resolved information involving their construction is required to maximize the enhancements in performance. Three-dimensional conductive-AFM (3D c-AFM) tomography,[30] [47] [152] a recently developed AFM approach, combines the sensitive force control in the z-dimension of the AFM with a hard, conductive diamond probe to sequentially remove material layer-by-layer and subsequently measure the local current, thus yielding a slice-and-view approach to observe conductive filaments within oxide-based memristors.

In order to locate the position of the conductive filament, the diameter of the top electrode has been reduced to 1 μm, which was patterned by electron beam lithography. Before scanning, I-V characteristics were collected and the devices were operated into LRS. A doped-diamond conductive tip (Bruker) with a spring constant

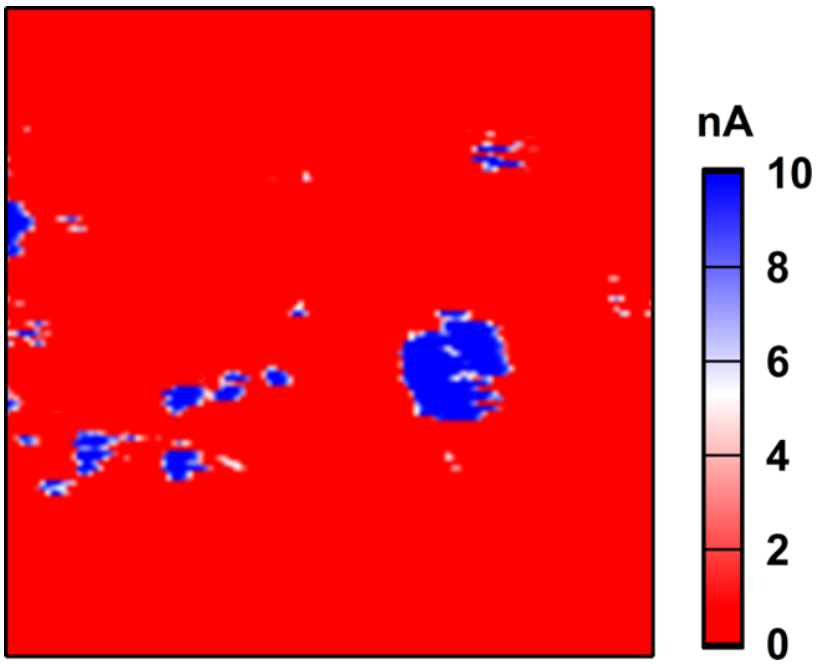

Figure 5.11. The c-AFM image (300 nm × 300 nm) on the bare HfO_2 RRAM devices surface scanned after removing the top electrode.

of [79] N/m was used as both scalpel and the current detective probe. The removal rate strongly depends on the material type and the fabrication conditions and can be controlled by adjusting the scan velocity and contact force.[153] A small scan rate of 0.3 Hz has been use to ensure a uniform removal region while a relative large force has been applied for removing the electrode material, remaining an average removal rate of 10 nm/scan. After removing the electrode, the oxide layer was entirely exposed such that the filaments were observed as multiple conductive spots and magnified to obtain high lateral resolution. The removal rate then has been reduced to about 0.5 nm/scan, leading to large number of 2D slices containing current information.

Figure 5.11 shows the current map of the bare HfO_2 device surface after removing the top electrode. One large and multiple small conductive spots can be observed, suggesting subfilamentary nature originates from the random growth of the conducting filaments. Each filament provides a potential pathway for current flow during the reset process, which explains the large variation taken place in the reference device. The

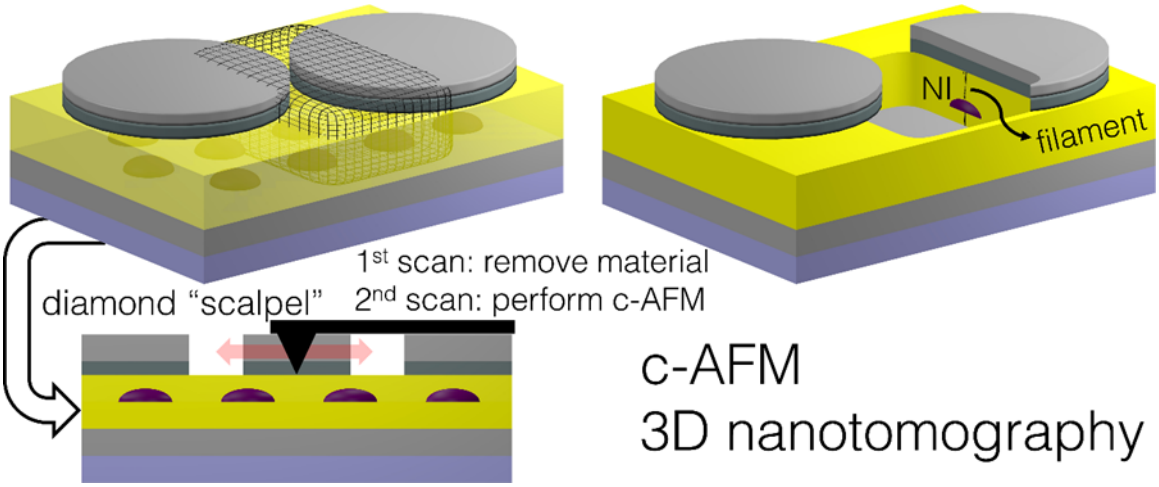

Figure 5.12. Schematic Illustration of the 3D tomography approach for conducting filament observation of b-PtD90.

subfilamentary phenomenon has been proved in recent work where the microscopic origin of the cycle-to-cycle variability was investigated in graphene/$SrTiO_3$/Nb : $SrTiO_3$ memristive devices.[150] A series of high resolution two-dimensional c-AFM images displays the evolution of local current spots corresponding to the presence of conductive filaments along the film thickness direction, thus enabling detailed analysis of the switching behavior.

In order to probe how nanoislands dictate the three-dimensional filament morphology and reduce variability, c-AFM 3D tomography was employed to observe filament formation. The devices were first subjected to 50 cycles and left with the LRS induced prior to any sample removal or measurement. Doped diamond c-AFM probes served as the nanoscalpel, which executed two separate sweeps operated in contact mode; the first sweep of removed material, the second sweep performed the conductive measurement (Fig. 5.12; bottom). Removing the electrode exposed the conducting filaments on the film surface underneath, the locations of which were magnified for subsequent scanning (Fig. 5.12, top right). A series of 2D current images (Fig. 5.13) were collected of the Pt-D90 system to produce a sequence of 3D side view conductive maps (Fig. 5.14). Here one larger, main filament was observed that spans the entire

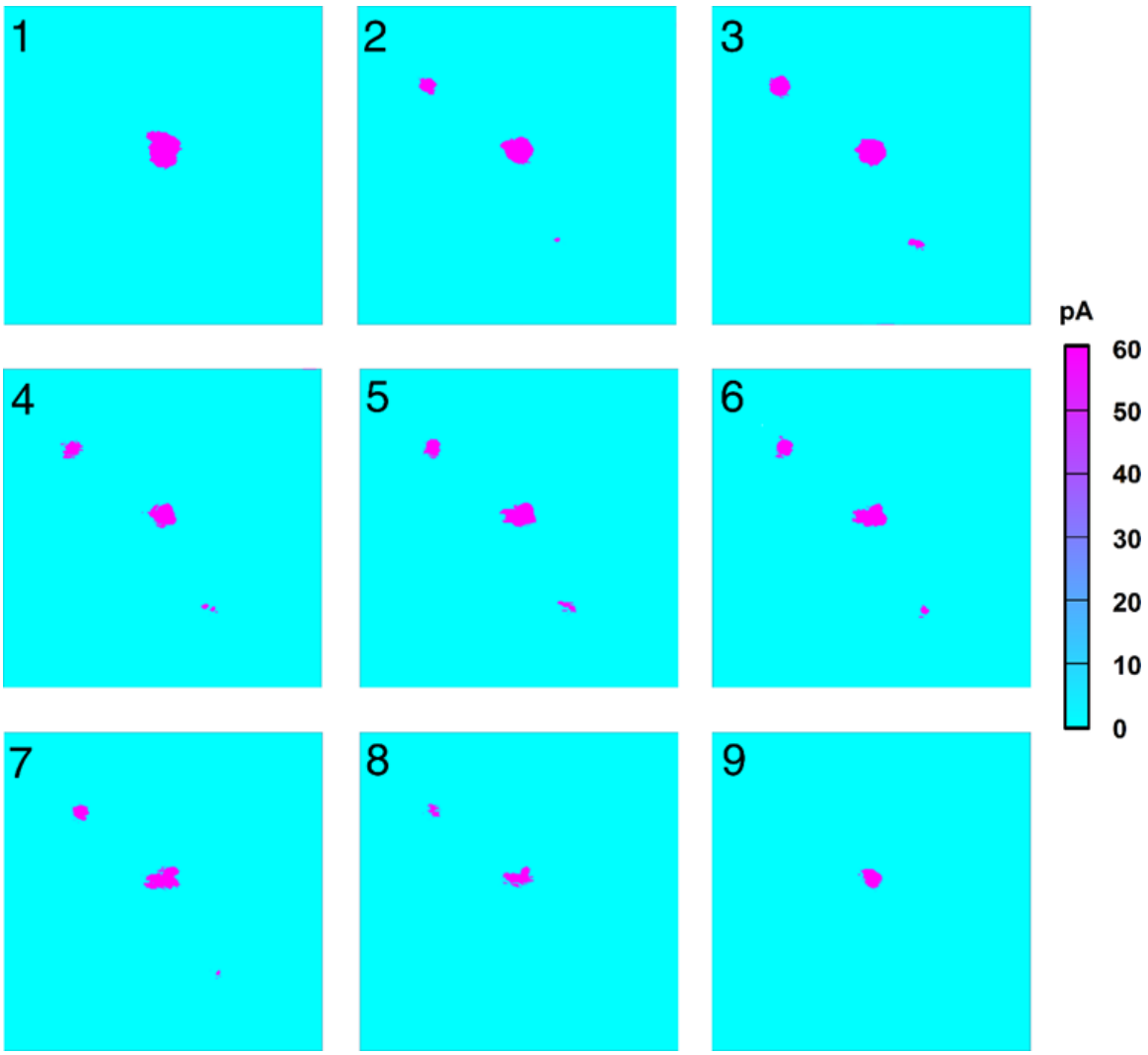

Figure 5.13. Two-dimensional current maps series (10 out of 30 slides). The conductive spots indicate the filament geometry varying from top to the bottom of the oxide layer.

film thickness from top to bottom which was flanked by two smaller, fragmented conductive channels (subfilaments; Fig. 5.14b top, bottom) that terminate within the HfO_2 layer. The main filament possessed an average diameter of 10, 15, and 20 nm, respectively, as measured at different slices along the film thickness direction of the cross-sectional profile. The main filament produces the strongest current, dominating the electrical behavior during the switching process.

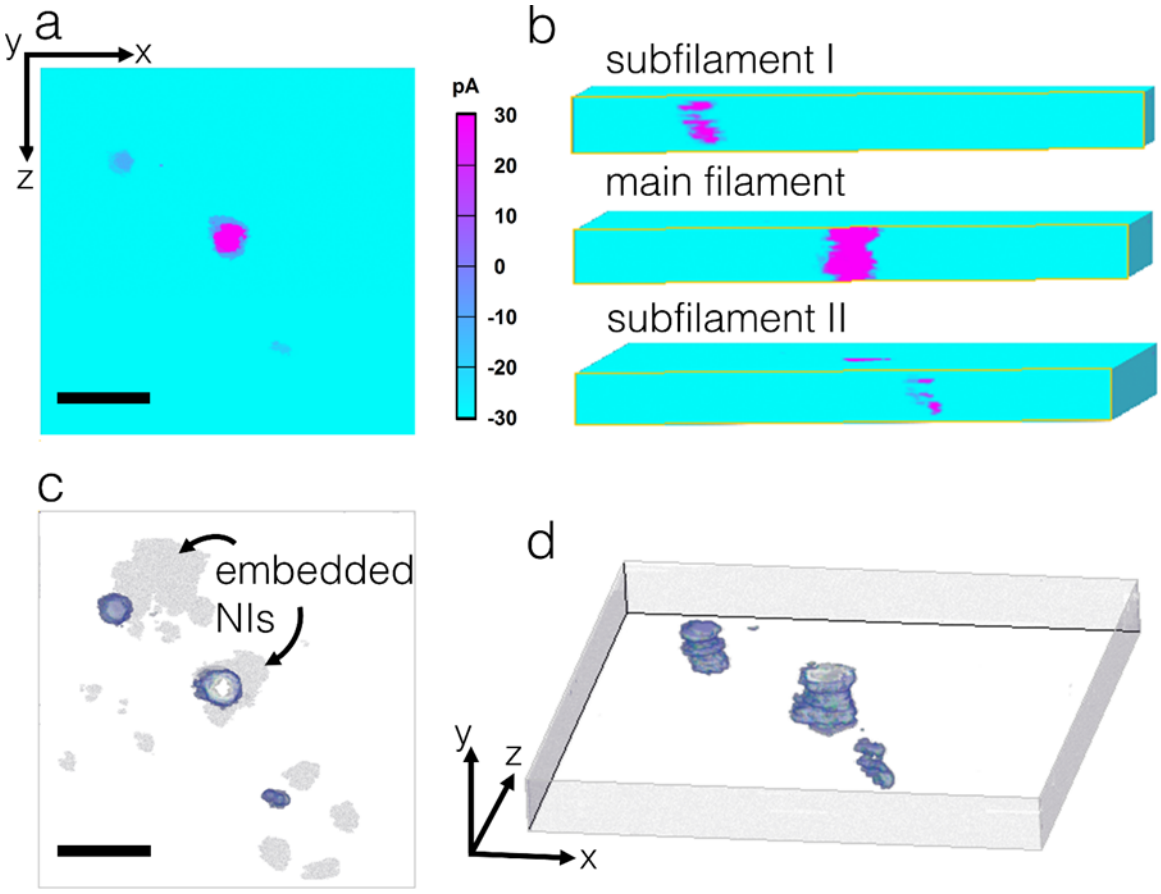

Figure 5.14. a. top view observation of 3D construction via volume viewer. b. cross-sectional observation of multifilamentary geometry inside Pt-D90. Three individual filaments with one larger and two small can be found at different cross-sectional positions. c. top view of the filament in high transparency with the shade area indicates the location of the embedded nanoislands. d. Three-dimensional structure of the conducting filament.

A combination of an hourglass-like and conical-shaped main conductive channel morphology[154] was observed (Fig. 5.14d), with an area ranging from 390 $\pm$ 2 nm^2

to 110 ± 2 nm^2 and variations in the corresponding cross-sectional diameter from 20 ± 1 nm to 10 ± 0.5 nm. The coexistence of one main and several secondary, subfilaments observed fully supports recent photoelectron emission studies of oxide thin films that showed subfilamentary formation caused cycle-to-cycle variability due to thermally-assisted recombination of oxygen vacancies.[150] A transparent 2D current image is shown in Figure 5e, which highlights the position of the main filament (blue, middle) and subfilaments (blue, upper left, lower right) relative to the embedded Pt-D90 nanoisland array (grey). Removing the HfO_2 thin film layer-by-layer along the thickness-direction of the entire device enabled the direct observation of the embedded nanoislands (grey areas) close to the bottom electrode, with the resulting filaments also visible along the nanoisland periphery. Note the filament growth follows along the outermost edge of the embedded nanoislands where the highest electric field occurs. The majority of the current flow is confined to the main conductive filament after SET operation, as evident by the highest current values observed within the largest filament in Fig. 5.14b. As the dominant filament ruptures during the RESET process,[155] each subfilament effectively competes to become the active, primary conductive pathway for the next cycle. The presence of multiple filaments thus controls the switching behavior, inducing undesired parameter fluctuation and device failure.[156] Figures 5.14b.d demonstrate the ability of 3D c-AFM nanotomography to directly observe the overall shape/morphology, spatial position, and strength for complete filament characterization.

Compared to the subfilamentary formation observed in the embedded Pt-D90 thin films, the filament morphology generated by the embedded Ti-D90 nanoisland array exhibits significantly different features, such as the enlarged area observed in the 2D current image (Fig. 5.15) and the stochastic geometry found in the 3D reconstruction (Fig. 5.16b, c). In contrast to the Pt-D90 system, the Ti-D90 system displays three separate, individual conductive pathways originating at the surface (with diameters

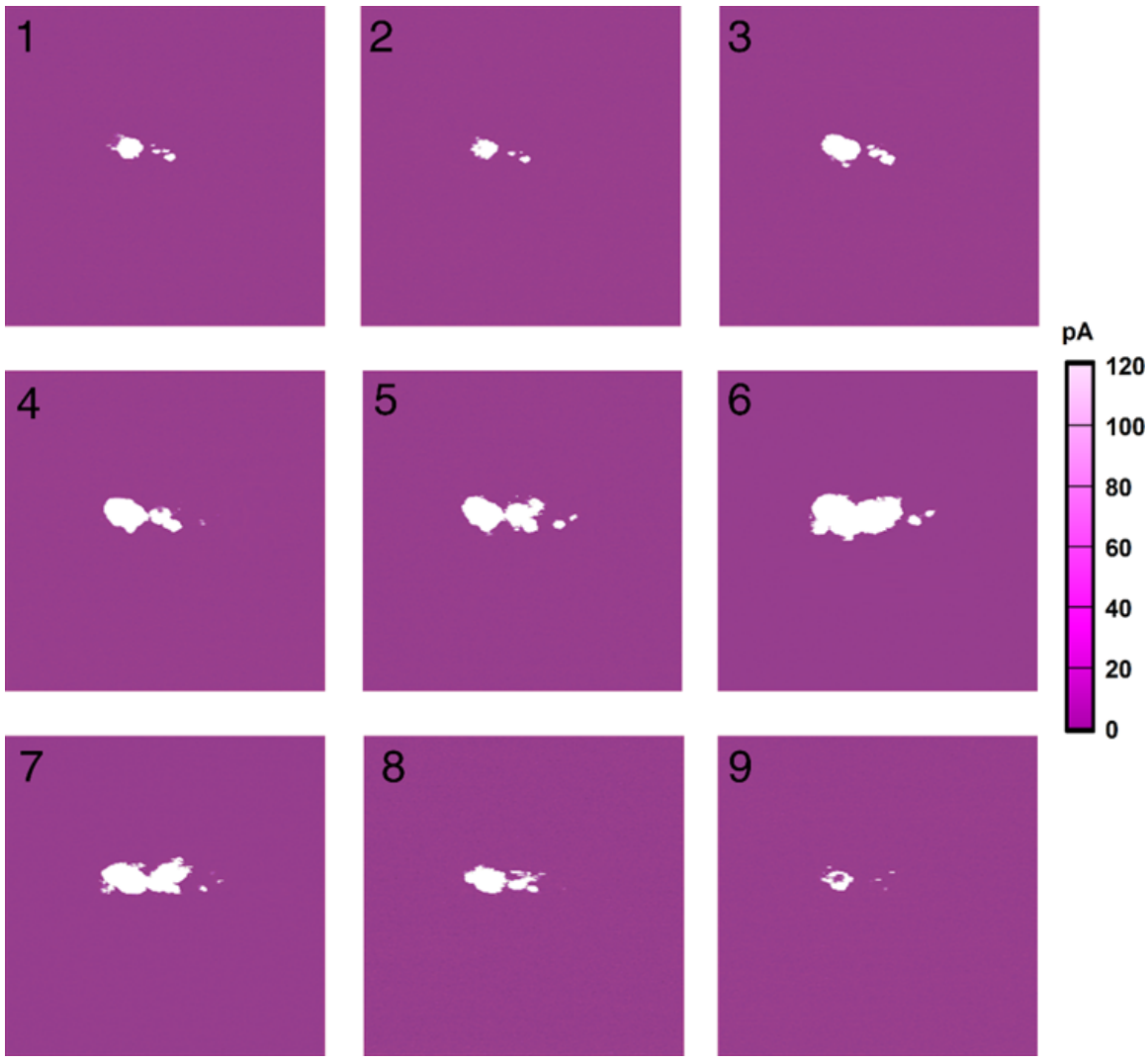

Figure 5.15. Two-dimensional current maps series (10 out of 30 slides). The conductive spots indicate the filament geometry varying from top to the bottom of the oxide layer.

ranging from 10 ± 2 nm to [79] ± 5 nm) that eventually merge to become one large, primary filament (area = 1460 ± 5 nm^2), as shown in the 3D side view current image projection in Figure 5.16a. These results are consistent with the EFM phase image (Fig. 5.10d) and current image (Fig. 5.10f) of embedded Ti-D90,which further supports an increase in the local oxygen vacancy concentration due to the Ti scavenging oxygen from the surrounding film,[157] thus creating the complex, branched network-like morphology of the conducting channel.

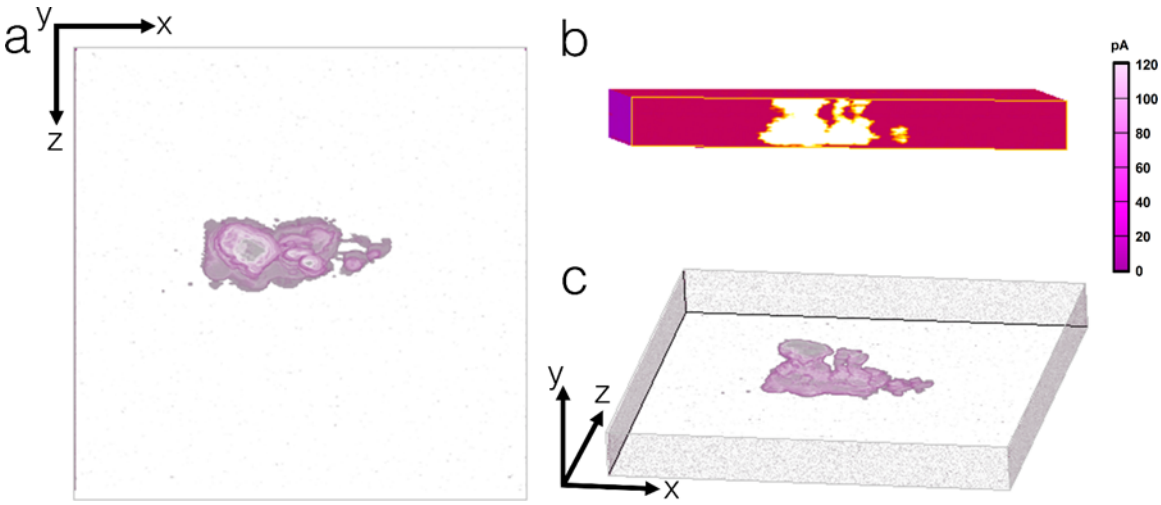

Figure 5.16. conducting filament observation of b-TiD90 on a. top view, b. cross-section and c. entire 3D structure, respectively.

The c-AFM nanotomography results shown in Figure 5.14 and 5.15 identified two separate filamentary morphologies; the existence of one large, primary filament surrounded by additional subfilamentary conductive paths in the Pt-D90 system, and the growth of a multi-branched conductive network in the Ti-D90 system. The large, stochastic nature of the branched filament network likely contributes to the severe degradation of the resistance states observed for the Ti-D90 system. Removing the top electrode of the bare HfO_2 thin film reference sample revealed multiple conducting spots (Figure 5.11) attributed to the random migration and redistribution of oxygen vacancies that drive the unexpected formation of smaller, secondary channels that

ultimately increase the number of competitive pathways during the reformation process. These results suggest that the design of embedded thin films should strongly emphasize the importance of the electrochemical stability of the nanoislands with its surround matrix. Inert nanoislands clearly simplify the morphological complexity of the conducting channel, thus reducing both the operating parameters and the cycle-to-cycle variability.

5.5 Summary of Chapter 5

Memristors have reached a critical developmental stage where emerging large scale integrations face major challenges involving the severe instability of performance parameters. Hierarchically-ordered metallic nanoislands were embedded within memristive HfO_2 thin films to overcome the random size and spatial distribution limitations of other embedded nanostructured approaches to enhance switching performance and observe conductive filament dynamics. Thin films embedded with Pt, Ti, and Ag of two distinct diameter regimes demonstrated significant reductions in both operating voltage and resistance, while also yielding enhanced cycle-to-cycle uniformity. Further improvements to V_{SET} were made possible by translating the embedded nanoisland arrays from the middle of the film towards the bottom electrode. The concentrated electric fields promoted oxygen vacancy generation and accumulation, as shown by the evolution of EFM phase and c-AFM current images between Pt and reactive Ti nanoislands. Use of the slice-and-view 3D c-AFM nanotomography confirmed the subsequent morphological differences of conductive filaments produced with Pt and Ti nanoislands. The electrochemical stability of Pt nanoislands yielded multiple, hourglass-shaped filaments found along the nanoisland periphery where the maximum local electric field enhancement occurs. A large branched filamentary network within the Ti-embedded film, resulting from the high vacancy concentrations induced as Ti extracts oxygen from the surrounding oxide matrix. Overall the versatility of

template-directed deposition of embedded nanostructures is expected to extend to include other, non-metallic material systems such as functional complex oxides, thus opening a wealth of opportunities to study transport, ferroic, and physiochemical phenomena sensitive to large electric fields.

CHAPTER 6

CONCLUSION AND OUTLOOK

Overall the work detailed in this thesis span topics ranging from fabrication processes to physical understanding of oxide-based resistive switching memory devices. All studies focused on identifying the underlying transport properties, controlling defect density and migration, and designing device fabrication methods that ultimately improve device performance to meet industrial requirements. The first study revealed the area dependency of electroforming and switching voltages in a TiO_2 based resistive switching cell, and reported on the different roles of oxygen vacancies on inducing a tunable polarity reversal during the switching process. Another series of work introduced an inexpensive fabrication approach that enables deposition of memristive nanoribbons comprising transition metal oxide nanoparticles that possess the ability to be transferred to arbitrary substrates, thus providing a rich parameter space. The latest study successfully demonstrated stark improvements to memristive functionality in HfO_2 thin films, including voltage reduction and enhanced parameter uniformity, by embedding nanoislands with pre-defined ordered, size and density.

Considering the potential of RRAM as a future high-density storage platform, new approaches must address remaining technological challenges such as device reliability, scaling for high density applications, and large-scale manufacturing. To overcome these challenges, studies of RRAM that pair materials engineering with structure and integration schemes have accelerated developments in performance, reliability and cost at an extraordinary pace. This chapter draws from the conclusions of the studies outlined above to identify future needs and directions in the field, including exciting

issues and the most promising solutions. The following sections will also highlight the most up-to-date characterization efforts that determine the shape, chemical properties and growth dynamics on conducting filaments.

6.1 Potential Works & Future Scope

In order for RRAM devices to break into commercial markets it is necessary to increase the reliability as well as leverage its scaling capability. Metal-oxide nanostructures are an essential building block in modern emerging memory technology and demonstrate significant promise as the functional switching material in RRAM devices. To achieve high performance device, it is important for the switching layer to possess uniform properties and a controllable conductive regime. Only devices with stable switching parameters can be effectively operated with optimal productivity. Based on the observation of subfilamentary networks via advanced SPM characterization techniques, an ideal uniformity should theoretically scale with the device size to the atomic level. This behavior has been well established recently yet demonstrated higher variability, as the degradation of reliability becomes a major issue in such small cells. While the evolutionary nature of the conductive filaments based on nanodevices has been revealed, characterization of the conducting component in a sub-nano structure still remains a rather difficult task, limiting the full knowledge of the switching mechanism and true scaling potential. Therefore, nanoscopic analyses involving advancements in materials engineering and characterization techniques will continue to play a key role in RRAM development.

6.1.1 Nanocrystals in Emerging Memristive Technology

Solution processing of a wide range of functional materials has been developed rapidly due to the potential to provide low-cost, large-area production and flexible electronics.[158] [159] Tremendous materials such as organic/polymer, organic-

inorganic nanocomposites, metal oxide nanocrystals and other nanostructures have been explored for this application. The STO and HfO_2 colloidal nanocrystals I used in my work served as an ordered switching layer assembly. This layer displays a porous structure with large interfacial area between neighboring nanocrystals, thus acting as a reservoir and a fast migration matrix of ions. The switching character of colloidal nanocrystals can be altered by the selection of the electrode materials. As described in Chapter 4, a reversed I-V response is observed when the Pt bottom electrode was replaced by Ag, suggesting that different switching mechanism is induced within the same material in contact with various metals. Until now, the most common approaches for depositing colloidal nanocrystals included spin coating, dip coating, and self-assembly. Drawbacks include the uniformity variations in film thickness from device to device induced from dip coating, and difficulties to obtain thin thickness by spin coating and dip coating. The convective self-assembly approach used here generates significant interest due to facile fabrication of scalable patterned nanostructures or continuous layers of colloidal nanocrystals. However, the transport mechanism at the tip/nanoribbon interface and between nanocrystals is not yet clear. While the nanocrystals attract attention because of their unique properties, it is important to address the reliability issues in such solution-processed RRAM devices.

The organic ligands between nanocrystals play a part in the assembly process, allowing a uniform film with order-distributed nanocrystals deposited on the substrate. It is important to note that the electrical behavior would be significant affected by the type, length and property of the organic ligands, which has received increased attention as the charge transport pathway.[83] [85] [160] High temperature annealing is required to remove the ligands and thus obtain a denser nanocrystal layer, changing the thickness of the film as well as enlarging the size of the nanocrystals. Further chemical analysis is also necessary to extensively investigate the transport mechanism.

6.1.2 Embedding Nanostructures

One attractive option to overcome the cycle-to-cycle variability in traditional RRAM devices is nanostructure-embedded devices, which have demonstrated substantial uniformity improvements in both set/reset and resistance. Consideration of the inherent scaling trend of memristive oxides implies better performance would also be found in smaller sizes. Ideally, perfectly uniform resistive switching is possible if only one conductive filament was formed and ruptured under a highly confined electrical filed. Due to the fact that the pore size and interpore spacing of AAO templates can be controlled (chemically and physically), it is worth to push forward the progress in fabrication of small pore size to catch up with the scaling potential. Additionally, the varying location of the embedded nanostructure may induce different effect on the set and reset processes, and thus there are ample opportunities to improve the performance.

6.1.3 Probing the Nanofilaments

The novelty of the 3D scalpel lies in the capability to completely observe the conductive channel. On one hand it provides an efficient way to remove the top electrode physically without introducing the unexpected chemical effects associated with other approaches such as ion milling. On the other hand it can overcome the challenges in providing experimental evidence of complex oxygen exchange due to the poor contrast between the reduced phase and the oxide matrix. The resolution of the image depends on the condition of the tip such as the geometry, resistance, spring constant and the tip-surface interaction, thus precise control is required during scanning. It is worth noting that c-AFM only offers the information in terms of the current contrast with high lateral resolution, permitting the realization of the location, shape and size of the filaments. However, the compositional identification of the filaments is still missing, limiting the understanding of ions activities involved

in switching behavior. Direct *in situ* characterization of the filament evolution is also not possible using this method. Combining 3D c-AFM and compositional analytical tools would provide a powerful, exciting platform to obtain the microscopic details from both the top surface of the device and inside the oxide layer.

APPENDIX A

MACROBUILDER

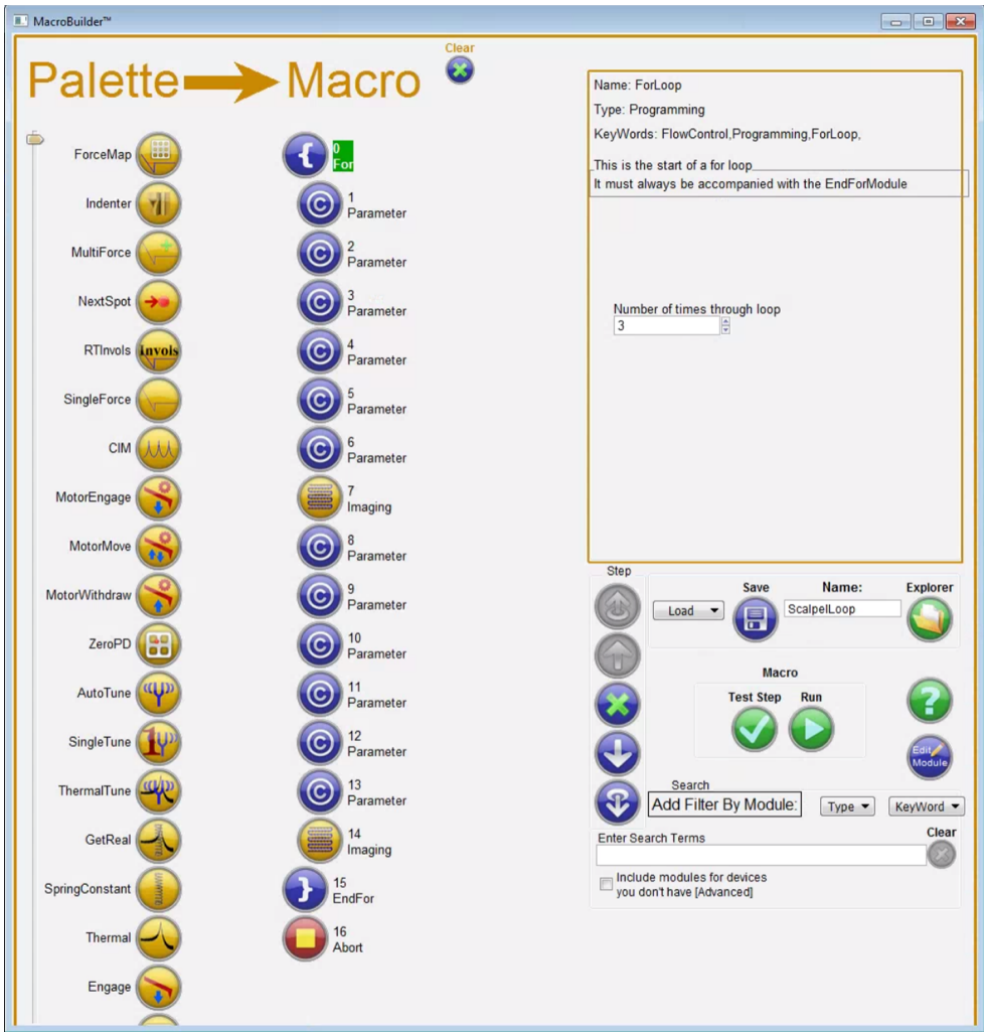

Figure A.1.

Loop(Imaging: Scan rate: 0.3 Hz, deflection setpoint volts: 1.5 V, scanlines: 512, scan point: 512; Imaging: scan rate: 2 Hz, deflection setpoint volts: 0.01V, scanlines: 256, scan point: 256, surface voltage: 500 mV.)

APPENDIX B

3D CONSTRUCTION USING IMAGEJ SOFTWARE

1. Create a folder with the 2D current images in sequence.

2. File → Import → Image Sequence, click the first file and open. In the Sequence Options window, use virtual stack.

3. Plugins → Volume Viewer

4. Adjust z-Aspect and Sampling to achieve appropriate structure.

BIBLIOGRAPHY

[1] L. Chua, "Memristor-the missing circuit element," *IEEE Transactions on Circuit Theory*, vol. 18, no. 5, pp. 507–519, 1971.

[2] S. Yu and P. Y. Chen, "Emerging memory technologies: Recent trends and prospects," *IEEE Solid-State Circuits Magazine*, vol. 8, no. 2, pp. 43–56, 2016.

[3] M. A. Zidan, J. P. Strachan, and W. D. Lu, "The future of electronics based on memristive systems," *Nature Electronics*, vol. 1, no. 1, pp. 22–29, 2018. [Online]. Available: https://doi.org/10.1038/s41928-017-0006-8

[4] R. Waser and M. Aono, "Nanoionics-based resistive switching memories," *Nat Mater*, vol. 6, no. 11, pp. 833–40, 2007. [Online]. Available: http://www.ncbi.nlm.nih.gov/pubmed/17972938

[5] A. Sawa, "Resistive switching in transition metal oxides," *Materials Today*, vol. 11, no. 6, pp. 28–36, 2008. [Online]. Available: http://www.sciencedirect.com/science/article/pii/S1369702108701196

[6] J. J. Yang, M. D. Pickett, X. Li, A. A. OhlbergDouglas, D. R. Stewart, and R. S. Williams, "Memristive switching mechanism for metal/oxide/metal nanodevices," *Nat Nano*, vol. 3, no. 7, pp. 429–433, 2008. [Online]. Available: http://dx.doi.org/10.1038/nnano.2008.160

[7] D.-H. Kwon, K. M. Kim, J. H. Jang, J. M. Jeon, M. H. Lee, G. H. Kim, X.-S. Li, G.-S. Park, B. Lee, S. Han, M. Kim, and C. S. Hwang, "Atomic structure of conducting nanofilaments in TiO_2 resistive switching memory," *Nat Nano*, vol. 5, no. 2, pp. 148–153, 2010. [Online]. Available: http://dx.doi.org/10.1038/nnano.2009.456

[8] M. Lanza, G. Bersuker, M. Porti, E. Miranda, M. Nafría, and X. Aymerich, "Resistive switching in hafnium dioxide layers: Local phenomenon at grain boundaries," *Applied Physics Letters*, vol. 101, no. 19, p. 193502, 2012. [Online]. Available: http://aip.scitation.org/doi/abs/10.1063/1.4765342

[9] M.-J. Lee, C. B. Lee, D. Lee, S. R. Lee, M. Chang, J. H. Hur, Y.-B. Kim, C.-J. Kim, D. H. Seo, S. Seo, U. I. Chung, I.-K. Yoo, and K. Kim, "A fast, high-endurance and scalable non-volatile memory device made from asymmetric bilayer Ta_2O_{5-x}/TaO_{2-x} structures," *Nat Mater*, vol. 10, no. 8, pp. 625–630, 2011. [Online]. Available: http://dx.doi.org/10.1038/nmat3070

[10] M. M. Shirolkar, C. Hao, X. Dong, T. Guo, L. Zhang, M. Li, and H. Wang, "Tunable multiferroic and bistable/complementary resistive switching properties of dilutely li-doped $BiFeO_3$ nanoparticles: an effect of aliovalent substitution," *Nanoscale*, vol. 6, no. 9, pp. 4735–4744, 2014. [Online]. Available: http://dx.doi.org/10.1039/C3NR05973A

[11] C. Li, Y. Vaynzof, G. Lakhwani, G. J. Beirne, J. Wang, and N. C. Greenham, "Observation of oxygen vacancy migration in memory devices based on zno nanoparticles," *Journal of Applied Physics*, vol. 121, no. 14, p. 144503, 2017. [Online]. Available: https://aip.scitation.org/doi/abs/10.1063/1.4979973

[12] C.-H. Huang, W.-C. Chang, J.-S. Huang, S.-M. Lin, and Y.-L. Chueh, "Resistive switching of sn-doped in_2o_3/HfO_2 core-shell nanowire: geometry architecture engineering for nonvolatile memory," *Nanoscale*, vol. 9, no. 20, pp. 6920–6928, 2017. [Online]. Available: http://dx.doi.org/10.1039/C6NR09564J

[13] S. K. Hwang, J. M. Lee, S. Kim, J. S. Park, H. I. Park, C. W. Ahn, K. J. Lee, T. Lee, and S. O. Kim, "Flexible multilevel resistive memory with controlled charge trap b- and n-doped carbon nanotubes," *Nano Letters*, vol. 12, no. 5, pp. 2217–2221, 2012. [Online]. Available: https://doi.org/10.1021/nl204039q

[14] D. Ielmini, C. Cagli, F. Nardi, and Y. Zhang, "Nanowire-based resistive switching memories: devices, operation and scaling," *Journal of Physics D: Applied Physics*, vol. 46, no. 7, p. 074006, 2013. [Online]. Available: http://stacks.iop.org/0022-3727/46/i=7/a=074006

[15] M. Kubicek, R. Schmitt, F. Messerschmitt, and J. L. M. Rupp, "Uncovering two competing switching mechanisms for epitaxial and ultrathin strontium titanate-based resistive switching bits," *ACS Nano*, vol. 9, no. 11, pp. 10 737–10 748, 2015. [Online]. Available: http://dx.doi.org/10.1021/acsnano.5b02752

[16] D. C. Kim, S. Seo, S. E. Ahn, D.-S. Suh, M. J. Lee, B.-H. Park, I. K. Yoo, I. G. Baek, H.-J. Kim, E. K. Yim, J. E. Lee, S. O. Park, H. S. Kim, U.-I. Chung, J. T. Moon, and B. I. Ryu, "Electrical observations of filamentary conductions for the resistive memory switching in nio films," *Applied Physics Letters*, vol. 88, no. 20, p. 202102, 2006. [Online]. Available: http://aip.scitation.org/doi/abs/10.1063/1.2204649

[17] J. Y. Son and Y.-H. Shin, "Direct observation of conducting filaments on resistive switching of nio thin films," *Applied Physics Letters*, vol. 92, no. 22, p. 222106, 2008. [Online]. Available: http://aip.scitation.org/doi/abs/10.1063/1.2931087

[18] D. S. Jeong, H. Schroeder, U. Breuer, and R. Waser, "Characteristic electroforming behavior in $Pt/TiO_2/Pt$ resistive switching cells depending on atmosphere," *Journal of Applied Physics*, vol. 104, no. 12, p. 123716, 2008. [Online]. Available: http://aip.scitation.org/doi/abs/10.1063/1.3043879

[19] S. Hyunjun, C. Dooho, L. Dongsoo, S. Sunae, L. Myong-Jae, Y. In-Kyeong, and H. Hyunsang, "Resistance-switching characteristics of polycrystalline Nb_2O_5 for nonvolatile memory application," *IEEE Electron Device Letters*, vol. 26, no. 5, pp. 292–294, 2005.

[20] Y. L. Chen, J. Wang, C. M. Xiong, R. F. Dou, J. Y. Yang, and J. C. Nie, "Scanning tunneling microscopy/spectroscopy studies of resistive switching in nb-doped $SrTiO_3$," *Journal of Applied Physics*, vol. 112, no. 2, p. 023703, 2012. [Online]. Available: http://aip.scitation.org/doi/abs/10.1063/1.4733999

[21] R. Dittmann, R. Muenstermann, I. Krug, D. Park, T. Menke, J. Mayer, A. Besmehn, F. Kronast, C. M. Schneider, and R. Waser, "Scaling potential of local redox processes in memristive SrTiO thin-film devices," *Proceedings of the IEEE*, vol. 100, no. 6, pp. 1979–1990, 2012.

[22] E. Linn, R. Rosezin, C. Kugeler, and R. Waser, "Complementary resistive switches for passive nanocrossbar memories," *Nat Mater*, vol. 9, no. 5, pp. 403–406, 2010. [Online]. Available: http://dx.doi.org/10.1038/nmat2748

[23] Y. Yang, P. Sheridan, and W. Lu, "Complementary resistive switching in tantalum oxide-based resistive memory devices," *Applied Physics Letters*, vol. 100, no. 20, p. 203112, 2012. [Online]. Available: https://aip.scitation.org/doi/abs/10.1063/1.4719198

[24] K. Shibuya, R. Dittmann, S. Mi, and R. Waser, "Impact of defect distribution on resistive switching characteristics of Sr_2TiO_4 thin films," *Advanced Materials*, vol. 22, no. 3, pp. 411–414, 2010. [Online]. Available: http://dx.doi.org/10.1002/adma.200901493

[25] S. Kim, S. Choi, and W. Lu, "Comprehensive physical model of dynamic resistive switching in an oxide memristor," *ACS Nano*, vol. 8, no. 3, pp. 2369–2376, 2014. [Online]. Available: http://dx.doi.org/10.1021/nn405827t

[26] Z. Wang, S. Joshi, S. E. Savel'ev, H. Jiang, R. Midya, P. Lin, M. Hu, N. Ge, J. P. Strachan, Z. Li, Q. Wu, M. Barnell, G.-L. Li, H. L. Xin, R. S. Williams, Q. Xia, and J. J. Yang, "Memristors with diffusive dynamics as synaptic emulators for neuromorphic computing," *Nat Mater*, vol. 16, no. 1, pp. 101–108, 2017. [Online]. Available: http://dx.doi.org/10.1038/nmat4756

[27] K. H. Jin, Y. K. Jean, P. T. Hyung, K. H. Joon, K. Y. Jae, S. X. Long, K. D. Eun, K. Y. Min, and H. C. Seong, "Filament shape dependent reset behavior governed by the interplay between the electric field and thermal effects in the $Pt/TiO_2/Cu$ electrochemical metallization device," *Advanced Electronic Materials*, vol. 3, no. 2, p. 1600404, 2017. [Online]. Available: https://onlinelibrary.wiley.com/doi/abs/10.1002/aelm.201600404

[28] Z. Wang, H. Jiang, M. Hyung Jang, P. Lin, A. Ribbe, Q. Xia, and J. J. Yang, "Electrochemical metallization switching with a platinum group metal in different oxides," *Nanoscale*, vol. 8, no. 29, pp. 14 023–14 030, 2016. [Online]. Available: http://dx.doi.org/10.1039/C6NR01085G

[29] J.-Y. Chen, C.-L. Hsin, C.-W. Huang, C.-H. Chiu, Y.-T. Huang, S.-J. Lin, W.-W. Wu, and L.-J. Chen, "Dynamic evolution of conducting nanofilament in resistive switching memories," *Nano Letters*, vol. 13, no. 8, pp. 3671–3677, 2013. [Online]. Available: http://dx.doi.org/10.1021/nl4015638

[30] U. Celano, L. Goux, A. Belmonte, K. Opsomer, A. Franquet, A. Schulze, C. Detavernier, O. Richard, H. Bender, M. Jurczak, and W. Vandervorst, "Three-dimensional observation of the conductive filament in nanoscaled resistive memory devices," *Nano Letters*, vol. 14, no. 5, pp. 2401–2406, 2014. [Online]. Available: http://dx.doi.org/10.1021/nl500049g

[31] S.-J. Choi, G.-S. Park, K.-H. Kim, S. Cho, W.-Y. Yang, X.-S. Li, J.-H. Moon, K.-J. Lee, and K. Kim, "In situ observation of voltage-induced multilevel resistive switching in solid electrolyte memory," *Advanced Materials*, vol. 23, no. 29, pp. 3272–3277, 2011. [Online]. Available: http://dx.doi.org/10.1002/adma.201100507

[32] K. J. Norris, J. J. Yang, and N. P. Kobayashi, "Tem and eels study on TaO_x-based nanoscale resistive switching devices," *MRS Proceedings*, vol. 1805, 2015. [Online]. Available: https://www.cambridge.org/core/article/div-class-title-tem-and-eels-study-on-tao-span-class-sub-x-span-based-nanoscale-resistive-sw 5E284ACAEDA6871BEF2683CD71D5E585

[33] R. Muenstermann, T. Menke, R. Dittmann, and R. Waser, "Coexistence of filamentary and homogeneous resistive switching in Fe-doped $SrTiO_3$ thin-film memristive devices," *Advanced Materials*, vol. 22, no. 43, pp. 4819–4822, 2010. [Online]. Available: http://dx.doi.org/10.1002/adma.201001872

[34] R. Münstermann, J. J. Yang, J. P. Strachan, G. Medeiros-Ribeiro, R. Dittmann, and R. Waser, "Morphological and electrical changes in TiO_2 memristive devices induced by electroforming and switching," *physica status solidi (RRL) – Rapid Research Letters*, vol. 4, no. 1-2, pp. 16–18, 2010. [Online]. Available: http://dx.doi.org/10.1002/pssr.200903347

[35] J. Xiao, W. L. Ong, Z. Guo, G. W. Ho, and K. Zeng, "Resistive switching and polarization reversal of hydrothermal-method-grown undoped zinc oxide nanorods by using scanning probe microscopy techniques," *ACS Applied Materials & Interfaces*, vol. 7, no. 21, pp. 11 412–11 422, 2015. [Online]. Available: http://dx.doi.org/10.1021/acsami.5b01988

[36] C. Baeumer, C. Schmitz, A. H. H. Ramadan, H. Du, K. Skaja, V. Feyer, P. Müller, B. Arndt, C.-L. Jia, J. Mayer, R. A. De Souza, C. Michael Schneider, R. Waser, and R. Dittmann, "Spectromicroscopic insights for rational design of redox-based memristive devices," *Nature Communications*, vol. 6, p. 8610, 2015. [Online]. Available: http://dx.doi.org/10.1038/ncomms9610

[37] S. Tappertzhofen, I. Valov, T. Tsuruoka, T. Hasegawa, R. Waser, and M. Aono, "Generic relevance of counter charges for cation-based nanoscale resistive switching memories," *ACS Nano*, vol. 7, no. 7, pp. 6396–6402, 2013. [Online]. Available: http://dx.doi.org/10.1021/nn4026614

[38] M. H. Lee and C. S. Hwang, "Resistive switching memory: observations with scanning probe microscopy," *Nanoscale*, vol. 3, no. 2, pp. 490–502, 2011. [Online]. Available: http://dx.doi.org/10.1039/C0NR00580K

[39] M. H. Lee, S. J. Song, K. M. Kim, G. H. Kim, J. Y. Seok, J. H. Yoon, and C. S. Hwang, "Scanning probe based observation of bipolar resistive switching nio films," *Applied Physics Letters*, vol. 97, no. 6, p. 062909, 2010. [Online]. Available: http://aip.scitation.org/doi/abs/10.1063/1.3479526

[40] H. Lee, H. Kim, T. N. Van, D.-W. Kim, and J. Y. Park, "Nanoscale resistive switching schottky contacts on self-assembled Pt nanodots on $SrTiO_3$," *ACS Applied Materials & Interfaces*, vol. 5, no. 22, pp. 11 668–11 672, 2013. [Online]. Available: http://pubs.acs.org/doi/abs/10.1021/am4032086

[41] L. Yang, C. Kuegeler, K. Szot, A. Ruediger, and R. Waser, "The influence of copper top electrodes on the resistive switching effect in TiO_2 thin films studied by conductive atomic force microscopy," *Applied Physics Letters*, vol. 95, no. 1, p. 013109, 2009. [Online]. Available: http://aip.scitation.org/doi/abs/10.1063/1.3167810

[42] H. Jiechang, R. Baptiste, Q. Wei, S. N. Stephen, and A. B. Dawn, "Tip loading effects on afm-based transport measurements of metal–oxide interfaces," *Nanotechnology*, vol. 24, no. 39, p. 395703, 2013. [Online]. Available: http://stacks.iop.org/0957-4484/24/i=39/a=395703

[43] M. Lanza, K. Zhang, M. Porti, M. Nafría, Z. Y. Shen, L. F. Liu, J. F. Kang, D. Gilmer, and G. Bersuker, "Grain boundaries as preferential sites for resistive switching in the HfO_2 resistive random access memory structures," *Applied Physics Letters*, vol. 100, no. 12, p. 123508, 2012. [Online]. Available: http://aip.scitation.org/doi/abs/10.1063/1.3697648

[44] M. Lanza, U. Celano, and F. Miao, "Nanoscale characterization of resistive switching using advanced conductive atomic force microscopy based setups," *Journal of Electroceramics*, 2017. [Online]. Available: https://doi.org/10.1007/s10832-017-0082-1

[45] D. S. Jeong, H. Schroeder, and R. Waser, "Coexistence of bipolar and unipolar resistive switching behaviors in a Pt/TiO_2/Pt stack," *Electrochemical and Solid-State Letters*, vol. 10, no. 8, pp. G51–G53, 2007. [Online]. Available: http://esl.ecsdl.org/content/10/8/G51.abstract

[46] J. J. Yang, M. Feng, D. P. Matthew, A. A. O. Douglas, R. S. Duncan, L. Chun Ning, and R. S. Williams, "The mechanism of electroforming of metal oxide memristive switches," *Nanotechnology*, vol. 20, no. 21, p. 215201, 2009. [Online]. Available: http://stacks.iop.org/0957-4484/20/i=21/a=215201

[47] U. Celano, L. Goux, R. Degraeve, A. Fantini, O. Richard, H. Bender, M. Jurczak, and W. Vandervorst, "Imaging the three-dimensional conductive channel in filamentary-based oxide resistive switching memory," *Nano Letters*, vol. 15, no. 12, pp. 7970–7975, 2015. [Online]. Available: http://dx.doi.org/10.1021/acs.nanolett.5b03078

[48] W. Melitz, J. Shen, A. C. Kummel, and S. Lee, "Kelvin probe force microscopy and its application," *Surface Science Reports*, vol. 66, no. 1, pp. 1–27, 2011. [Online]. Available: http://www.sciencedirect.com/science/article/pii/S0167572910000841

[49] U. Russo, D. Ielmini, C. Cagli, and A. L. Lacaita, "Self-accelerated thermal dissolution model for reset programming in unipolar resistive-switching memory (rram) devices," *IEEE Transactions on Electron Devices*, vol. 56, no. 2, pp. 193–200, 2009.

[50] L. Goux, J. G. Lisoni, M. Jurczak, D. J. Wouters, L. Courtade, and C. Muller, "Coexistence of the bipolar and unipolar resistive-switching modes in nio cells made by thermal oxidation of ni layers," *Journal of Applied Physics*, vol. 107, no. 2, p. 024512, 2010. [Online]. Available: http://aip.scitation.org/doi/abs/10.1063/1.3275426

[51] Y. Shi, Y. Ji, F. Hui, M. Nafria, M. Porti, G. Bersuker, and M. Lanza, "New insights on the origin of resistive switching in HfO_2 thin films: The role of local mechanical strength," in *2015 IEEE 22nd International Symposium on the Physical and Failure Analysis of Integrated Circuits*, Conference Proceedings, pp. 472–475.

[52] I. Valov, I. Sapezanskaia, A. Nayak, T. Tsuruoka, T. Bredow, T. Hasegawa, G. Staikov, M. Aono, and R. Waser, "Atomically controlled electrochemical nucleation at superionic solid electrolyte surfaces," *Nat Mater*, vol. 11, no. 6, pp. 530–535, 2012. [Online]. Available: http://dx.doi.org/10.1038/nmat3307

[53] A. Wedig, M. Luebben, D.-Y. Cho, M. Moors, K. Skaja, V. Rana, T. Hasegawa, K. K. Adepalli, B. Yildiz, R. Waser, and I. Valov, "Nanoscale cation motion in taox, HfO_x and TiO_x memristive systems," *Nat Nano*, vol. 11, no. 1, pp. 67–74, 2016. [Online]. Available: http://dx.doi.org/10.1038/nnano.2015.221

[54] H. Jiang, L. Han, P. Lin, Z. Wang, M. H. Jang, Q. Wu, M. Barnell, J. J. Yang, H. L. Xin, and Q. Xia, "Sub-10 nm ta channel responsible for superior performance of a HfO_2 memristor," *Scientific Reports*, vol. 6, p. 28525, 2016. [Online]. Available: http://dx.doi.org/10.1038/srep28525

[55] M. Lübben, P. Karakolis, V. Ioannou-Sougleridis, P. Normand, P. Dimitrakis, and I. Valov, "Graphene-modified interface controls transition from vcm to ecm switching modes in ta/taox based memristive devices," *Advanced Materials*, vol. 27, no. 40, pp. 6202–6207, 2015. [Online]. Available: http://dx.doi.org/10.1002/adma.201502574

[56] A. A. Sharma, M. Noman, M. Abdelmoula, M. Skowronski, and J. A. Bain, "Electronic instabilities leading to electroformation of binary metal oxide-based resistive switches," *Advanced Functional Materials*, vol. 24, no. 35, pp. 5522–5529, 2014. [Online]. Available: http://dx.doi.org/10.1002/adfm.201400461

[57] S. Kumar, C. E. Graves, J. P. Strachan, E. M. Grafals, A. L. D. Kilcoyne, T. Tyliszczak, J. N. Weker, Y. Nishi, and R. S. Williams, "Direct observation of localized radial oxygen migration in functioning tantalum oxide memristors," *Advanced Materials*, vol. 28, no. 14, pp. 2772–2776, 2016. [Online]. Available: http://dx.doi.org/10.1002/adma.201505435

[58] C. Nauenheim, C. Kuegeler, A. Ruediger, and R. Waser, "Investigation of the electroforming process in resistively switching TiO_2 nanocrosspoint junctions," *Applied Physics Letters*, vol. 96, no. 12, p. 122902, 2010. [Online]. Available: http://scitation.aip.org/content/aip/journal/apl/96/12/10.1063/1.3367752

[59] A. A. Sharma, I. V. Karpov, R. Kotlyar, J. Kwon, M. Skowronski, and J. A. Bain, "Dynamics of electroforming in binary metal oxide-based resistive switching memory," *Journal of Applied Physics*, vol. 118, no. 11, p. 114903, 2015. [Online]. Available: http://scitation.aip.org/content/aip/journal/jap/118/11/10.1063/1.4930051

[60] D. K. Gala, A. A. Sharma, D. Li, J. M. Goodwill, J. A. Bain, and M. Skowronski, "Low temperature electroformation of taox-based resistive switching devices," *APL Mater.*, vol. 4, no. 1, p. 016101, 2016. [Online]. Available: http://scitation.aip.org/content/aip/journal/aplmater/4/1/10.1063/1.4939181

[61] A. Chen, "Area and thickness scaling of forming voltage of resistive switching memories," *IEEE Electron Device Letters*, vol. 35, no. 1, pp. 57–59, 2014.

[62] B. Govoreanu, G. S. Kar, Y. Y. Chen, V. Paraschiv, S. Kubicek, A. Fantini, I. P. Radu, L. Goux, S. Clima, R. Degraeve, N. Jossart, O. Richard, T. Vandeweyer, K. Seo, P. Hendrickx, G. Pourtois, H. Bender, L. Altimime, D. J. Wouters, J. A. Kittl, and M. Jurczak, "10nm Hf/HfO_x crossbar resistive ram with excellent performance, reliability and low-energy operation," in *Electron Devices Meeting (IEDM), 2011 IEEE International*, Conference Proceedings, pp. 31.6.1–31.6.4.

[63] H. Wylezich, H. Mähne, J. Rensberg, C. Ronning, P. Zahn, S. Slesazeck, and T. Mikolajick, "Local ion irradiation-induced resistive threshold and memory switching in Nb_2O_5/NbO_x films," *ACS Applied Materials & Interfaces*, vol. 6, no. 20, pp. 17 474–17 480, 2014. [Online]. Available: http://dx.doi.org/10.1021/am5021149

[64] P. Bousoulas, I. Michelakaki, and D. Tsoukalas, "Influence of oxygen content of room temperature TiO_{2-x} deposited films for enhanced resistive switching memory performance," *Journal of Applied Physics*, vol. 115, no. 3, p. 034516, 2014. [Online]. Available: http://scitation.aip.org/content/aip/journal/jap/115/3/10.1063/1.4862797

[65] N. Ghenzi, M. J. Rozenberg, R. Llopis, P. Levy, L. E. Hueso, and P. Stoliar, "Tuning the resistive switching properties of TiO_{2-x} films," *Applied Physics Letters*, vol. 106, no. 12, p. 123509, 2015. [Online]. Available: http://scitation.aip.org/content/aip/journal/apl/106/12/10.1063/1.4916516

[66] J. S. Lee, S. Lee, and T. W. Noh, "Resistive switching phenomena: A review of statistical physics approaches," *Applied Physics Reviews*, vol. 2, no. 3, p. 031303, 2015. [Online]. Available: http://scitation.aip.org/content/aip/journal/apr2/2/3/10.1063/1.4929512

[67] J. Hou, S. S. Nonnenmann, W. Qin, and D. A. Bonnell, "Size dependence of resistive switching at nanoscale metal-oxide interfaces," *Advanced Functional Materials*, vol. 24, no. 26, pp. 4113–4118, 2014. [Online]. Available: http://dx.doi.org/10.1002/adfm.201304121

[68] D. Ielmini, F. Nardi, and C. Cagli, "Physical models of size-dependent nanofilament formation and rupture in nio resistive switching memories," *Nanotechnology*, vol. 22, no. 25, p. 254022, 2011. [Online]. Available: http://stacks.iop.org/0957-4484/22/i=25/a=254022

[69] K. Kyung Min, J. Doo Seok, and H. Cheol Seong, "Nanofilamentary resistive switching in binary oxide system; a review on the present status and outlook," *Nanotechnology*, vol. 22, no. 25, p. 254002, 2011. [Online]. Available: http://stacks.iop.org/0957-4484/22/i=25/a=254002

[70] K. Szot, M. Rogala, W. Speier, Z. Klusek, A. Besmehn, and R. Waser, "TiO_2 —a prototypical memristive material," *Nanotechnology*, vol. 22, no. 25, p. 254001, 2011. [Online]. Available: http://stacks.iop.org/0957-4484/22/i=25/a=254001

[71] M. Feng, J. J. Yang, B. Julien, M.-R. Gilberto, and R. S. Williams, "Observation of two resistance switching modes in TiO_2 memristive devices electroformed at low current," *Nanotechnology*, vol. 22, no. 25, p. 254007, 2011. [Online]. Available: http://stacks.iop.org/0957-4484/22/i=25/a=254007

[72] A. Sawa, T. Fujii, M. Kawasaki, and Y. Tokura, "Hysteretic current–voltage characteristics and resistance switching at a rectifying $Ti/Pr_{0.7}Ca_{0.3}MnO_3$ interface," *Applied Physics Letters*, vol. 85, no. 18, pp. 4073–4075, 2004. [Online]. Available: http://scitation.aip.org/content/aip/journal/apl/85/18/10.1063/1.1812580

[73] J. J. Yang, J. Borghetti, D. Murphy, D. R. Stewart, and R. S. Williams, "A family of electronically reconfigurable nanodevices," *Advanced Materials*, vol. 21, no. 37, pp. 3754–3758, 2009. [Online]. Available: http://dx.doi.org/10.1002/adma.200900822

[74] A. Khiat, P. Ayliffe, and T. Prodromakis, *Scientific Reports*, vol. 6, p. 32614, 2016. [Online]. Available: http://www.ncbi.nlm.nih.gov/pmc/articles/PMC5009344/

[75] R. Waser, R. Dittmann, G. Staikov, and K. Szot, "Redox-based resistive switching memories – nanoionic mechanisms, prospects, and challenges," *Advanced Materials*, vol. 21, no. 25-26, pp. 2632–2663, 2009. [Online]. Available: http://dx.doi.org/10.1002/adma.200900375

[76] I. Valov, "Redox-based resistive switching memories (rerams): Electrochemical systems at the atomic scale," *ChemElectroChem*, vol. 1, no. 1, pp. 26–36, 2014. [Online]. Available: http://dx.doi.org/10.1002/celc.201300165

[77] T.-C. Chang, K.-C. Chang, T.-M. Tsai, T.-J. Chu, and S. M. Sze, "Resistance random access memory," *Materials Today*, vol. 19, no. 5, pp. 254–264, 2016. [Online]. Available: //www.sciencedirect.com/science/article/pii/S1369702115003843

[78] D. O. Schmidt, S. Hoffmann-Eifert, H. Zhang, C. La Torre, A. Besmehn, M. Noyong, R. Waser, and U. Simon, "Resistive switching of individual, chemically synthesized TiO_2 nanoparticles," *Small*, vol. 11, no. 48, pp. 6444–6456, 2015. [Online]. Available: http://dx.doi.org/10.1002/smll.201502100

[79] K. Nagashima, T. Yanagida, K. Oka, M. Taniguchi, T. Kawai, J.-S. Kim, and B. H. Park, "Resistive switching multistate nonvolatile memory effects in a single cobalt oxide nanowire," *Nano Letters*, vol. 10, no. 4, pp. 1359–1363, 2010. [Online]. Available: http://dx.doi.org/10.1021/nl9042906

[80] E. M. Bourim, Y. Kim, and D.-W. Kim, "Interface state effects on resistive switching behaviors of Pt/nb-doped $SrTiO_3$ single-crystal schottky junctions," *ECS Journal of Solid State Science and Technology*, vol. 3, no. 7, pp. N95–N101, 2014. [Online]. Available: http://jss.ecsdl.org/content/3/7/N95.abstract

[81] O. A. Ageev, Y. F. Blinov, O. I. Il'in, B. G. Konoplev, M. V. Rubashkina, V. A. Smirnov, and A. A. Fedotov, "Study of the resistive switching of vertically aligned carbon nanotubes by scanning tunneling microscopy," *Physics of the Solid State*, vol. 57, no. 4, pp. 825–831, 2015. [Online]. Available: http://dx.doi.org/10.1134/S1063783415040034

[82] S. S. Nonnenmann, E. M. Gallo, and J. E. Spanier, "Redox-based resistive switching in ferroelectric perovskite nanotubes," *Applied Physics Letters*, vol. 97, no. 10, p. 102904, 2010. [Online]. Available: http://scitation.aip.org/content/aip/journal/apl/97/10/10.1063/1.3486224

[83] O. Voznyy, B. R. Sutherland, A. H. Ip, D. Zhitomirsky, and E. H. Sargent, "Engineering charge transport by heterostructuring solution-processed semiconductors," *Nature Reviews Materials*, vol. 2, p. 17026, 2017. [Online]. Available: http://dx.doi.org/10.1038/natrevmats.2017.26

[84] G. Niu, L. Wang, R. Gao, B. Ma, H. Dong, and Y. Qiu, "Inorganic iodide ligands in ex situ pbs quantum dot sensitized solar cells with i-/i3-electrolytes," *Journal of Materials Chemistry*, vol. 22, no. 33, pp. 16 914–16 919, 2012. [Online]. Available: http://dx.doi.org/10.1039/C2JM32459H

[85] Y. Liu, M. Gibbs, J. Puthussery, S. Gaik, R. Ihly, H. W. Hillhouse, and M. Law, "Dependence of carrier mobility on nanocrystal size and ligand length in pbse nanocrystal solids," *Nano Letters*, vol. 10, no. 5, pp. 1960–1969, 2010. [Online]. Available: http://dx.doi.org/10.1021/nl101284k

[86] X. Yu, N. Malvankar, R. Landis, S. Eymur, O. R. Miranda, and V. M. Rotello, "Impedance spectroscopy of ionic ligand-modulated charge transport of gold nanoparticle films," *Small*, vol. 11, no. 31, pp. 3814–3821, 2015. [Online]. Available: http://dx.doi.org/10.1002/smll.201500127

[87] J. Jang, F. Pan, K. Braam, and V. Subramanian, "Resistance switching characteristics of solid electrolyte chalcogenide Ag_2Se nanoparticles for flexible nonvolatile memory applications," *Advanced Materials*, vol. 24, no. 26, pp. 3573–3576, 2012. [Online]. Available: http://dx.doi.org/10.1002/adma.201200671

[88] Q. Hu, T. S. Lee, N. J. Lee, T. S. Kang, M. R. Park, T.-S. Yoon, H. H. Lee, and C. J. Kang, "Resistive switching characteristics in mno nanoparticle assembly and Ag_2Se thin film devices," *Journal of Nanoscience and Nanotechnology*, vol. 17, no. 10, pp. 7189–7193, 2017. [Online]. Available: http://www.ingentaconnect.com/content/asp/jnn/2017/00000017/00000010/art00022https://doi.org/10.1166/jnn.2017.14732

[89] F. Verbakel, S. C. J. Meskers, D. M. de Leeuw, and R. A. J. Janssen, "Resistive switching in organic memories with a spin-coated metal oxide nanoparticle layer," *The Journal of Physical Chemistry C*, vol. 112, no. 14, pp. 5254–5257, 2008. [Online]. Available: http://dx.doi.org/10.1021/jp800624u

[90] M. M. Shirolkar, J. Li, X. Dong, M. Li, and H. Wang, "Controlling the ferroelectric and resistive switching properties of a $BiFeO_3$ thin film prepared using sub-5 nm dimension nanoparticles," *Physical Chemistry Chemical Physics*, vol. 19, no. 38, pp. 26 085–26 097, 2017. [Online]. Available: http://dx.doi.org/10.1039/C7CP04341D

[91] H. Quanli, J. Sung Mok, L. Hyun Ho, K. Yong-Sang, C. Young Jin, K. Dae-Hwan, K. Ki-Bum, and Y. Tae-Sik, "Resistive switching characteristics of maghemite nanoparticle assembly," *Journal of Physics D: Applied Physics*, vol. 44, no. 8, p. 085403, 2011. [Online]. Available: http://stacks.iop.org/0022-3727/44/i=8/a=085403

[92] Y. Jae Woo, H. Quanli, B. Yoon-Jae, C. Young Jin, K. Chi Jung, L. Hyun Ho, L. Do-Joong, K. Hyun-Mi, K. Ki-Bum, and Y. Tae-Sik, "Resistive switching characteristics of maghemite nanoparticle assembly on Al and Pt electrodes on a flexible substrate," *Journal of Physics D: Applied Physics*, vol. 45, no. 22, p. 225304, 2012. [Online]. Available: http://stacks.iop.org/0022-3727/45/i=22/a=225304

[93] J.-D. Kim, Y.-J. Baek, Y. J. Choi, C. J. Kang, H. H. Lee, H.-M. Kim, K.-B. Kim, and T.-S. Yoon, "Investigation of analog memristive switching of iron oxide nanoparticle assembly between Pt electrodes," *Journal of Applied Physics*, vol. 114, no. 22, p. 224505, 2013. [Online]. Available: http://aip.scitation.org/doi/abs/10.1063/1.4846759

[94] T. H. Kim, E. Y. Jang, N. J. Lee, D. J. Choi, K.-J. Lee, J.-t. Jang, J.-s. Choi, S. H. Moon, and J. Cheon, "Nanoparticle assemblies as memristors," *Nano Letters*, vol. 9, no. 6, pp. 2229–2233, 2009. [Online]. Available: http://dx.doi.org/10.1021/nl900030n

[95] E. Verrelli, D. Tsoukalas, P. Normand, A. H. Kean, and N. Boukos, "Forming-free resistive switching memories based on titanium-oxide nanoparticles fabricated at room temperature," *Applied Physics Letters*, vol. 102, no. 2, p. 022909, 2013. [Online]. Available: http://aip.scitation.org/doi/abs/10.1063/1.4775760

[96] J. Wang, S. Choudhary, W. L. Harrigan, A. J. Crosby, K. R. Kittilstved, and S. S. Nonnenmann, "Transferable memristive nanoribbons comprising solution-processed strontium titanate nanocubes," *ACS Applied Materials & Interfaces*, vol. 9, no. 12, pp. 10 847–10 854, 2017. [Online]. Available: http://dx.doi.org/10.1021/acsami.7b00220

[97] H. S. P. Wong, H. Y. Lee, S. Yu, Y. S. Chen, Y. Wu, P. S. Chen, B. Lee, F. T. Chen, and M. J. Tsai, "Metal 2013;oxide rram," *Proceedings of the IEEE*, vol. 100, no. 6, pp. 1951–1970, 2012.

[98] H. S. Kim, C. H. Lee, P. K. Sudeep, T. Emrick, and A. J. Crosby, "Nanoparticle stripes, grids, and ribbons produced by flow coating," *Advanced Materials*, vol. 22, no. 41, pp. 4600–4604, 2010. [Online]. Available: http://dx.doi.org/10.1002/adma.201001892

[99] H. Y. Peng, Y. F. Li, W. N. Lin, Y. Z. Wang, X. Y. Gao, and T. Wu, "Deterministic conversion between memory and threshold resistive switching via tuning the strong electron correlation," *Scientific Reports*, vol. 2, p. 442, 2012. [Online]. Available: http://www.ncbi.nlm.nih.gov/pmc/articles/PMC3369197/

[100] J. De Roo, F. Van den Broeck, K. De Keukeleere, J. C. Martins, I. Van Driessche, and Z. Hens, "Unravelling the surface chemistry of metal oxide nanocrystals, the role of acids and bases," *Journal of the American Chemical Society*, vol. 136, no. 27, pp. 9650–9657, 2014. [Online]. Available: http://dx.doi.org/10.1021/ja5032979

[101] J. De Roo, I. Van Driessche, J. C. Martins, and Z. Hens, "Colloidal metal oxide nanocrystal catalysis by sustained chemically driven ligand displacement," *Nat Mater*, vol. 15, no. 5, pp. 517–521, 2016. [Online]. Available: http://dx.doi.org/10.1038/nmat4554

[102] J. J. Yang, D. B. Strukov, and D. R. Stewart, "Memristive devices for computing," *Nat Nano*, vol. 8, no. 1, pp. 13–24, 2013. [Online]. Available: http://dx.doi.org/10.1038/nnano.2012.240

[103] K. Szot, R. Dittmann, W. Speier, and R. Waser, "Nanoscale resistive switching in $SrTiO_3$ thin films," *physica status solidi (RRL) – Rapid Research Letters*, vol. 1, no. 2, pp. R86–R88, 2007. [Online]. Available: http://dx.doi.org/10.1002/pssr.200701003http://onlinelibrary.wiley.com/store/10.1002/pssr.200701003/asset/86_ftp.pdf?v=1&t=itg3qyuz&s=013e2a1c68410ce6130410d06035592c269d31c9

[104] V. Metlenko, A. H. H. Ramadan, F. Gunkel, H. Du, H. Schraknepper, S. Hoffmann-Eifert, R. Dittmann, R. Waser, and R. A. De Souza, "Do dislocations act as atomic autobahns for oxygen in the perovskite oxide $SrTiO_3$?" *Nanoscale*, vol. 6, no. 21, pp. 12 864–12 876, 2014. [Online]. Available: http://dx.doi.org/10.1039/C4NR04083J

[105] D. Marrocchelli, L. Sun, and B. Yildiz, "Dislocations in $SrTiO_3$: Easy to reduce but not so fast for oxygen transport," *Journal of the American Chemical Society*, vol. 137, no. 14, pp. 4735–4748, 2015. [Online]. Available: http://dx.doi.org/10.1021/ja513176u

[106] K. Szot, W. Speier, G. Bihlmayer, and R. Waser, "Switching the electrical resistance of individual dislocations in single-crystalline $SrTiO_3$," *Nat Mater*, vol. 5, no. 4, pp. 312–320, 2006. [Online]. Available: http://dx.doi.org/10.1038/nmat1614

[107] R. Muenstermann, R. Dittmann, K. Szot, S. Mi, C.-L. Jia, P. Meuffels, and R. Waser, "Realization of regular arrays of nanoscale resistive switching blocks in thin films of nb-doped $SrTiO_3$," *Applied Physics Letters*, vol. 93, no. 2, p. 023110, 2008. [Online]. Available: http://scitation.aip.org/content/aip/journal/apl/93/2/10.1063/1.2959074

[108] T. Menke, P. Meuffels, R. Dittmann, K. Szot, and R. Waser, "Separation of bulk and interface contributions to electroforming and resistive switching behavior of epitaxial Fe-doped $SrTiO_3$," *Journal of Applied Physics*, vol. 105, no. 6, p. 066104, 2009. [Online]. Available: http://scitation.aip.org/content/aip/journal/jap/105/6/10.1063/1.3100209

[109] W. L. Harrigan, S. E. Michaud, K. A. Lehuta, and K. R. Kittilstved, "Tunable electronic structure and surface defects in chromium-doped colloidal $SrTiO_{3-\delta}$ nanocrystals," *Chemistry of Materials*, vol. 28, no. 2, pp. 430–433, 2016. [Online]. Available: http://dx.doi.org/10.1021/acs.chemmater.6b00049

[110] T. Gu, "Role of oxygen vacancies in TiO_2-based resistive switches," *Journal of Applied Physics*, vol. 113, no. 3, p. 033707, 2013. [Online]. Available: http://scitation.aip.org/content/aip/journal/jap/113/3/10.1063/1.4779767

[111] K. Kamiya, M. Young Yang, S.-G. Park, B. Magyari-Köpe, Y. Nishi, M. Niwa, and K. Shiraishi, "On-off switching mechanism of resistive–random–access–memories based on the formation and disruption of oxygen vacancy conducting channels," *Applied Physics Letters*, vol. 100, no. 7, p. 073502, 2012. [Online]. Available: http://scitation.aip.org/content/aip/journal/apl/100/7/10.1063/1.3685222

[112] S. X. Wu, L. M. Xu, X. J. Xing, S. M. Chen, Y. B. Yuan, Y. J. Liu, Y. P. Yu, X. Y. Li, and S. W. Li, "Reverse-bias-induced bipolar resistance switching in $Pt/TiO_2SrTi_{0.99}Nb_{0.01}O_3/Pt$ devices," *Applied Physics Letters*, vol. 93, no. 4, p. 043502, 2008. [Online]. Available: http://scitation.aip.org/content/aip/journal/apl/93/4/10.1063/1.2965469

[113] T. Fujii, M. Kawasaki, A. Sawa, Y. Kawazoe, H. Akoh, and Y. Tokura, "Electrical properties and colossal electroresistance of heteroepitaxial $SrRuO_3/SrTi_{1-x}Nb_xO_3$ schottky junctions," *Physical Review B*, vol. 75, no. 16, p. 165101, 2007. [Online]. Available: http://link.aps.org/doi/10.1103/PhysRevB.75.165101

[114] E. Mikheev, B. D. Hoskins, D. B. Strukov, and S. Stemmer, "Resistive switching and its suppression in Pt/nb:$SrTiO_3$ junctions," *Nat Commun*, vol. 5, 2014. [Online]. Available: http://dx.doi.org/10.1038/ncomms4990

[115] K.-J. Lee, L.-W. Wang, T.-K. Chiang, and Y.-H. Wang, "Effects of electrodes on the switching behavior of strontium titanate nickelate resistive random access memory," *Materials*, vol. 8, no. 10, p. 5374, 2015. [Online]. Available: http://www.mdpi.com/1996-1944/8/10/5374

[116] D. Y. Lee, J. T. Pham, J. Lawrence, C. H. Lee, C. Parkos, T. Emrick, and A. J. Crosby, "Macroscopic nanoparticle ribbons and fabrics," *Advanced Materials*, vol. 25, no. 9, pp. 1248–1253, 2013. [Online]. Available: http://dx.doi.org/10.1002/adma.201203719

[117] Y. Yang, P. Gao, S. Gaba, T. Chang, X. Pan, and W. Lu, "Observation of conducting filament growth in nanoscale resistive memories," *Nat Commun*, vol. 3, p. 732, 2012. [Online]. Available: http://dx.doi.org/10.1038/ncomms1737

[118] S. Yu, X. Guan, and H.-S. P. Wong, "Conduction mechanism of tin/HfO_x/Pt resistive switching memory: A trap-assisted-tunneling model," *Applied Physics Letters*, vol. 99, no. 6, p. 063507, 2011. [Online]. Available: http://aip.scitation.org/doi/abs/10.1063/1.3624472

[119] U. Celano, Y. Y. Chen, D. J. Wouters, G. Groeseneken, M. Jurczak, and W. Vandervorst, "Filament observation in metal-oxide resistive switching devices," *Applied Physics Letters*, vol. 102, no. 12, p. 121602, 2013. [Online]. Available: http://aip.scitation.org/doi/abs/10.1063/1.4798525

[120] M. A. Boles, D. Ling, T. Hyeon, and D. V. Talapin, "The surface science of nanocrystals," *Nat Mater*, vol. 15, no. 2, pp. 141–153, 2016. [Online]. Available: http://dx.doi.org/10.1038/nmat4526

[121] D. M. Adams, L. Brus, C. E. D. Chidsey, S. Creager, C. Creutz, C. R. Kagan, P. V. Kamat, M. Lieberman, S. Lindsay, R. A. Marcus, R. M. Metzger, M. E. Michel-Beyerle, J. R. Miller, M. D. Newton, D. R. Rolison, O. Sankey, K. S. Schanze, J. Yardley, and X. Zhu, "Charge transfer on the nanoscale: Current status," *The Journal of Physical Chemistry B*, vol. 107, no. 28, pp. 6668–6697, 2003. [Online]. Available: http://dx.doi.org/10.1021/jp0268462

[122] S. Xavier, M. Enrique, J. David, L. Shibing, L. Ming, R. Joan Marc, C. Francesca, and S. Jordi, "Threshold switching and conductance quantization in Al/HfO_2 /si(p) structures," *Japanese Journal of Applied Physics*, vol. 52, no. 4S, p. 04CD06, 2013. [Online]. Available: http://stacks.iop.org/1347-4065/52/i=4S/a=04CD06

[123] S. U. Sharath, S. Vogel, L. Molina-Luna, E. Hildebrandt, C. Wenger, J. Kurian, M. Duerrschnabel, T. Niermann, G. Niu, P. Calka, M. Lehmann, H.-J. Kleebe, T. Schroeder, and L. Alff, "Control of switching modes and conductance quantization in oxygen engineered HfO_x based memristive devices," *Advanced Functional Materials*, vol. 27, no. 32, pp. 1 700 432–n/a, 2017. [Online]. Available: http://dx.doi.org/10.1002/adfm.201700432

[124] S. H. Chang, J. S. Lee, S. C. Chae, S. B. Lee, C. Liu, B. Kahng, D. W. Kim, and T. W. Noh, "Occurrence of both unipolar memory and threshold resistance switching in a nio film," *Physical Review Letters*, vol. 102, no. 2, p. 026801, 2009. [Online]. Available: https://link.aps.org/doi/10.1103/PhysRevLett.102.026801

[125] C.-Y. Lin, P.-H. Chen, T.-C. Chang, K.-C. Chang, S.-D. Zhang, T.-M. Tsai, C.-H. Pan, M.-C. Chen, Y.-T. Su, Y.-T. Tseng, Y.-F. Chang, Y.-C. Chen, H.-C. Huang, and S. M. Sze, "Attaining resistive switching characteristics and selector properties by varying forming polarities in a single HfO_2-based rram device with a vanadium electrode," *Nanoscale*, vol. 9, no. 25, pp. 8586–8590, 2017. [Online]. Available: http://dx.doi.org/10.1039/C7NR02305G

[126] L. Goux, "Resistive switching: From concept to device optimization," in *2015 IEEE 15th International Conference on Nanotechnology (IEEE-NANO)*, Conference Proceedings, pp. 17–19.

[127] I. Daniele, "Resistive switching memories based on metal oxides: mechanisms, reliability and scaling," *Semiconductor Science and Technology*, vol. 31, no. 6, p. 063002, 2016. [Online]. Available: http://stacks.iop.org/0268-1242/31/i=6/a=063002

[128] Z. Wang, P. B. Griffin, J. McVittie, S. Wong, P. C. McIntyre, and Y. Nishi, "Resistive switching mechanism in $Zn_xCd_{1-x}S$ nonvolatile memory devices," *IEEE Electron Device Letters*, vol. 28, no. 1, pp. 14–16, 2007.

[129] Y. Huang, Y. Luo, Z. Shen, G. Yuan, and H. Zeng, "Unipolar resistive switching of zno-single-wire memristors," *Nanoscale Research Letters*, vol. 9, no. 1, p. 381, 2014. [Online]. Available: https://doi.org/10.1186/1556-276X-9-381

[130] D. Ielmini and S. Menzel, *Universal Switching Behavior*. Wiley-VCH Verlag GmbH & Co. KGaA, 2016, pp. 317–340. [Online]. Available: http://dx.doi.org/10.1002/9783527680870.ch11

[131] W.-Y. Chang, K.-J. Cheng, J.-M. Tsai, H.-J. Chen, F. Chen, M.-J. Tsai, and T.-B. Wu, "Improvement of resistive switching characteristics in TiO_2 thin films with embedded Pt nanocrystals," *Applied Physics Letters*, vol. 95, no. 4, p. 042104, 2009. [Online]. Available: http://aip.scitation.org/doi/abs/10.1063/1.3193656

[132] G. Leiwen, L. Yanhuai, L. Qin, S. Zhongxiao, and M. Fei, "Enhanced resistive switching characteristics in Al_2O_3 memory devices by embedded Ag nanoparticles," *Nanotechnology*, vol. 28, no. 21, p. 215201, 2017. [Online]. Available: http://stacks.iop.org/0957-4484/28/i=21/a=215201

[133] J. Lee, S. Jungho, L. Daeseok, W. Lee, S. Jung, M. Jo, J. Park, K. P. Biju, S. Kim, S. Park, and H. Hwang, "Diode-less nano-scale ZrO_x/HfO_x rram device with excellent switching uniformity and reliability for high-density cross-point memory applications," in *2010 International Electron Devices Meeting*, Conference Proceedings, pp. 19.5.1–19.5.4.

[134] B. K. You, J. M. Kim, D. J. Joe, K. Yang, Y. Shin, Y. S. Jung, and K. J. Lee, "Reliable memristive switching memory devices enabled by densely packed silver nanocone arrays as electric-field concentrators," *ACS Nano*, vol. 10, no. 10, pp. 9478–9488, 2016. [Online]. Available: http://dx.doi.org/10.1021/acsnano.6b04578

[135] D. T. Wang, Y. W. Dai, J. Xu, L. Chen, Q. Q. Sun, P. Zhou, P. F. Wang, S. J. Ding, and D. W. Zhang, "Resistive switching and synaptic behaviors of $TaN/Al_2O_3/ZnO/ITO$ flexible devices with embedded Ag nanoparticles," *IEEE Electron Device Letters*, vol. 37, no. 7, pp. 878–881, 2016.

[136] W. Guan, S. Long, R. Jia, and M. Liu, "Nonvolatile resistive switching memory utilizing gold nanocrystals embedded in zirconium oxide," *Applied Physics Letters*, vol. 91, no. 6, p. 062111, 2007. [Online]. Available: http://aip.scitation.org/doi/abs/10.1063/1.2760156

[137] K. Geetika, M. Pankaj, K. Nitu, K. Sudheendran, F. S. James, and S. K. Ram, "Enhanced resistive switching in forming-free graphene oxide films embedded with gold nanoparticles deposited by electrophoresis," *Nanotechnology*, vol. 27, no. 1, p. 015702, 2016. [Online]. Available: http://stacks.iop.org/0957-4484/27/i=1/a=015702

[138] M.-C. Wu, T.-H. Wu, and T.-Y. Tseng, "Robust unipolar resistive switching of co nano-dots embedded ZrO_2 thin film memories and their switching mechanism," *Journal of Applied Physics*, vol. 111, no. 1, p. 014505, 2012. [Online]. Available: http://aip.scitation.org/doi/abs/10.1063/1.3674322

[139] D. Panda, A. Dhar, and S. K. Ray, "Nonvolatile memristive switching characteristics of tio¡formula formulatype="inline"¿¡tex notation="tex"¿$_{bm2}$ ¡/tex¿¡/formula¿ films embedded with nickel nanocrystals," *IEEE Transactions on Nanotechnology*, vol. 11, no. 1, pp. 51–55, 2012.

[140] T. K. Kang, C. C. Tsao, and W. L. Chen, "Resistive switching characteristics in HfO_x memory devices embedded with pd nanocrystals," in *2014 Silicon Nanoelectronics Workshop (SNW)*, Conference Proceedings, pp. 1–2.

[141] C.-Y. Liu, J.-J. Huang, and C.-H. Lai, "Resistive switching characteristics of a Pt nanoparticle-embedded sio2-based memory," *Thin Solid Films*, vol. 529, pp. 107–110, 2013. [Online]. Available: http://www.sciencedirect.com/science/article/pii/S0040609012003999

[142] L. Chen, H. Y. Gou, Q. Q. Sun, P. Zhou, H. L. Lu, P. F. Wang, S. J. Ding, and D. Zhang, "Enhancement of resistive switching characteristics in Al_2O_3-based rram with embedded ruthenium nanocrystals," *IEEE Electron Device Letters*, vol. 32, no. 6, pp. 794–796, 2011.

[143] J. H. Yoon, J. H. Han, J. S. Jung, W. Jeon, G. H. Kim, S. J. Song, J. Y. Seok, K. J. Yoon, M. H. Lee, and C. S. Hwang, "Highly improved uniformity in the resistive switching parameters of TiO_2 thin films by inserting ru nanodots," *Advanced Materials*, vol. 25, no. 14, pp. 1987–1992, 2013. [Online]. Available: http://dx.doi.org/10.1002/adma.201204572

[144] M. J. Yun, H.-D. Kim, S. M. Hong, J. H. Park, D. S. Jeon, and T. G. Kim, "Effect of embedded metal nanocrystals on the resistive switching characteristics in nin-based resistive random access memory cells," *Journal of Applied Physics*, vol. 115, no. 9, p. 094305, 2014. [Online]. Available: http://aip.scitation.org/doi/abs/10.1063/1.4867639

[145] M. Irini, B. Panagiotis, S. Spyros, B. Nikos, and T. Dimitris, "Coexistence of bipolar and threshold resistive switching in TiO_2 based structure with embedded hafnium nanoparticles," *Journal of Physics D: Applied Physics*, vol. 50, no. 4, p. 045103, 2017. [Online]. Available: http://stacks.iop.org/0022-3727/50/i=4/a=045103

[146] S. Hong, T. Choi, J. H. Jeon, Y. Kim, H. Lee, H.-Y. Joo, I. Hwang, J.-S. Kim, S.-O. Kang, S. V. Kalinin, and B. H. Park, "Large resistive switching in ferroelectric $BiFeO_3$ nano-island based switchable diodes," *Advanced Materials*, vol. 25, no. 16, pp. 2339–2343, 2013. [Online]. Available: http://dx.doi.org/10.1002/adma.201204839

[147] L. Zhao, Z. Lu, F. Zhang, G. Tian, X. Song, Z. Li, K. Huang, Z. Zhang, M. Qin, SujuanWu, X. Lu, M. Zeng, X. Gao, J. Dai, and J.-M. Liu, "Current rectifying and resistive switching in high density $BiFeO_3$ nanocapacitor arrays on nb-$SrTiO_3$ substrates," *Scientific Reports*, vol. 5, p. 9680, 2015. [Online]. Available: http://dx.doi.org/10.1038/srep09680

[148] Z. Lu, Z. Fan, P. Li, H. Fan, G. Tian, X. Song, Z. Li, L. Zhao, K. Huang, F. Zhang, Z. Zhang, M. Zeng, X. Gao, J. Feng, J. Wan, and J. Liu, "Ferroelectric resistive switching in high-density nanocapacitor arrays based on $BiFeO_3$ ultrathin films and ordered Pt nanoelectrodes," *ACS Applied Materials & Interfaces*, vol. 8, no. 36, pp. 23 963–23 968, 2016. [Online]. Available: http://dx.doi.org/10.1021/acsami.6b07792

[149] K. Park and J.-S. Lee, "Controlled synthesis of ni/cuo(x)/ni nanowires by electrochemical deposition with self-compliance bipolar resistive switching," *Scientific Reports*, vol. 6, p. 23069, 2016. [Online]. Available: http://www.ncbi.nlm.nih.gov/pmc/articles/PMC4791678/

[150] C. Baeumer, R. Valenta, C. Schmitz, A. Locatelli, T. O. Menteş, S. P. Rogers, A. Sala, N. Raab, S. Nemsak, M. Shim, C. M. Schneider, S. Menzel, R. Waser, and R. Dittmann, "Subfilamentary networks cause cycle-to-cycle variability in memristive devices," *ACS Nano*, vol. 11, no. 7, pp. 6921–6929, 2017. [Online]. Available: http://dx.doi.org/10.1021/acsnano.7b02113

[151] U. Celano, G. Giammaria, L. Goux, A. Belmonte, M. Jurczak, and W. Vandervorst, "Nanoscopic structural rearrangements of the Cu-filament in conductive-bridge memories," *Nanoscale*, vol. 8, no. 29, pp. 13 915–13 923, 2016. [Online]. Available: http://dx.doi.org/10.1039/C5NR08735J

[152] V. Sujaya Kumar, W. Hyunsuk, and J. Sanghun, "Enhancement of resistive switching properties in Al_2O_3 bilayer-based atomic switches: multilevel resistive switching," *Nanotechnology*, vol. 29, no. 23, p. 235202, 2018. [Online]. Available: http://stacks.iop.org/0957-4484/29/i=23/a=235202

[153] U. Celano, *Nanoscaled Electrical Characterization*. Cham: Springer International Publishing, 2016, pp. 47–86. [Online]. Available: https://doi.org/10.1007/978-3-319-39531-9_3

[154] R. Degraeve, A. Fantini, S. Clima, B. Govoreanu, L. Goux, Y. Y. Chen, D. Wouters, P. Roussel, G. S. Kar, and G. Pourtois, "Dynamic 'hour glass' model for set and reset in HfO_2 rram," in *VLSI Technology (VLSIT), 2012 Symposium on*. IEEE, Conference Proceedings, pp. 75–76.

[155] S. Asapu and T. Maiti, "Multifilamentary conduction modeling in transition metal oxide-based rram," *IEEE Transactions on Electron Devices*, vol. 64, no. 8, pp. 3145–3150, 2017.

[156] U. Celano, L. Goux, A. Belmonte, K. Opsomer, C. Detavernier, M. Jurczak, and W. Vandervorst, "Conductive filaments multiplicity as a variability factor in cbram," in *2015 IEEE International Reliability Physics Symposium*, Conference Proceedings, pp. MY.11.1–MY.11.3.

[157] H. Du, C.-L. Jia, A. Koehl, J. Barthel, R. Dittmann, R. Waser, and J. Mayer, "Nanosized conducting filaments formed by atomic-scale defects in redox-based resistive switching memories," *Chemistry of Materials*, vol. 29, no. 7, pp. 3164–3173, 2017. [Online]. Available: http://dx.doi.org/10.1021/acs.chemmater.7b00220

[158] B. Writam, L. Qi, L. Shibing, L. Hangbing, and L. Ming, "Crystal that remembers: several ways to utilize nanocrystals in resistive switching memory," *Journal of Physics D: Applied Physics*, vol. 50, no. 30, p. 303002, 2017. [Online]. Available: http://stacks.iop.org/0022-3727/50/i=30/a=303002

[159] J. Ouyang, "Application of nanomaterials in two-terminal resistive-switching memory devices," *Nano Reviews*, vol. 1, no. 1, p. 5118, 2010. [Online]. Available: https://doi.org/10.3402/nano.v1i0.5118

[160] A. R. Smith, W. Yoon, W. B. Heuer, S. I. M. Baril, J. E. Boercker, J. G. Tischler, and E. E. Foos, "Effect of ligand structure on the optical and electronic properties of nanocrystalline pbse films," *The Journal of Physical Chemistry C*, vol. 116, no. 10, pp. 6031–6037, 2012. [Online]. Available: https://doi.org/10.1021/jp2111023